

Characterizing the Climate of Distant Worlds via
High Precision Photometry with the
Spitzer Space Telescope

A dissertation presented by

K. H. Lisa Đặng

to the Department of Physics

in partial fulfillment of the requirements for the degree of

Doctor of Philosophy

McGill University

Tiohtià:ke/Montréal, Québec

August 2022

© 2022 — K. H. Lisa Dặng

All rights reserved.

Characterizing the Climate of Distant Worlds via High Precision Photometry with the Spitzer Space Telescope

Abstract

Unexpected at the time of its conception, the Spitzer Space Telescope has provided considerable insights into the characterization of exoplanets and has paved the way for future exoplanet missions. More particularly, *Spitzer* was first to detect the infrared radiation of highly irradiated, close-in transiting giant exoplanets and pioneered a powerful *phase curves* technique consisting of observations spanning the full orbit of the planet to reveal the presence of an atmosphere and the in-homogeneous longitudinal temperature structure of the planet. In this thesis, I present the thermal phase curve of three different study cases: 1) CoRoT-2b, a young hot Jupiter on a circularized orbit, 2) XO-3b, an eccentric massive hot Jupiter, 3) 55 Cnc e, an ultra short period rocky planet. From these investigations, I show that the climate of a close-in exoplanet cannot be solely explained by its current orbital configuration. Interestingly, our observations suggest that hints of a planet's past could manifest itself in phase curve observations implying that history matters on these scorching hot worlds.

Through these investigations, I demonstrate that retrieving astrophysical parameters is not always robust against the decorrelation method used. Achieving high precision photometry via instrumental systematics detrending is a prerequisite for hot thermal phase curves. This led me to a cross-disciplinary foray into gravitational lensing. During its last years, *Spitzer* also served as a microlens parallax satellite to study exoplanets beyond the snow line which provided an unconventional study case to test commonly used self-calibration techniques and enabled the development of an approach for multi-epoch observations. In short, in this dissertation, I show how *Spitzer* has set the stage for future exoplanet investigations with next-generation instruments and observatories and guide how we will interpret those observations.

Caractériser le climat de planètes lointaines grâce à la photométrie de haute précision avec le télescope spatial *Spitzer*

Abrégé

Malgré que ce n'était pas planifié au moment de sa conception, le télescope spatial *Spitzer* a fourni des informations importantes sur la caractérisation des exoplanètes et a ouvert la voie à de futures missions exoplanétaires. Plus particulièrement, *Spitzer* a été le premier à détecter le rayonnement infrarouge d'une exoplanète géante fortement irradiée et a été le pionnier d'une puissante technique de *courbe de phase* consistant en des observations couvrant toute l'orbite de la planète pour révéler la présence d'une atmosphère et la structure de température longitudinale inhomogène de la planète. Dans cette thèse, je présente la courbe de phase thermique de trois études de cas : 1) CoRoT-2b, une jeune Jupiter chaude sur une orbite circulaire, 2) XO-3b, une Jupiter chaude massive avec une orbite excentrique, 3) 55 Cnc e, une planète rocheuse ayant une période ultra courte. À partir de ces investigations, je démontre que le climat d'une exoplanète proche ne peut s'expliquer uniquement par sa configuration orbitale actuelle. Fait intéressant, nos observations suggèrent que des indices du passé d'une planète pourraient se manifester dans des observations de courbe de phase impliquant que l'histoire compte dans ces mondes brûlants.

De plus, je démontre que l'estimation des paramètres astrophysiques ne sont pas toujours robuste face à la méthode de décorrélation utilisée. L'obtention d'une photométrie de haute précision est un préalable pour les observations de courbe de phase et nécessite alors la décorrélation des effets instrumentaux. Cette expertise est donc ce qui m'a menée sur une incursion interdisciplinaire dans le domaine des études de lentilles gravitationnelles. Au cours de ses dernières années, *Spitzer* a également servi de satellite à parallaxe à microlentilles pour étudier les exoplanètes au-delà de la lignes des glaces, ce qui a fourni une étude de cas non conventionnelle pour tester les techniques de décorrélation couramment utilisées et a permis le développement d'une approche pour les observations multi-époques. Bref, dans cette thèse, je démontre comment *Spitzer* a préparé le terrain pour de futures enquêtes sur les exoplanètes avec des instruments et des observatoires de nouvelle génération et guide la manière dont nous interpréterons ces observations.

Contents

Abstract	iii
Abrégé	iv
Acknowledgments	ix
1 Introduction	1
1.1 Exoplanets	1
2 Background	7
2.1 Time Series Observations with Spitzer	7
2.2 Phase Curves of Short-Period Exoplanets	7
2.2.1 Circular Orbits: Thermal Map of Close-in Planets	8
2.2.2 Eccentric Orbits: Seasonal Variation on Exoplanets	9
2.3 Exoplanetary Microlensing: Detecting Long-Period Exoplanets	11
2.3.1 Gravitational Microlensing 101	11
2.3.2 Microlens Parallax to break the Mass-Distance	14
2.4 High Precision Photometry in Time-Series	14
3 Detection of a Westward Hotspot Offset in the Atmosphere of a Hot Gas Giant CoRoT-2b	17
3.1 Main Text	19

CONTENTS

3.2	Methods	26
3.2.1	Data Source	26
3.2.2	Data Reduction	27
3.2.3	Astrophysical Model	27
3.2.4	Detector Models	29
3.2.5	Model Fitting and Error Estimates	31
3.2.6	Priors	32
3.2.7	Model Comparison	33
3.2.8	Surface Brightness Map	35
3.2.9	Energy Budget	35
3.2.10	Emission Spectroscopy	36
3.2.11	Constraint on Magnetic Field Strength of CoRoT-2b	36
3.3	Supplementary Tables	39
3.4	Supplementary Figures	45
3.5	Supplementary Information	58
3.5.1	Data Reduction	58
3.5.2	Photometry Extraction	59
3.5.3	Centroids	60
3.5.4	Noise in <i>Spitzer</i> IRAC Data due to Bias Dark Subtraction	61
3.5.5	Binning	61
3.5.6	Upper Limit on Stellar Variability at $4.5 \mu m$	62
3.5.7	Surface Brightness	62
4	Pixel Level Decorrelation in Service of the <i>Spitzer</i> Microlens Parallax Survey	65
4.1	Introduction	67
4.1.1	Decorrelation Techniques Developed for <i>Spitzer</i> Observations	69

CONTENTS

4.2	Observations	70
4.2.1	Challenges with Spitzer Microlensing Campaign	70
4.2.2	Timescale	71
4.2.3	Pointing	71
4.2.4	Field Rotation	71
4.2.5	Relative Brightness	72
4.2.6	Magnitude of the Signal	72
4.2.7	Signal Coverage	73
4.3	Method Description	73
4.3.1	Photometry Extraction	73
4.3.2	Detrending	74
4.3.3	Astrophysical Model	75
4.3.4	Regressors	75
4.3.5	Fitting Process	77
4.3.6	Model Comparison	79
4.4	Examples	79
4.4.1	OGLE-2017-BLG-1140b	80
4.4.2	OGLE-2015-BLG-0448	82
4.5	Discussion and Conclusion	85
5	Thermal Phase Curves of XO-3b: an Eccentric Hot Jupiter at the Deuterium Burning Limit	89
5.1	Introduction	91
5.2	Observation and Reduction	94
5.2.1	Data Reduction	94
5.2.2	Extracting the Photometry	95
5.2.3	PSF Diagnostics	98

CONTENTS

5.3	Model	99
5.3.1	Astrophysical Model	99
5.3.2	Detector Model	100
5.4	Parameter Estimation and Model Comparison	102
5.4.1	Model Comparison	104
5.5	Results	106
5.5.1	SPCA Fits	106
5.5.2	Energy Balance Model	108
5.5.3	Spitzer/IRAC 3.6: A Cautionary Tale	112
5.5.4	Theoretical Models of XO-3b’s Atmosphere	114
5.5.5	Possible Inflated Radius of XO-3b	120
5.6	Summary and Conclusion	122
6	A Hell of a Phase Curve	127
6.1	Overview of Lava Planets	128
6.2	Re-Analysis of 55 Cnc e’s Phase Curve	128
6.2.1	Authors Contribution	131
6.3	Mapping the Atmosphere and Surface of K2-141b	131
7	Conclusion	137
	References	141

Acknowledgments

To my supervisor, Nick, it's been incredibly rewarding to be your student. Thank you for sharing your enthusiasm for science and for fostering my curiosity about our own climate and that of distant worlds. I will forever be grateful for your thoughtful guidance, never-ending encouragement, and endless opportunities provided over the years. Your uplifting mentorship has been exemplary and will remain an inspiration to me for the rest of my career, wherever it leads me. I am proud to have been an inaugural member of your group at McGill.

I'm a product of my environment and my success is reflective of the delightful atmosphere provided by my community at the McGill Space Institute, the Department of Physics, and the MEChA research group. In particular, to my work buddies, Taylor, Dylan, and Keavin, it's been a blast to learn by your side and go on scientific excursions with you!

Cám ơn Mamy và Papy, even though I didn't learn to solve algebraic equations from you, the work ethic and the unconditional care you've taught me transpires through the pages of this dissertation. To my sister, thank you for reminding me to take things easy when I started to get overwhelmed. To my family in Montreal, in Vietnam, and those I met for the first time during my stint in California, thank you for the support throughout the years. To my dearest friends, *you know who you are*, thank you for lending an ear, for cheering me up, and for keeping me grounded.

Last but not least, to David, *meu querido*, thank you for joining me in this unconventional adventure, for your endless support, and for the incredible love you give. Consistently laughing with you is what kept me sane through this wild ride. Thank you for continuously uplifting my general cultural knowledge and keeping me up to date with what's going on in the world. I'm excited about where life takes us next.

*If because of my schooling, I had grown culturally separated from my parents,
my education finally had given me ways of speaking and caring about that fact.*

– The Desire of Achievement, Richard Rodriguez, 1982

Chapter 1

Introduction

1.1 Exoplanets

Before the exoplanets era, the architecture of the Solar System has long been the primary inspiration for planet formation and evolution theories. It was then theorized that all planets started as rocky cores located on the orbit they follow today. Cores farther from the Sun, where it gets cold enough for abundant volatiles like water and methane to condense, accreted large envelopes and formed gas giant planets such as Jupiter and Saturn. Meanwhile, the high temperature of the inner Solar System caused volatiles to be scarce, consequently limiting the ability for planetary cores, like Earth's, to accrete large envelopes of gas.

The detection of the first hot Jupiter, 51 Pegasi b, a gas giant planet with a 4-day orbital period, is still one of the most astonishing planetary discoveries as leading planet formation theories then could not explain such a planet ([Mayor & Queloz 1995](#)). The discovery of 51 Peg b led to the search for pathways in which gas giants could migrate so close to their stars ([Lin et al. 1996](#); [Rasio & Ford 1996](#)) and was awarded the 2019 Nobel Prize in Physics. In parallel, an increasing number of Solar System investigations also suggested that the Solar System's history was more dramatic than previously thought (e.g. [Malhotra 1993](#); [Thommes et al. 1999](#)); our formation and evolution theory needed revision (e.g., [Gomes et al. 2005](#); [Walsh et al. 2012](#)).

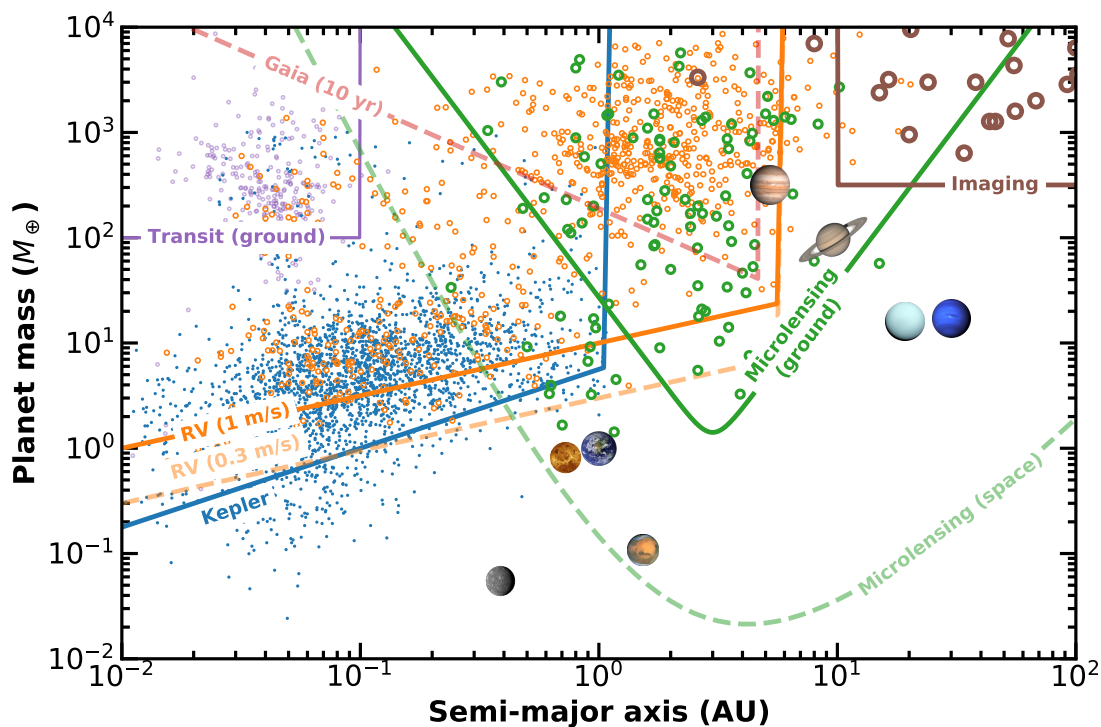


Figure 1.1: Mass versus semimajor axis of known planets color-coded according to their method of detection, based on the “Confirmed Planets” list from the NASA Exoplanet Archive (Akeson et al. 2013, acquired in September 2021) from Zhu & Dong 2021. Ground-based and space-based *transiting planets* are plotted in purple and blue, respectively. *Doppler planets* are denoted plotted in orange and *directly imaged planets* are shown in brown. Finally, ground-based *microlensing exoplanets* are plotted in green. Additionally, the light red curve denotes *Gaia*’s sensitivity curve, an on-going space-based survey to detect *astrometric planets* and the light green curve is the sensitivity curve of the upcoming Nancy Grace Roman Microlensing Survey.

Exoplanet Detection

The number of detected extrasolar planets has recently passed 5000 as a result of successful exoplanets detection surveys, most notably the Kepler Space Telescope (Borucki et al. 2010) and Transiting Exoplanets Survey Satellite (TESS, Ricker et al. 2015). The inventory of detected exoplanets and their measured properties provide statistical insights into planetary formation and evolution scenarios while placing Solar System in a broader context (Gaudi 2022). Astronomy is unlikely to provide intimate details of exoplanets to the same level that Solar System exploration provides, but the numerous extra-solar planets spanning a large region of parameter

CHAPTER 1. INTRODUCTION

space could allow for hundreds of case studies. As shown in Figure 1.1, exoplanets are wildly diverse and the vast majority of these other worlds have properties strikingly different from the Solar System planets.

A direct image of an exoplanet in the vicinity of their self-illuminated stellar counterpart is extremely difficult to detect and spatially resolve – the planetary brightness is drowned by the massive radiation emitted by their host star. As a result, most exoplanets discovered via direct imaging reside at large separation from their host star and are large enough to reflect or emit an appreciable amount of flux (Gaudi 2022). Nonetheless, remarkable advances have enabled the detection of thousands of exoplanets by leveraging their effect on their host stars and surrounding gravitational field. Figure 1.1 categorizes known exoplanets according to their detection methods and presents the sensitivity curve of each method:

- *Transiting planets* offer a fascinatingly simple way to be detected – as they orbit in front of their host star, they will block a fraction of the incoming light from their host star resulting in periodic decrease of the apparent stellar brightness.
- Conservation of momentum requires that as a planet orbits a distant star, the star also orbits about their common center of mass. *Doppler planets* reside on an-edge on orbit and cause a radial reflex motion of their host star which can be detected in spectroscopic time-series radial velocity measurements. *Astrometric planets* reside on face-on orbits, as such, the detection of periodic variations of a star’s position in the sky plane can infer their presence.
- *Microlensing exoplanets* are detected through their gravitational influence on the light coming from a more distant background star as they move in and out of alignment. The biggest advantage of this technique is its unique capability to probe planets at large orbital separation, as this technique does not require observations spanning a significant fraction of the orbital period, for a wide range of masses.

As not all planets are created equal, they are not equally amenable to any single method of detection. Rather, these different detection techniques complement each other by probing a different part of parameter space and constraining different properties. As transiting and doppler planets require observations spanning at least an orbital period to be reliably detected, transit and radial velocity surveys are biased towards short-period exoplanets. In contrast, microlensing and direct imaging surveys can detect long-period exoplanets as they can be detected with time series observations spanning a minuscule fraction of the planet’s orbit. Patterns in the distribution of known exoplanets allow for theories of the origin and the evolution of

planetary systems to be tested (Zhu & Dong 2021). Ground-based observatories have pioneered many of these detection techniques, while the precision offered by space-based observatories revolutionized our ability to probe a larger variety of exoplanets. The remaining parameter space, on-going and future exoplanet hunting satellites such as the Gaia mission (Gaia Collaboration et al. 2016), which will enable the search for astrometric planets, and the Nancy Grace Roman Space Telescope microlensing survey (Spergel et al. 2015). Of these methods of detection, space-based microlensing is most sensitive to Solar System analogs, but detailed follow-up characterization is often inaccessible due to the transient nature of gravitational lensing events. At the other end of the figure, *transiting short-period planets* radiate higher heat flux and are the most amenable for atmospheric characterization.

Exoplanet Atmosphere Characterization

As the field of exoplanets gradually expands from detection to atmospheric characterization, transiting short-period exoplanets have been objects of extensive atmospheric investigations due to their fortuitously edge-on orbit. Not long after the first detection of thermal emission from a hot Jupiter as it was eclipsed by its host star (Charbonneau et al. 2005), it was suggested that obtaining observations of part or all the planetary orbit could reveal the in-homogeneous longitudinal temperature structure of a planet (Knutson et al. 2007; Cowan & Agol 2008). This observing technique, also referred as phase curves, has since provided important insights into the atmospheric dynamics of hot Jupiters by constraining heat transport and winds, and enabling atmospheric properties of hot Jupiters to be studied as a population (e.g. Keating et al. 2019). In parallel, exoplanet hunting missions such as Kepler and TESS have discovered a rich diversity of exoplanets and measurements of the bulk properties of these planets, their host stars, and the systems as a whole have enabled demographic investigations (e.g. Fulton et al. 2017). While bulk properties of exoplanets are key for testing planet formation and evolution theories, detailed atmospheric characterization of exoplanets provide deeper understanding of their composition and of the planet as a whole.

The Spitzer Space Telescope (2003-2020)

During its conception, exoplanetary sciences were not projected to be a substantial part of the now retired Spitzer Space telescope mission. Nonetheless, its contribution to the field remains one of its biggest scientific legacy as it set the stage for future space-based exoplanet missions (Deming & Knutson 2020). More particularly, *Spitzer* was first to detect the infrared radiation of highly irradiated, close-in transiting gi-

CHAPTER 1. INTRODUCTION

ant exoplanets, also called hot Jupiters, as they emit more thermal flux than their cooler counterparts (Charbonneau et al. 2005). Not long after, *Spitzer* pioneered a powerful technique called *phase curves* consisting of observations spanning the full orbit of the planet to reveal the presence of an atmosphere and the in-homogeneous longitudinal temperature structure of the planet (Knutson et al. 2007). For example, one of *Spitzer*'s greatest legacies is thermal phase curve observations of a large sample of highly-irradiated exoplanets. Moreover, in the last five-years of operation, *Spitzer* served as a *microlens parallax satellite* and routinely measured the mass and distance of gravitational lenses. While the information from these two investigations are orthogonal to each other, they provide complementary insights in the larger context of exoplanetary science, share similar observational challenges and can benefit from similar data reduction treatment.

In this manuscript-based thesis, I present my contribution to our understanding of exoplanet atmospheric dynamics from *Spitzer* phase curves as well as a cross-disciplinary contribution to the *Spitzer Microlensing Campaign*. First, in chapter 2 I review climate characterization of various short-period exoplanets via *Spitzer* phase curve observations and provide background concepts of gravitational exoplanetary microlensing. Then, I present a series of published articles in chronological order. In chapter 3, I report the first detection of a *westward* hotspot offset on the young gas giant CoRoT-2b. In chapter 4, I developed a new detrending technique for the *Spitzer Microlensing Survey* inspired by decorrelation methods designed for eclipse observation. Chapter 5 presents the analysis of the phase curve of the eccentric hot Jupiter XO-3b. Then, I present a summary of my contribution to the current and future studies of Ultra-Short Period (USPs) rocky planets in chapter 6. Each chapter is preceded by a prologue briefly introducing each article and is followed by an epilogue summarizing follow-up work since their publication. Finally, I present the conclusions of this thesis in Chapter 7.

CHAPTER 1. INTRODUCTION

Chapter 2

Background

2.1 Time Series Observations with Spitzer

The common theme of projects presented in this thesis is the use of high-fidelity time-series observations also referred as *lightcurves* acquired during the *warm* mission of the *Spitzer* space telescope with the InfraRed Array Camera (IRAC, [Fazio et al. 2004](#)). In this chapter, I review the value of *Spitzer* lightcurves for two distinct scientific investigations: 1) characterizing the climate of short-period exoplanets and 2) constraining the distribution of microlensing exoplanets towards the galactic bulge. Then, I describe background concepts for each science case and discuss the astrophysical insights they provide. Finally, I discuss the obstacles to high-precision photometry and present examples of state-of-the-art data treatment commonly applied to *Spitzer*/IRAC lightcurves to decorrelate instrumental systematics.

2.2 Phase Curves of Short-Period Exoplanets

As a transiting planet orbits around their host star, a distant observer will observe a transit and secondary eclipse as the planet passes in front and behind. As the planet rotates, different regions of the planet will rotate in and out of view of the observer causing a variation of brightness over time. *Phase curves*, lightcurves spanning the entire orbital period of a planet, are particularly rich in information as they uniquely probe the planet's atmosphere as a whole as opposed to only its dayside or limb ([Seager & Deming 2010](#); [Heng & Showman 2015](#)). Phase curves record the increase and decrease of planetary flux as a function of orbital phases which are shaped by the convolution of the planet's longitudinal brightness distribution and its geometric pro-

jection to the observer (Cowan & Agol 2011a). In this section, I discuss atmospheric constraints that phase curves of short-period planets provide and the insights they provide into atmospheric processes.

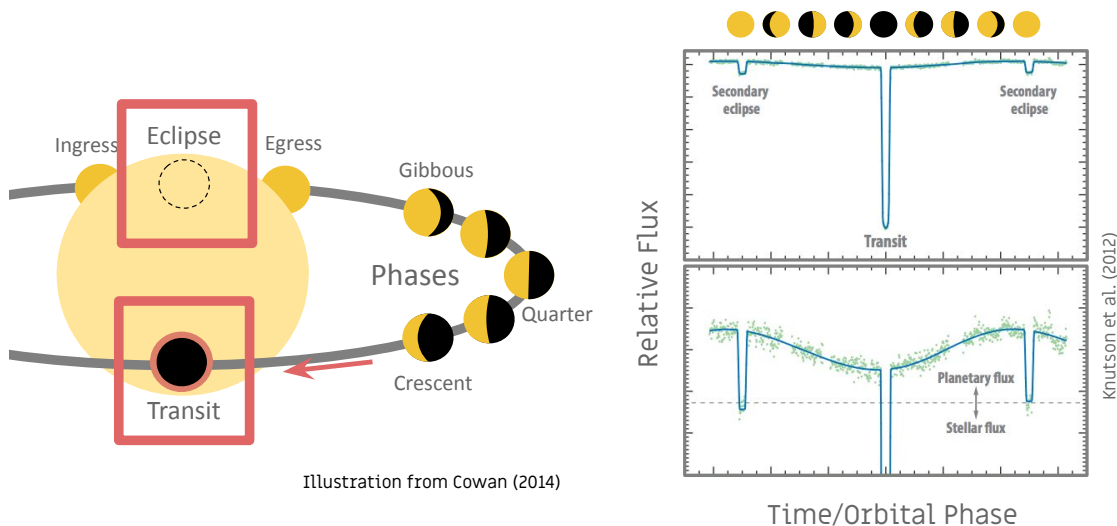


Figure 2.1: *Left:* Viewing geometry of a transiting planetary system. *Right:* The corresponding exhibits a sharp decrease in brightness during occultation and phase modulations shaped by the brightness distribution of the planet convolved with its projection to the observer.

2.2.1 Circular Orbits: Thermal Map of Close-in Planets

Obtaining a full-orbit phase curve is a rather time-consuming task for most exoplanets, however, short-period exoplanets are particularly amenable for this method. Close-in exoplanets are expected to experience strong tidal interaction with their parent star leading to the circularization of their orbit and the synchronization of their rotation with their orbital spin. As the timescale for synchronous rotation is generally shorter than the circularization time scale, short-period planets on circular orbits are expected to also be synchronously rotating, i.e. $P_{orb} = P_{rot}$, where P_{orb} and P_{rot} are the planet's orbital and rotation period, respectively (for a review, see Heng & Showman 2015). As a result, close-in exoplanets have a scorching permanent dayside blasted with stellar irradiation and a permanent frigid nightside which provide an unprecedented laboratory for atmospheric processes.

Photometric phase curves observations at different wavelengths provide different insights into the planet's atmosphere: optical phase curves constrains the planet's reflectivity and the distribution of condensates across the planet, while infrared phase curves record the emission of the planets and inform us about the thermal structure of

the planet. High-precision phase curves, as presented in Figure 3.2, can be converted into planetary longitudinal brightness maps (Cowan & Agol 2008), a unique method to characterize the nightside of synchronously rotating exoplanets that can provide key insights into atmospheric dynamics. The phase amplitude and offset inform us about the displacement of the brightest and the darkest region from the substellar and anti-stellar point on the planet.

Finally, infrared phase modulations of highly-irradiated exoplanets are dominated by their thermal emission and allow us to measure the dayside and nightside temperature. Inverting the Planck function (Cowan & Agol 2011a), the brightness temperature at wavelength λ can be expressed as:

$$T_b(\lambda) = \frac{hc}{\lambda k_B} \left[\log \left(1 + \frac{e^{(hc/\lambda k_B T_*)} - 1}{\psi(\lambda)} \right) \right] \quad (2.1)$$

where h is the Planck constant, c is the speed of light, k_B is the Boltzmann constant, and $\psi(\lambda)$ is the relative intensity of the planet to that of its host star. The dayside relative intensity can be expressed as $\psi_d(\lambda) = \delta_{ecl}/\delta_{tr}$, where δ_{ecl} and δ_{tr} are the eclipse and transit depth, respectively. Meanwhile, the nightside intensity ratio is defined as $\psi_n(\lambda) = \frac{\delta_{ecl} - (F_{p,ecl} - F_{p,tr})}{\delta_{tr}}$, where $F_{p,ecl}$ and $F_{p,tr}$ is the planetary flux during eclipse and transit, respectively (Schwartz et al. 2017). Finally, constraining the dayside and nightside temperature also allows for the planet’s Bond albedo and heat re-circulation efficiency to be simultaneously constrained (Cowan & Agol 2011a; Schwartz & Cowan 2015; Schwartz et al. 2017). Thus far, hot Jupiters have been the primary focus for this technique as they are the optimal target for phase curve characterization due to their large signals and short orbital period. Excitingly, the phase curve of a handful of newly discovered ultra-short period planets have been detected in recent years.

2.2.2 Eccentric Orbits: Seasonal Variation on Exoplanets

While most hot Jupiters are found on circular orbits, a few short-period gas giants on eccentric orbits have been detected. Though rare, the existence of moderately eccentric hot Jupiters is indicative that some gas giants underwent eccentricity tidal migration (e.g. Dawson & Johnson 2018). The orbital eccentricity of a planet is a relic of its evolutionary history. In addition, they represent a unique opportunity to observe a planetary atmosphere’s response to varying incident stellar flux as they revolve around their parent star as illustrated in Figure 2.2 (Kataria et al. 2013). The variation in incoming flux can lead to dramatic time-dependent changes in the thermal and chemical atmospheric structure. For example, the planet’s temperature

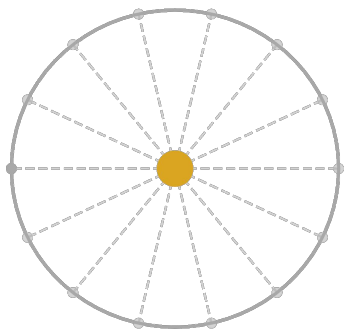
CHAPTER 2. BACKGROUND

at apoapse could be cold enough for some cloud condensate species to form and later dissipate as the insolation increases toward periapse.

To investigate these temporal effects and how they are manifested in time-series observation of eccentric gas giants, several theoretical models with varying complexities have been developed to predict climate properties of these objects. General circulation models allow for sophisticated computationally-intensive 3D atmospheric investigation of temporal changes in the thermal, chemical and advective structure (Kataria et al. 2013; Lewis et al. 2013, 2017a). Rapid one-dimensional time-stepping radiative-convective models have also been developed to investigate the planet-averaged change in thermal and chemical structure of eccentric gas giants as a function of orbital phase, however, they do not explore their atmospheric latitudinal and longitudinal in-homogeneity (Mayorga et al. 2021). Another efficient model used for eccentric planets is a semi-analytical energy-balance model that allow for the study of radiative processes and the advective heat-redistribution but neglect the effect of wavelength-dependent opacities on the heat distribution (Cowan & Agol 2011a; Bell & Cowan 2018).

Short Period Planets on circular orbit:

- *Tidally locked* - the star is stationary on the sky and the planet receives a constant amount of stellar flux.
- *1-D Longitudinal brightness map* can be obtained from the full-orbit phase curve
- *Heat recirculation* is responsible for the shape of the lightcurve (phase offset and amplitude).



Short Period Planets on Eccentric orbit:

- *Pseudosynchronism* - the planet is only tidally locked near periapse and the rotation rate of the planet is not constant
- *Variation of distance to the star* - the planet receives a varying stellar flux throughout the orbit.
- *The time varying stellar flux* allows us to break the degeneracy between the advective and radiative timescale.

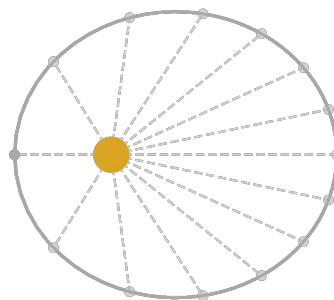


Figure 2.2: Summary of the key differences between a typical hot Jupiter and a moderately eccentric planet and constraints their phase curve provides.

Encoded in their phase curve observations is information about radiative and dynamical atmospheric processes, however, extracting information from observation of eccentric planets involves unique challenges. In particular, the interpretation of

thermal phase curves can be complicated due to the convolution of spatial, diurnal, and seasonal forcing. Unlike typical hot Jupiters on circular orbits, these objects do not have their rotation synchronized – rather, they are expected to exhibit pseudosynchronous rotation (e.g. [Hut 1981](#)). Sufficient theoretical insights and comparison with various simulations provide important intuition to elucidate the importance of various processes embedded in our observations. While the thermal map of an eccentric hot Jupiter isn't static, the varying insolation allows us to simultaneously constrain the atmospheric radiative and advective timescales. Thus far, time-variable atmospheric changes have been detected in photometric *Spitzer* observations of eccentric exoplanets ([Laughlin et al. 2009](#); [Lewis et al. 2013](#); [Lanotte et al. 2014](#); [de Wit et al. 2016](#)) and their careful analysis are paving the way for future spectroscopic observations of eccentric gas giants [Sikora et al. \(2021\)](#); [Kataria et al. \(2021\)](#).

2.3 Exoplanetary Microlensing: Detecting Long-Period Exoplanets

2.3.1 Gravitational Microlensing 101

According to Einstein's theory of General Relativity, gravity is the curvature of the fabric of space-time and light is bound to follow the curvature of space-time ([Einstein 1916](#)). As such, any object with a sufficient mass will deflect the trajectory of light-rays passing in its vicinity – this phenomenon is called *gravitational lensing* ([Einstein 1936](#)). A gravitational lensing event occurs when 2 unrelated objects, a background *source* and a foreground *lens* come in and out of alignment along the line of sight of an observer. During the gravitational lensing event, a distant observer will see multiple distorted images of the source appear around the lens. In the special case of perfect alignment between a single lens and a single source, the multiple images of the source will merge and form a bright ring around the lens called the *Einstein ring* with an angular size defined as

$$\theta_E = \left(\frac{4GM_l}{D_{\text{rel}}c^2} \right)^{1/2} \quad (2.2)$$

where G is the gravitational constant, M_l is the lens' mass, c is the speed of light, and $D_{\text{rel}}^{-1} \equiv D_l^{-1} - D_s^{-1}$ with D_l and D_s being the distance of the lens and source, respectively, from the observers. When the alignment isn't exact, two distorted images will appear – a minor image inside the Einstein ring, and a major image outside of the Einstein ring as illustrated in Figure 2.3.

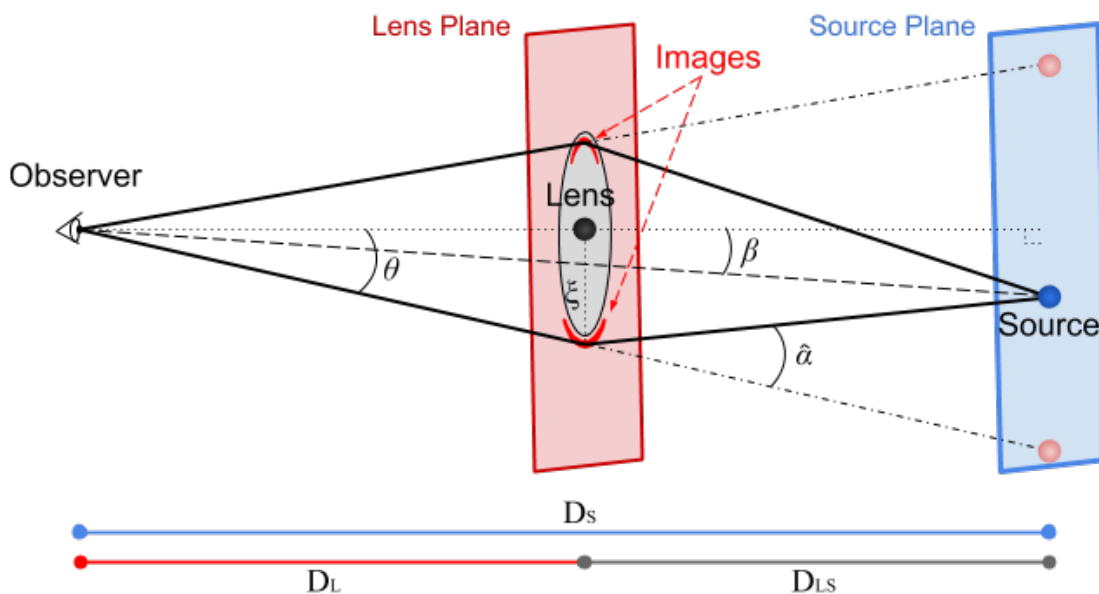


Figure 2.3: The geometry of a single lens microlensing event with non-perfect alignment from Tsapras (2018). Light rays from the background source are deflected by the foreground gravitational lens. Two distorted images, a minor and major image appear inside and outside of the theoretical angular Einstein ring radius from the observer’s perspective.

An important feature of gravitational deflection is that the source’s surface brightness is conserved. The better the alignment, the larger and more distorted the images of the source will appear as more light rays are deflected towards the observer. Consequently, the background source will be magnified and demagnified as the two objects move into and out of alignment as shown in Figure 2.4.

The angular size of the Einstein ring radius for a typical stellar mass lensing a source located in our galactic bulge is too small to be resolved by most existing telescopes. Unlike *strong gravitational lensing*, no single exposure can determine that a microlensing event is happening, instead time-series photometric monitoring allows us to detect the rise and fall of the source’s brightness as a function of time as shown Figure 2.4. A strength of this detection method is that no flux from the lens is necessary therefore allowing for the study of faint and dark objects. Given the unpredictable nature of gravitational microlensing events, modern microlensing surveys employ wide-field observatories to observe dense parts of the sky, e.g. towards the Galactic bulge to maximize the detection yield.

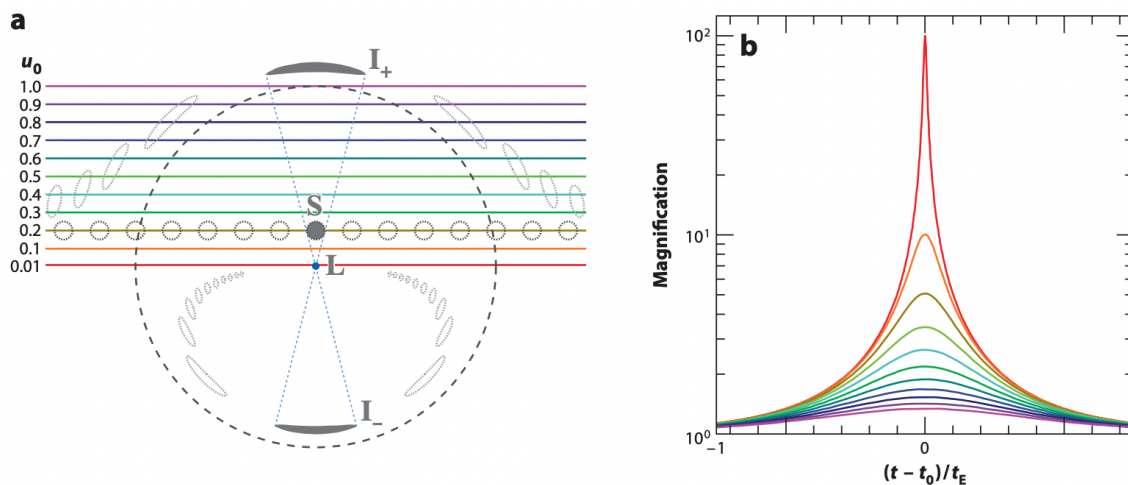


Figure 2.4: Single lens magnification from Gaudi (2012). a) The dashed line circle represents the Einstein ring radius and the array of smaller circles indicate the true trajectory of the source projected onto the lens' plane. For each source position illustrated, the respective minor and major distorted images are represented by the distorted circles. b) The corresponding magnification lightcurves for each source trajectory represented by the coloured lines on the left plot.

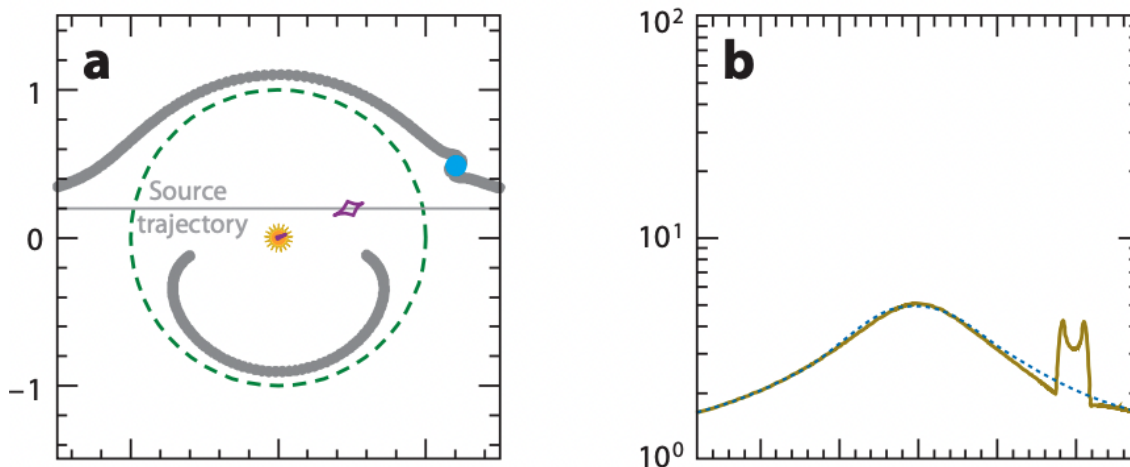


Figure 2.5: Lightcurve planetary anomaly from Gaudi (2012). During the course of the microlensing event, the projected position of the planetary companion will be swept by one of the distorted images of the source, as a result, the light rays will be further deflected and additional images will be created. On the right, the gravitational lensing effect of the planet reveals itself in the lightcurve as a deviation from the single lens magnification.

Exoplanetary Microlensing

Over the course of a microlensing event, as the relative alignment changes, the positions of the minor and major images will sweep out two paths on the sky as shown in Figure 2.5. In the case where the primary lens is accompanied by a much less massive secondary lens, e.g. a star and a planet, the planet will also act as a gravitational lensing with a much smaller Einstein ring. Consequently, the exoplanetary microlensing lightcurve, for the most part, will be similar to the single lens lightcurve. If the planet’s projected position is near one of the paths swept by the images, it will reveal itself when one of the images sweeps by the planet as illustrated in Figure 2.5 – the planet can further deflect nearby light rays which manifest itself in the lightcurve as a lightcurve perturbation also called a *planetary anomaly*. Embedded in exoplanetary microlensing lightcurves is information about the planet-star mass ratio, $q = m_p/M_*$, and projected angular separation, s .

2.3.2 Microlens Parallax to break the Mass-Distance

Although microlensing lightcurves automatically yield the binary lens’ mass ratio, the stellar mass itself is unknown due to a classic microlensing degeneracy known as the mass-distance degeneracy. One way to resolve this degeneracy is by measuring the *microlens parallax* from simultaneous observations of the microlensing event from ground and a well-separated observatory such as *Spitzer* (Refsdal 1966; Gould 1994). As the microlensing viewing geometry is different between a ground-based observatory and a distant space satellite such as *Spitzer*, each observatory will record a different lightcurve. In particular, the time of closest alignment and impact parameter will be different, resulting in different microlensing lightcurves as shown in Figure 2.6. As later described in chapter 4, the microlens parallax provides a mass-distance relation enabling constraints on the relative distance of the lens and the source while simultaneously yielding the lens’ mass. In the last five-years of operation, *Spitzer* served as a microlens parallax satellite and routinely measured the mass and distance of lenses to constrain the distribution of exoplanets towards the Galactic bulge.

2.4 High Precision Photometry in Time-Series

In 2009, the Spitzer Space Telescope ran out of coolant to keep its instrument cold and minimize the instrumental thermal contamination. Fortunately, two of its infrared detectors, IRAC 3.6 and 4.5 μm InSb detectors, remained operational despite

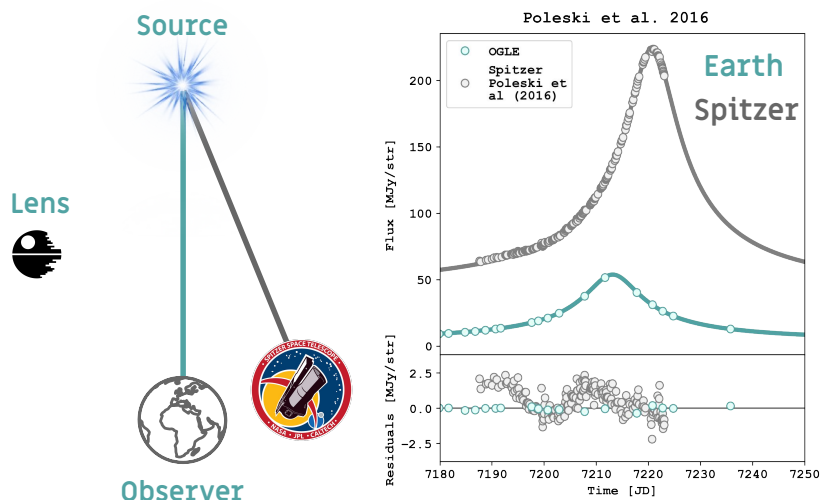


Figure 2.6: Satellite microlens parallax. As the viewing geometry as seen from the Earth and *Spitzer*, their respective lightcurves will be different as illustrated on the right.

the increased temperature. Inconveniently, *Spitzer* IRAC observations are known to be plagued with detector systematics due to the interplay of residual telescope pointing fluctuations with non-uniform intra-pixel gain variations in the moderately under-sampled camera. As such, extracting exoplanets signals at the 100 parts per million (ppm) level can be extremely challenging and require the removal of significant instrumental effects (for a review, see [Ingalls et al. 2016](#)). Over the past decade, improvements in the observing strategy along with a suite of techniques developed to remove time-correlated noise in IRAC have revealed the robust thermal phase curves of many short-period exoplanets. An important distinction in the analysis of *Spitzer* lightcurves, is that the data reduction and data fitting are done simultaneously. In short, the instrumental noise model and the astrophysical model are fit at the same time allowing for the propagation of instrumental uncertainties into our astrophysical constraints.

CHAPTER 2. BACKGROUND

Chapter 3

Detection of a Westward Hotspot Offset in the Atmosphere of a Hot Gas Giant CoRoT-2b

*This thesis chapter originally appeared in the literature as
Dang et al. 2018, Nature Astronomy*

Authors

Lisa Dang^{1,2,3}, Nicolas B. Cowan^{1,2,3,4}, Joel C. Schwartz^{1,2,3,4,5}, Emily Rauscher⁶, Heather Knutson⁷, Ian Dobbs-Dixon⁸, Micheal Line⁹, Drake Deming¹⁰, Sudarsan Sundararajan¹¹, Jonathan J. Fortney¹², and Ming Zhao¹³

¹ Department of Physics, McGill University, Montréal, QC, Canada

² McGill Space Institute (MSI), McGill University, Montréal, QC, Canada

³ Institut de Recherche sur les Exoplanètes (iREx), Université de Montréal, QC, Canada

⁴ Department of Earth & Planetary Sciences, McGill University, Montréal, Canada

⁵ Department of Physics & Astronomy, Northwestern University, USA

⁶ Department of Astronomy, University of Michigan, USA

⁷ Division of Geological & Planetary Sciences, California Institute of Technology, USA

⁸ New York University Abu Dhabi, UAE

⁹ School of Earth and Space Exploration, Arizona State University, USA

¹⁰ Department of Astronomy, University of Maryland, College Park, USA

¹¹ School of Engineering, Amrita Vishwa Vidyapeetham (Amrita University), India

¹² Department of Astronomy and Astrophysics, University of California, Santa Cruz, USA

Prologue

The first continuous infrared phase curve of a hot Jupiter, HD 189733b revealed a large phase amplitude and a *eastward* hot spot shift from the substellar point (Knutson et al. 2007). Subsequently, similar measurements have been acquired for a handful of hot Jupiter with varying phase amplitudes and *eastward* offsets. Intriguingly, an *eastward* hot spot shift on hot Jupiters had been predicted in 3D general circulation models a few years prior (Showman & Guillot 2002) as a result of fast eastward equatorial jets, a dominant dynamical feature that has since been reproduced independently by several hydrodynamical simulations (Heng & Showman 2015). In this chapter, I present $4.5 \mu\text{m}$ phase curve observations for a young hot Jupiter, CoRoT-2b where I report the first robust detection of a *westward* hot spot offset, calling into question our understanding of atmospheric dynamics on hot gas giants.

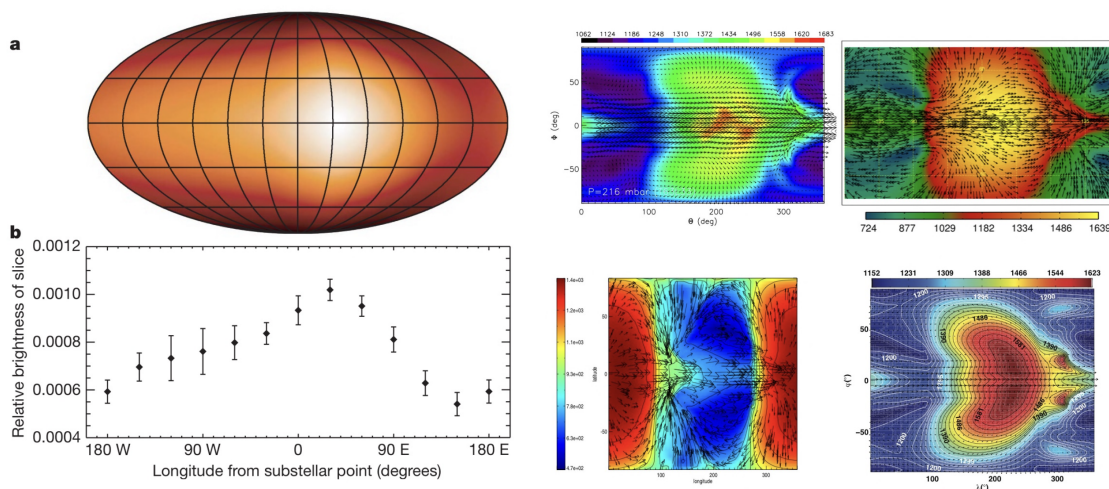


Figure 3.1: *Left:* Thermal map of HD 189733b inferred $8 \mu\text{m}$ phase curve observations from Knutson et al. 2007. *Right:* Example of general circulation models calculation for hot Jupiters from (Heng & Showman 2015) exhibiting eastward equatorial jets causing a shift of the hot spot.

Abstract

Short-period planets exhibit day–night temperature contrasts of hundreds to thousands of degrees K. They also exhibit eastward hotspot offsets whereby the hottest region on the planet is East of the substellar point (Knutson et al. 2007); this has been widely interpreted as advection of heat due to eastward winds (Showman & Guillot 2002). We present thermal phase observations of the hot Jupiter CoRoT-2b obtained with the IRAC instrument on the Spitzer Space Telescope. These measurements show the most robust detection to date of a *westward* hotspot offset of 23 ± 4 degrees, in contrast with the nine other planets with equivalent measurements (Cowan et al. 2012a; Knutson et al. 2012; Maxted et al. 2013; Zellem et al. 2014; Wong et al. 2015, 2016; Demory et al. 2016a; Stevenson et al. 2017). The peculiar infrared flux map of CoRoT-2b may result from westward winds due to non-synchronous rotation (Rauscher & Kempton 2014) or magnetic effects (Rogers & Komacek 2014; Rogers 2017), or partial cloud coverage, that obscures the emergent flux from the planet’s eastern hemisphere (Demory et al. 2013; Parmentier et al. 2016; Lee et al. 2016; Roman & Rauscher 2017). Non-synchronous rotation and magnetic effects may also explain the planet’s anomalously large radius (Guillot & Havel 2011; Rogers & Komacek 2014). On the other hand, partial cloud coverage could explain the featureless dayside emission spectrum of the planet (Moses et al. 2013; Wilkins et al. 2014). If CoRoT-2b is not tidally locked, then it means that our understanding of star–planet tidal interaction is incomplete. If the westward offset is due to magnetic effects, our result represents an opportunity to study an exoplanet’s magnetic field. If it has Eastern clouds, then it means that our understanding of large-scale circulation on tidally locked planets is incomplete.

3.1 Main Text

Amongst the plethora of known hot Jupiters, the CoRoT-2 system stands out from the rest for three reasons: its remarkably active host star, its unusual inflated radius, and its puzzling emission spectrum. In addition to these anomalous features, previous observations of the CoRoT-2 system show a gravitationally bound stellar companion candidate, 2MASS J19270636+0122577.

CoRoT-2b’s optical phase curve obtained by the *CoRoT* mission has previously been studied (Alonso et al. 2009; Snellen et al. 2010) and yielded an upper limit on the planet’s geometric albedo of 0.12. Later near-infrared (NIR) and mid-infrared (mid-IR) observations, acquired with ground-based (Alonso et al. 2010) and space-based

(Gillon et al. 2010; Deming et al. 2011; Wilkins et al. 2014) instruments, have shown that the planet’s emission spectrum could not be explained by conventional solar composition spectra or by a blackbody. Several scenarios were invoked to interpret the perplexing spectrum including the presence of silicate clouds affecting the mid-IR emission of the planet (Moses et al. 2013) and optically thick dayside clouds or a vertically isothermal atmosphere to explain the lack of features in the data acquired by the Wide Field Camera 3 (WFC3) on board of the Hubble Space Telescope (Wilkins et al. 2014).

We present new phase observations of the CoRoT-2 system (PID 11073; PI Cowan) acquired with the Infrared Array Camera (IRAC) on the Spitzer Space Telescope with the $4.5 \mu\text{m}$ channel on January 3–5, 2016. To minimize the impact of the visual companion in our analysis, we subtract it from our images. We combine the data into bins of 64 frames and detrend the lightcurve for detector systematics using various detrending strategies explained in more details in Methods.

We experiment with various decorrelation methods and fit for both the astrophysical models and the time-correlated systematics simultaneously. Most importantly, we find that the phase curve exhibits a westward hotspot offset. The offset is detected regardless of the planetary phase variation model, with and without imposing priors on the phase variation coefficients, and using the trimmed and untrimmed data. Additionally, we find the westward offset to be robust to the different photometry extraction schemes.

Our analysis shows a phase curve peak occurring 2.7 ± 0.4 hours after the time of secondary eclipse and a phase variation amplitude, from peak to trough, of $(4.3 \pm 0.2) \times 10^{-3}$. Using our observations, including two secondary eclipses and one transit, we measure a secondary eclipse depth, and transit depth of $(4.3 \pm 0.2) \times 10^{-3}$ and $(2.87 \pm 0.03) \times 10^{-2}$, respectively (see Supplementary Tables for the complete list of parameter values). We find a smaller eclipse depth than previously reported using channel 2 *Spitzer* IRAC data (Gillon et al. 2010; Deming et al. 2011). Our new measurement decreases the abnormally deep $4.5 \mu\text{m}$ planet-star contrast previously reported. Fitting the emission spectrum of the planet, we infer an optical geometric albedo of 0.08 ± 0.04 , which is consistent with the published upper limit using *CoRoT* data (Alonso et al. 2009; Snellen et al. 2010).

Full-orbit phase curves at $4.5 \mu\text{m}$ have so far been published for nine exoplanets on circular orbits—all of them exhibit phase offsets consistent with an eastward hotspot offset or no offset: WASP-12b (Cowan et al. 2012a), HD 189733b (Knutson et al. 2012), WASP-18b (Maxted et al. 2013), HD 209458b (Zellem et al. 2014), WASP-14b (Wong et al. 2015), WASP-19b (Wong et al. 2016), HAT-P-7b (Wong

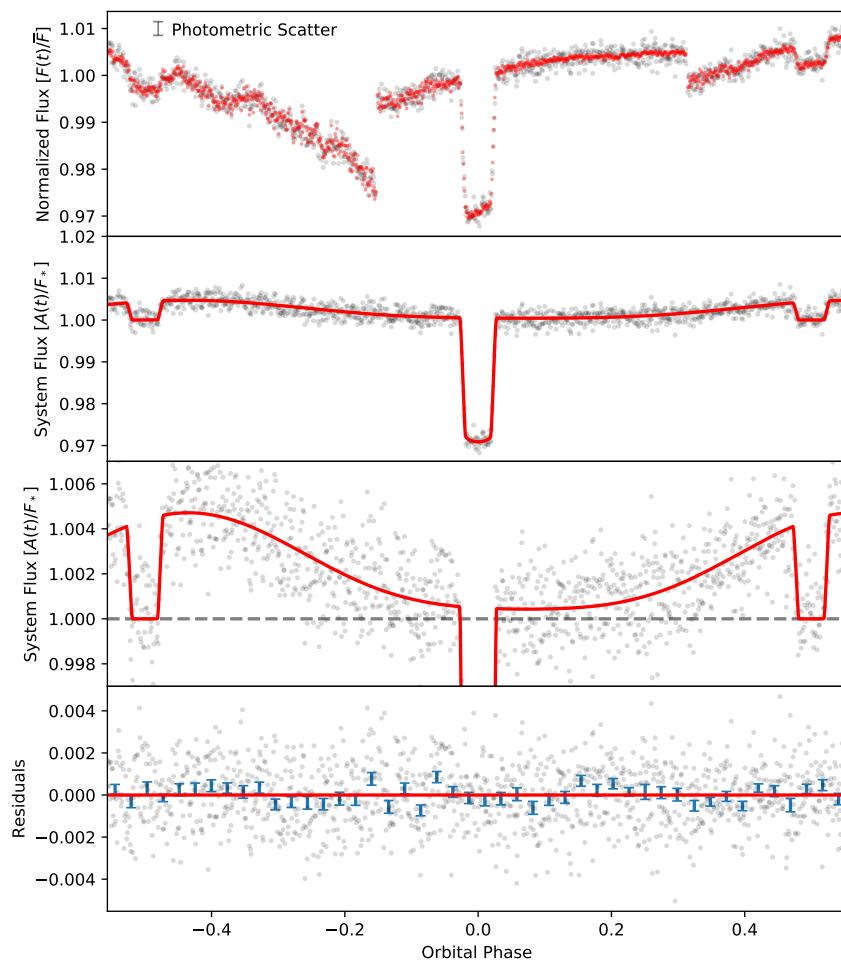


Figure 3.2: Fit model to Spitzer phase observation of CoRoT-2b. The top panel shows the normalized raw photometry obtained from *Spitzer* observations of the CoRoT-2 system (gray dots) and the fit with greatest Bayesian Evidence, instrumental systematics modeled as a 2^{nd} order polynomial and with no stellar variability (red dots). The error on the photometry measurements presented (top-left) is the photometric scatter, σ_F , which is estimated using a Markov Chain Monte Carlo (MCMC). The second panel shows the photometry corrected for detector systematics (gray dots) and the most probable astrophysical signal (red line). The third panel is a zoomed-in version of the second panel to better show the phase variation—we can see the peak of the phase variation occurring after the secondary eclipse. This corresponds to a *westward* offset of the brightest longitude on CoRoT-2b. The bottom panel shows the residuals obtained from subtracting the most probable astrophysical model from the corrected photometry (gray dots) and the binned residuals with a bin size of ~ 1 hour (blue points) and the errorbars are the error on the mean of each bin.

et al. 2016), 55 Cancri e (Demory et al. 2016a), and WASP-43b (Stevenson et al. 2017). The westward hotspot offset of 23 ± 4 degrees we measure for CoRoT-2b in the mid-IR therefore makes it unique. We note that another westward offset has previously been observed for Kepler-7b in optical *Kepler* data, attributed to reflected light from inhomogeneous clouds (Demory et al. 2013). We derive the longitudinal $4.5 \mu\text{m}$ brightness map of CoRoT-2b shown in Figure 2.

We derive the day-to-night heat recirculation efficiency, ϵ , and Bond albedo, A_B , of CoRoT-2b using all existing transit and eclipse depths in the infrared along with our best fit phase amplitude and offset, shown in Figure 3. Given the young age of the system (100–300 Mya) and the inflated radius of CoRoT-2b, we expect the planet to experience internal heating from residual heat of formation or tidal heating, but this should be dwarfed by the external heating of the star. The $\sim 35\%$ Bond albedo of CoRoT-2b shown in Figure 3.4 is greater than its low optical geometric albedo of $12 \pm 2 \%$ (Alonso et al. 2009; Snellen et al. 2010), suggesting significant NIR albedo, as reported for other hot Jupiters (Schwartz & Cowan 2015). The day–night temperature contrast is greater than has been inferred for HD 209458b (a hot Jupiter with similar irradiation temperature), suggesting that CoRoT-2b is less effective at transporting heat to its nightside.

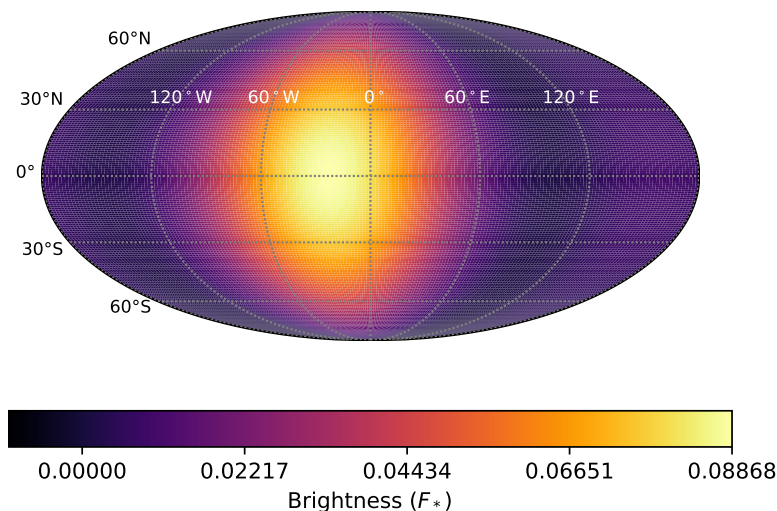


Figure 3.3: Surface brightness map of CoRoT-2b. This is the 1D longitudinal brightness obtained from the phase variations converted into a surface brightness map of CoRoT-2b. The surface brightness is scaled in units of stellar flux. The peak of the phase variation after the secondary eclipse shown in Fig. 3.2 corresponds to the westward offset of the brightest longitude on the planet.

The emission spectrum of CoRoT-2b has been difficult to understand since no

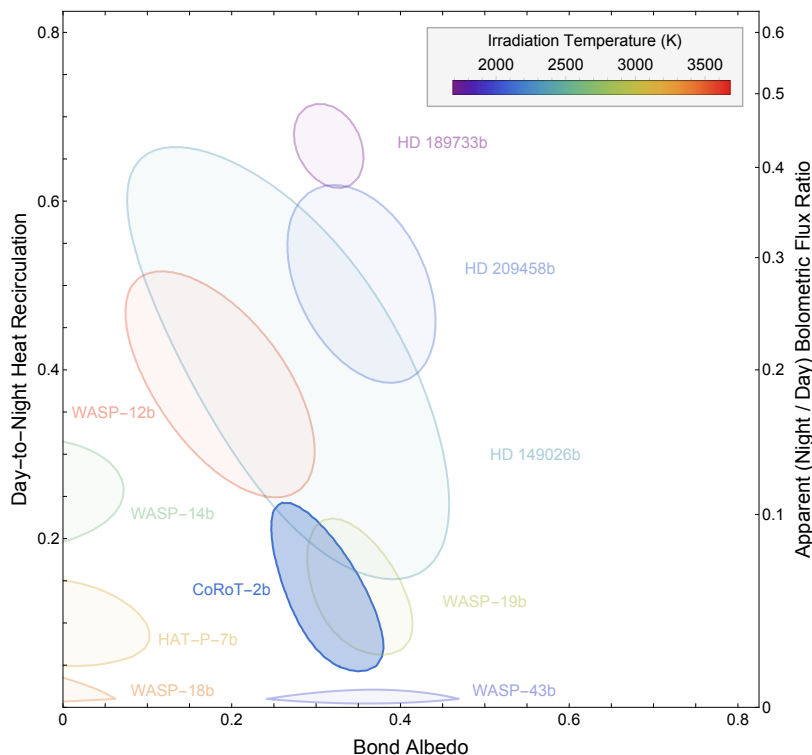


Figure 3.4: Energy budget of CoRoT-2b and other hot Jupiters. The 1σ confidence region for Bond albedo and day-to-night heat recirculation efficiency of CoRoT-2b and other hot Jupiters. The color of each region denotes the irradiation temperature. Given the day-night temperature difference, CoRoT-2b lies in the low-recirculation efficiency region.

spectral model could fit all the data within the uncertainties (Wilkins et al. 2014). Using our new measurement at $4.5 \mu m$, along with published eclipse depth measurements at other wavelengths, we fit a toy model including thermal emission and reflected light shown in Figure 4, described in Methods. The model with a geometric albedo of 0.12 ± 0.02 and dayside effective temperature of 1693 ± 17 K best fits the data with chi-squared per datum of 1.34.

Water vapor is expected in hot Jupiter’ atmospheres and therefore we expect to see water absorption features in *HST* data as well as at $4.5 \mu m$. However, these features are not apparent in the emission spectrum of CoRoT-2b which could mean one of two things: 1) wavelengths in and outside of H₂O bands are probing the same pressure or 2) they are probing a vertically isothermal region of the atmosphere. For example, optically thick clouds would prevent deeper observations into the atmosphere and could be responsible for the absence of water absorption features (Delorme et al. 2017). Alternatively, it would mean that infrared emission originates from a vertically

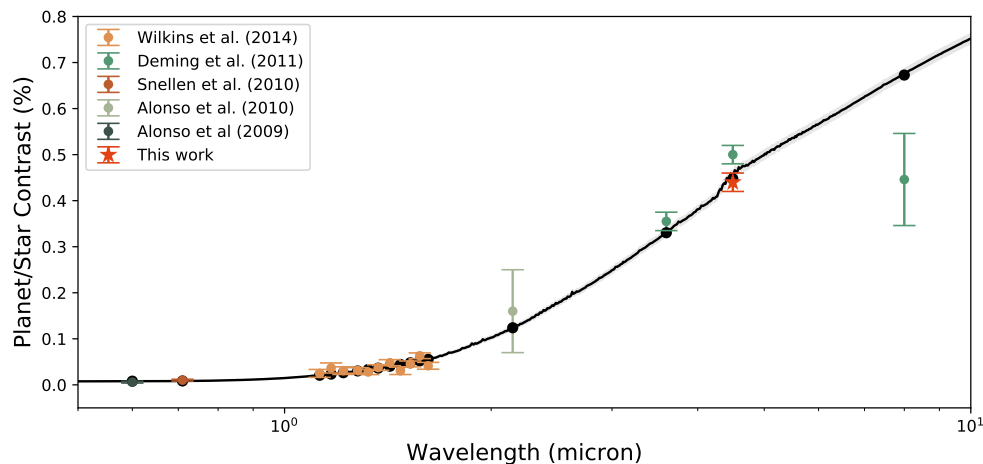


Figure 3.5: Dayside emission spectrum of CoRoT-2b. Our secondary eclipse depth and error, obtained from our fit using an MCMC, is shown along with previous measurements from *CoRoT* observations (Alonso et al. 2009; Snellen et al. 2010), *Spitzer* data (Deming et al. 2011), *HST*/WFC3 β results (Wilkins et al. 2014) and ground-based NIR measurement with their respective uncertainties (Alonso et al. 2010). The black line is the 1693 ± 17 K toy model with a geometric albedo of 0.12 ± 0.02 and the black dots are the band-integrated eclipse depths (per-datum $\chi^2 = 1.34$).

isothermal layer of the atmosphere.

Given that the irradiation temperature of CoRoT-2b is similar to that of HD 209458b, global circulation models predict an eastward hot spot shift, due to fast and broad equatorial jets at and near the photosphere (Showman & Guillot 2002). We propose three possible explanations for the westward offset seen on CoRoT-2b: 1) westward winds due to sub-synchronous rotation (Rauscher & Kempton 2014), 2) westward winds due to magnetic effects (Rogers & Komacek 2014; Rogers 2017), and/or 3) inhomogeneous clouds that are optically thick in the mid-IR (Demory et al. 2013; Parmentier et al. 2016; Lee et al. 2016; Roman & Rauscher 2017). In practice, these scenarios could be causally related, since spin rate affects wind direction (Rauscher & Kempton 2014), and wind direction affects cloud patterns (Lee et al. 2016; Roman & Rauscher 2017).

We note that the planetary photometry for CoRoT-2b exhibits a broad minimum rather than the distinct trough near or before transit seen in other phase curves. Sub-synchronous rotation not only produce westward atmospheric circulation, but the entire wind and temperature pattern is different than the standard eastward-jet

pattern. Simulation of HD 209458 b with sub-synchronous rotation also show a long minimum in the phase curve (Rauscher & Kempton 2015).

The high temperature of CoRoT-2b allows for collisional ionization of alkali metals in the atmosphere, hence creating a partially ionized atmosphere. The presence of a deep-seated magnetic field could create temporary directional winds causing atmospheric variability as seen on HAT-P-7b (Armstrong et al. 2016; Rogers 2017). We note that the host star is relatively young and spectrally active. CoRoT-2b is then subject to high X-ray and extreme ultraviolet flux (XUV) potentially leading to time-variable photo-ionization. While magnetism in the atmosphere of hot Jupiters is not yet understood, it is conceivable that the photo-ionization could also lead to time-variable coupling of the atmosphere with the magnetic dynamo of the planet. We estimate that the strength of the magnetic field needs to be $B \sim 230$ G to produce significant westward winds (see Supplementary Information). A recent study (Yadav & Thorngren 2017) found that some hot Jupiters with energetic interiors can have magnetic fields up to 250 G. Since an inflated radius suggests a high entropy interior, it is plausible that CoRoT-2b could have such a strong deep-seated magnetic field. Additionally, the coupling effect of magnetic drag can slow down wind speed (Menou 2012) which could explain the low heat redistribution efficiency, as well as the broad minimum in the light curve.

It is well established that some hot Jupiters have inhomogeneous clouds which produce non-trivial reflected phase variations (Demory et al. 2013). As previously mentioned, Kepler-7b’s optical phase curve exhibits a westward offset. Such observations can be caused by reflective clouds located west of the substellar meridian (Lee et al. 2016; Roman & Rauscher 2017) due to nightside clouds advected by the eastward jets. In contrast with Kepler-7b, CoRoT-2b would have western cloud coverage which require different aerosol formation and transportation mechanisms.

The equilibrium temperature of CoRoT-2b of 1521 ± 18 K allows for MnS, Cr and MgSiO₃ clouds to form on the dayside hemisphere (Parmentier et al. 2016). Inhomogeneous clouds covering the East and night side of the planet with particles large enough to block thermal emission at $4.5 \mu\text{m}$ could explain CoRoT-2b’s unusual phase curve (Delorme et al. 2017). Based on our current understanding, clouds tend to form on the cooler nightside hemisphere. Therefore, in the presence of westward winds, one would expect eastern cloud coverage (Lee et al. 2016). Alternatively, photochemical hazes (produced on the dayside) coupled with standard eastward jets could result in aerosols located east of the substellar point (Kempton et al. 2017). If inhomogeneous clouds are responsible for the shape of the phase curve, the dayside emission spectrum would be an average of a blackbody spectrum and a clear spectrum. This could explain why no spectral model, so far, could fit all the data within the

errors (Feng et al. 2016). However, if this is the case, it is possible that phase curves of other planets are also sculpted by clouds.

All three options are attractive because they might also explain other features of the planet. Asynchronous rotation can lead to tidal heating which, if deposited deep enough, can prevent contraction, explaining the inflated radius of CoRoT-2b (Arras & Socrates 2010). Magnetic effects are also attractive as they can explain the large temperature difference between the dayside and the nightside of the planet (Menou 2012) and the inflated radius (Yadav & Thorngren 2017). Partial cloud coverage is appealing because it may explain the anomalous dayside emission spectrum of the gas giant. It should be possible to distinguish between these scenarios with phase curve observations with wider spectral coverage including $4.5 \mu\text{m}$, either with both *Spitzer* channels or *JWST*. Non-synchronous rotation should have an impact on the phase curve at all wavelengths, while unusual cloud coverage may betray itself at short wavelengths dominated by reflected light or by spectral emission features. On the other hand, the circulation due to magnetic effects should be variable on an Alfvén timescale of $\tau_A \sim 23$ days (Armstrong et al. 2016; Rogers 2017) (see Methods for calculation), so a new phase curve at the same wavelength would show a different location for the peak.

The westward offset of CoRoT-2b is another example that hot Jupiters are not all cut from the same cloth and cannot be organized into a simple one-parameter family. More broadly, each scenario outlined above challenges our understanding of short period planets. If the westward hot spot offset is due to non-synchronous rotation, then our understanding of tidal interaction between planets and their host star is not fully understood. If magnetic effects are responsible for the unusual shape of the phase curve, our result would represent one of the few observable effects of a hot Jupiter’s magnetic field, allowing further understanding of the magnetic fields of hot Jovians. Lastly, if it is caused by Eastern clouds, then our understanding of large-scale atmospheric circulation on tidally locked planets is incomplete. Hence, an exhaustive understanding of these phenomena is necessary for the characterization of short-period planets, including the potentially habitable variety.

3.2 Methods

3.2.1 Data Source

We acquired observations of CoRoT-2b (Alonso et al. 2008) with the Infrared Array Camera (IRAC; Fazio et al. 2004) on the Spitzer Space Telescope (Werner et al. 2004)

with the $4.5 \mu\text{m}$ channel on January 3-5, 2016, during the *Post-Cryogenic Mission*. The system was observed for approximately 49 hours from shortly before a secondary eclipse to slightly after the next secondary eclipse. We used the subarray mode with 2.0 s exposures (1.92 s effective exposure time) to minimize the data volume and to make the observations as uniform as possible. This generated data cubes of 64 images with 32×32 pixel ($39'' \times 39''$) dimensions. Our observations were divided into 5 Astronomical Observation Requests (AORs) and includes a total of 1374 data cubes covering the full orbit of CoRoT-2. We elect to discard the first and last AOR containing 12 and 4 data cubes, respectively, since they are dithered, placing the target on different pixels than the rest of the data.

3.2.2 Data Reduction

We convert the pixel intensity from MJy/str to electron counts and mask bad pixels, i.e., 4σ outliers and *NaN* pixels. We discard all frames with containing a bad pixel in the vicinity of the target. Observations of CoRoT-2 ($K = 10.31$) (Cabrera et al. 2009) show the presence of a close-in visual companion, 2MASS J19270636+0122577 ($K = 12.03$) (Cutri et al. 2003). Due to the proximity of the companion, we experiment with various photometric extraction schemes to remove contamination from the companion and choose the strategy resulting the smallest RMS scatter. We then bin the data into bins of 64 frames before fitting the data (see the Supplementary Information for details about the data reduction and photometry extraction).

3.2.3 Astrophysical Model

We model the measured flux $F_{model}(t)$ as the product of the astrophysical signal $A(t)$ and the detector response \tilde{D} ,

$$F_{model}(t) = A(t) \times \tilde{D}. \quad (3.1)$$

Our astrophysical model is the sum of the emitted flux from the host star, F_* , and from the planet, F_p , as seen by a distant observer

$$A(t) = F_*(t) + F_p(t). \quad (3.2)$$

To model the occultations, we use the Python package `batman` (Kreidberg 2015). Using the quadratic limb-darkening model (Mandel & Agol 2002) supported by `batman`, we obtain the stellar intensity profile during transit $T(t)$. The secondary eclipse $E(t)$ is modeled using a uniform disk.

Stellar Model

CoRoT-2 is a young active star (100–300 Mya) (Schröter et al. 2011) with a rotational period P_* of 4.522 ± 0.024 days (Lanza et al. 2009). Unfortunately, the CoRoT-2 system was not visible from Earth at the time of the *Spitzer* observation, so stellar activity could not be monitored in real time. Typically, stellar variation due to star spots should not have a large effect in the mid-infrared, but given that CoRoT-2b is an active star with a short rotational period, it would be unwise to ignore stellar variability. We use optical observations acquired by *CoRoT* (Lanza et al. 2009) to estimate the magnitude of the stellar variation at $4.5\mu\text{m}$ on a 2 days time scale. We find that the stellar flux can vary by 1.1% (see Supplementary Information). We experiment with and without the inclusion of stellar variability to test the robustness of our fit.

The apparent stellar brightness is modeled as

$$F_*(t) = \Phi_*(t) + T(t) \quad (3.3)$$

where $\Phi_*(t)$ is the stellar variability and $T(t)$, as mentioned before is the transit curve. This is modeled as a sinusoid with a period equal to the rotational period of the host star

$$\Phi_*(t) = S_1 \cos\left(\frac{2\pi(t)}{P_*} - S_2\right) \quad (3.4)$$

where S_1 and S_2 are the semi-amplitude and the offset of the phase stellar variation model included as free parameters, respectively.

By construction, modeling the stellar variability as a sinusoid is not ideal for optimization purposes since this can lead to degeneracy between stellar and planetary model. In other words, both the phase variation model and the stellar variation model can mimic the shape of the planetary phase variation which explains the large uncertainty obtained for the fits which include a varying stellar brightness (see Supplementary Table 4 and 5). Although a few fits including stellar variability yield eastward offsets, they can be ruled out based on their significantly lower Bayesian Evidence, as described below.

Planetary Model

In the *batman* package, the time of secondary eclipse t_e is not an explicit parameter, instead it is defined as the time when true anomaly equals $3\pi/2 - \omega$, where ω is the longitude of periastron. We did not account for the light travel time as it is only a matter on 28.04 seconds and does not affect our analysis.

The planet’s flux is given by

$$F_p(t) = \Phi_p(t) \times E(t) \quad (3.5)$$

where $\Phi_p(t)$ is the phase variation and $E(t)$ is the secondary eclipse. In the `batman` package, the eclipse $E(t)$ is scaled such that the flux is unity during eclipse and the eclipse depth is given in terms of stellar flux. We re-scaled it such that $E(t) = 0$ during complete occultation and $E(t) = \delta_e$ outside of eclipse.

Previous studies have reported that the orbit of CoRoT-2b is nearly circular (Alonso et al. 2008; Gillon et al. 2010) and therefore the phase variation of the planet’s apparent brightness can be modeled (Cowan & Agol 2008) to first order as:

$$\Phi_p(t) = 1 + A \left[\cos \left(\frac{2\pi(t - t_e)}{P} \right) - 1 \right] + B \sin \left(\frac{2\pi(t - t_e)}{P} \right). \quad (3.6)$$

and to second order as:

$$\begin{aligned} \Phi_p(t) = 1 + A \left[\cos \left(\frac{2\pi(t - t_e)}{P} \right) - 1 \right] + B \sin \left(\frac{2\pi(t - t_e)}{P} \right) \\ + C \left[\cos \left(\frac{4\pi(t - t_e)}{P} \right) - 1 \right] + D \sin \left(\frac{4\pi(t - t_e)}{P} \right) \end{aligned} \quad (3.7)$$

where t_e is the time of eclipse center. Note that $\Phi_p(t_e) = 1$, which allows us to make the eclipse depth δ_e an explicit model variable.

3.2.4 Detector Models

Photometric data obtained using *Spitzer/IRAC* exhibit a well-studied instrumental effect due to intrapixel sensitivity variations (Charbonneau et al. 2005). The total number of electron counts varies with small changes in the position of the PSF of the target on the detector. The measured flux variation is dependent on both the sensitivity variation across the detector and the shape and position of the PSF. We experiment with various methods to decorrelate the astrophysical signal from the detector sensitivity. Although the PSF spans many pixels, most of the flux falls in the core of the PSF. Ultimately, we ignore the effect of the PSF widths σ_x and σ_y on the photometry.

2D Polynomial

Our first approach to correct the intrapixel sensitivity variation is to model the detector systematics as a n^{th} -degree polynomial in the centroid x_0 and y_0 :

$$\tilde{D}(x_0, y_0) = D_0 + \sum_{i=0}^n \sum_{j=0}^i c_{ij} (x_0 - \langle x_0 \rangle)^j (y_0 - \langle y_0 \rangle)^{i-j} \quad (3.8)$$

where n is the order of the polynomial. The model has $(n+1)(n+2)/2$ parameters and we experiment with polynomials of orders varying from 2 to 5. The shortcoming of this model is the requirement of accurate PSF location on the detector. As mentioned before, binning data improves the precision of centroid measurements. As we do not expect the location of the PSF to change significantly in ~ 2 minutes, it is sensible to bin the centroids by datacube.

BLISS Mapping

In recent years, many researchers have used BiLinear Interpolated Subpixel Sensitivity (BLISS) mapping (Stevenson et al. 2012; Ingalls et al. 2016; Schwartz & Cowan 2017). This non-parametric detector response model has the advantage of running quickly in a Markov-Chain-Monte-Carlo (MCMC) routine because the detector model has no explicit parameters. First, BLISS defines a set of locations on the pixel referred to as “knots”. Then, it divides the astrophysical model from the light curve at each step of the MCMC and averages the residuals surrounding each knot to obtain the detector sensitivity at each location. Finally, it uses the sensitivity values at the knots to interpolate the detector sensitivity $\tilde{D}(x_0, y_0)$ at each centroid.

Again, the drawback of this method is the necessity for accurate centroid measurements: a greater number of knots requires more precise centroid measurements. To mitigate the problem, we used binned centroids to obtain the detector sensitivity. Due to the relation between the inter-knot distance and the requirements for precised PSF location measurements, we chose a distance between the knots to be approximately the size of the centroid scatter within a datacube.

The shortcoming of such non-parametric models is that they do not properly marginalize over the detector uncertainty (Schwartz & Cowan 2017) and they have an indeterminate number of parameters which makes it difficult to assess the Bayesian evidence for the model as explained below.

Pixel-Level Decorrelation

Finally, we experiment with Pixel Level Decorrelation (PLD) (Deming et al. 2015; Ingalls et al. 2016) using a modified version of the systematics model. As mentioned earlier, the PSF of the target spans many pixels. One can express the total flux measurements as a general function of the pixels level fluxes. Astrophysical variations are expected to affect all pixels equally. Therefore, variations in the fraction of the total measured by each pixel are caused by the detector systematics such as variations in the telescope pointing, intra-pixel sensitivity variation, pixel coupling, and oscillation due to heating. Hence, one can express the detector sensitivity as a general function of the fraction to total flux recorded by each pixel.

We define the detector model as

$$\tilde{D}^t = \sum_{i=1}^N a_i \frac{P_i^t}{\sum_k^N P_k^t} \quad (3.9)$$

where N is the number of pixels used, a_i is the linear PLD coefficient for the i^{th} pixel and P_i is the value of the i^{th} pixel. In contrast with the original formulation of Deming et al. (2015), we elect to include \tilde{D}^t as a multiplicative factor rather than an additive factor since it describes the detector systematics more accurately. The difference between including the systematics as an additive term or a multiplicative factor is the $\delta A(t) \cdot \delta \tilde{D}^t$ cross-term which can be as large as $0.03 \cdot 0.005 = 0.00015$ (150 parts per million) for a 3% transit depth (Benneke et al. 2017).

Although our observations were acquired in staring mode, the telescope pointing can drift significantly in long time series observations. In our case, the image position on the detector varied by a third of a pixel, hence the first order PLD performed poorly compared to other decorrelation methods.

3.2.5 Model Fitting and Error Estimates

To estimate model parameters and their uncertainties, we use the package `emcee` (Foreman-Mackey et al. 2013), an Affine Invariant Markov Chain Monte Carlo (MCMC) implemented in Python. We use parameters from the literature (Alonso et al. 2008; Gillon et al. 2010) as an initial estimate of the astrophysical model. We use a Levenberg-Marquardt to estimate the detector coefficients from the residuals obtained after removing the initial astrophysical signal guess. We initialize 500 MCMC walkers with initial positions in parameter space distributed around the initial guess. We

define the likelihood function as

$$\ln L = -\frac{1}{2}\chi^2 - N_{dat} \ln \sigma_F \quad (3.10)$$

where σ_F is the photometric uncertainty which we make a jump parameter, N_{dat} is the number of data and χ^2 is the badness-of-fit which is defined as

$$\chi^2 = \frac{\sum_i [F_{data}(t) - F_{model}(t)]^2}{\sigma_F^2} \quad (3.11)$$

where F_{data} is the measured flux obtained from photometry. Since the measured flux varies by at most 4%, we adopt the same photometric uncertainty σ_F for the entire data set.

Each fit has a different burn in period for the MCMC. To ensure that our MCMC fit has converged, it has to satisfy the following criteria: 1) over the last 2000 MCMC steps of all the walkers, the likelihood of the best fit did not change and 2) over the last 2000 MCMC steps of all the walkers, the distribution the MCMC walker along each parameters was approximately constant. We find that depending on the complexity of model, the burn in period is about 4000 to 15000 steps for each MCMC walker.

Instead of using a covariance matrix to estimate the uncertainty on our parameter estimates, we marginalize over all the walkers over the last 2000 MCMC steps to get a posterior distribution for each jump parameter.

3.2.6 Priors

Our observations only include one orbit of CoRoT-2b which does not allow us to constrain astrophysical parameters such as the period, P , the semi-major axis, a , and the inclination, i , as precisely as values available in the literature. We therefore adopt informative priors for these parameters in the MCMC. We use the values and uncertainties obtained from 152 days of continuous observations of the system (Alonso et al. 2008) to impose Gaussian priors on a and i . Since the uncertainty on P is merely 0.0001% of the value, we choose to fix the period to reduce the number of jump parameters in our analysis.

The time of transit and secondary eclipse allows us to constrain $e \cos \omega$ while the relative duration of the transit and the secondary eclipse allows us to constrain $e \sin \omega$ (Charbonneau et al. 2005). While this puts a strong constrain on $e \cos \omega$, the duration of the occultations is usually too short to strongly constrain $e \sin \omega$. Since

eccentricity can only range between 0 and 1 and ω can be any value, we put a uniform prior on $e \cos \omega$ and $e \sin \omega$ ranging from -1 to 1.

Additionally, we specify priors on the limb-darkening coefficient. We consider quadratic limb-darkening where the stellar intensity $I(\mu)$ is described as

$$I(\mu)/I_0 = 1 - u_1(1 - \mu) - u_2(1 - \mu)^2 \quad (3.12)$$

where I_0 is the stellar intensity at the center of the disk, u_1 and u_2 are the limb-darkening coefficients and $\mu = \sqrt{1 - r^2}$ with r defined as the distance from the center of the disc. The common way to deal with limb darkening coefficients is to estimate the limb darkening coefficients prior to the fit and keep them fixed. The drawback is that the coefficients are dependent on the stellar atmosphere model adopted (Espinoza & Jordán 2015). Alternatively, one can make the coefficients jump parameters which is more statistically robust as it makes no assumption about the star; we chose the latter solution and to ensure that we make no assumption about the intensity profile of the host star while never exploring unphysical solutions, we used the following parametrization (Kipping 2013):

$$q_1 = (u_1 + u_2)^2, \quad (3.13)$$

$$q_2 = \frac{1}{2(u_1 + u_2)}, \quad (3.14)$$

with uniform prior on q_1 and q_2 ranging from 0 to 1, which the author claims to yield both realistic and robust uncertainties.

Most importantly, the full orbit phase curve of the system allows us to obtain a longitudinal surface brightness map of the planet (Cowan & Agol 2008). We use a physical prior rejecting models with phase variation coefficients that yield negative brightness at any longitude (Keating & Cowan 2017).

3.2.7 Model Comparison

Generally, a fit to data improves as we increase the number of model parameters. To compare the various astrophysical and detector models, we estimate the Bayesian Evidence by analogy with the Bayesian Information Criterion (BIC) (Schwarz 1978; Wit et al. 2012):

$$E = \ln L - \frac{N_{par}}{2} \ln N_{dat} = -\frac{\text{BIC}}{2} \quad (3.15)$$

where N_{par} is the number of model parameters. By this definition, a greater Bayesian evidence is preferred.

We experiment with various models: different detector models, planetary signature models, and the inclusion of stellar variability signatures. Although BLISS mapping is a non-parameteric model and therefore cannot be assigned a Bayesian Evidence, those fits yield lower log-likelihood than polynomials and therefore were ruled out as best fits. Comparing the Bayesian Evidence, we find 3 almost equivalently best models and 2 substantially good models ([Kass & Raftery 1995](#)):

- no stellar variability, 2nd order polynomial detector model, 2nd order phase variation, $E = 7695.64$ ($\Delta\text{BIC} = 0$)
- with stellar variability, 3th order polynomial detector model, 1st order phase variation, $E = 7695.14$ ($\Delta\text{BIC} = 1.00$)
- with stellar variability, 4th order polynomial detector model, 1st order phase variation, $E = 7694.62$ ($\Delta\text{BIC} = 2.04$)
- with stellar variability, 2nd order polynomial detector model, 2st order phase variation, $E = 7693.52$ ($\Delta\text{BIC} = 4.24$)
- with stellar variability, 2nd order polynomial detector model, 1st order phase variation, $E = 7693.49$ ($\Delta\text{BIC} = 4.30$)

where ΔBIC is the difference in BIC compared to the fit with lowest BIC, and by analogy with greatest Bayesian Evidence. Fits with a $\Delta\text{BIC} > 6$ can be strongly ruled out as best-fits ([Kass & Raftery 1995](#)). The most probable parameters, log-likelihood, and Bayesian Evidence values for each models are reported in Supplementary Table 2, 3, 4, and 5; the best fits are highlighted. All five models favor a westward hotspot offset on the planet, but with varying significance.

Since the Bayesian Evidence does not allow us to discern which of the 5 is the best model, we elect to look at the in-eclipse portion of the lightcurve to discriminate between the models. The in-eclipse portions of the phase curve should be unity once we remove the detector systematics and stellar variability. Fitting a linear function to the in-eclipse segments of the corrected lightcurves, we find the model in which we assumed no stellar variability to be the most consistent with the absence of a trend: the linear fits to the first and second eclipses have slopes of $-0.009 \pm$

0.013 and -0.003 ± 0.01 , respectively (see Supplementary Figures 10, 11, and 12 in Supplementary Figures). Since the in-eclipse flatness test favors the model with stable stellar flux over the models with the inclusion of stellar variability, it suggests that the models with stable stellar flux is a better representation of the underlying astrophysics.

As mentioned previously, the inclusion of a sinusoidal stellar variation model can introduce degeneracy as seen in Supplementary Tables 4 and 5 which can lead to less consistent parameter estimates and larger uncertainties. As a sanity check, we include a fit performed using an entirely independent photometry and fitting pipeline (Zhang et al. 2018). Using a higher-order PLD method coupled with a linear trend as model for the stellar variability, we find a westward offset of 25.6 ± 1.9 degrees, confirming the westward offset obtained with the first pipeline.

Note, moreover, that all of the models exhibit a slightly declining flux during eclipse which is consistent with the fit obtained using the higher-order PLD pipeline. This suggests that if anything, we are slightly underestimating the magnitude of the westward hotspot offset: if the eclipse bottom were flat, then the flux would be even greater after eclipse.

3.2.8 Surface Brightness Map

Due to the orbital motion and rotation of the planet, the region of the planet facing us changes over time. One can translate the phase variation of the planet as seen from a distant observer into a longitudinal brightness map of the planet. We map the surface brightness of CoRoT-2b (Cowan & Agol 2008) (see Supplementary Information) and see a clear westward offset of 23 ± 4 degrees.

In the case of a non-synchronously rotating planet, the same formalism can be used to obtain the longitudinal brightness of the planet, but the longitude would correspond to stellar zenith angle (Cowan et al. 2012b).

3.2.9 Energy Budget

Thermal phase variations of short-period planet constrain the day-to-night heat recirculation efficiency of the atmosphere (Cowan & Agol 2011b; Perez-Becker & Showman 2013; Schwartz & Cowan 2015).

Using published eclipse and transit depths, including ours, along with the phase curve amplitude and offset, we obtain the dayside and nightside brightness temper-

atures with the inverse Planck function. We constrain the Bond albedo and recirculation efficiency from the derived effective dayside and nightside temperature shown in Figure 3 (Cowan & Agol 2011b; Stevenson et al. 2017).

3.2.10 Emission Spectroscopy

We used a toy emission spectrum model accounting for the contribution from reflected light, $F_{reflected}$, and thermal emission, $F_{thermal}$ to describe the planet’s emission spectrum. We model the emission spectrum of the host star, $F_*(\lambda)$, using the Kurucz Atlas from the `pysynphot` package (STScI Development Team 2013) with an effective temperature of $T_* = 5625$ K, a metallicity $[\text{Fe}/\text{H}] = 0$, and a surface gravity $\log g = 4.71$. The emission spectrum of the planet as the sum of thermal emission and reflected light (Keating & Cowan 2017):

$$F_p(\lambda) = \left(\frac{R_p}{R_*}\right)^2 B_\lambda(T_{day}, \lambda) + \frac{A_g}{(a/R_*)^2} \left(\frac{R_p}{R_*}\right)^2 F_*(\lambda) \quad (3.16)$$

where T_{day} is the effective dayside emission and A_g is the geometric albedo of the planet. Using `emcee`, we fit the presented model to CoRoT-2b’s emission spectrum and we find that the model with a geometric albedo, A_g , of 0.12 ± 0.02 and dayside effective temperature of 1693 ± 17 K best fits the data with chi-squared per datum, χ_{dat} , of 1.34. We note that our eclipse depth measurement at $4.5 \mu\text{m}$ is shallower than that reported using observation taken during the cryogenic *Spitzer* era (Gillon et al. 2010; Deming et al. 2011). This discrepancy may be due to improvements observational in strategies and self-calibration techniques over time (Hansen et al. 2014; Ingalls et al. 2016).

3.2.11 Constraint on Magnetic Field Strength of CoRoT-2b

To estimate the lower limit on the magnetic strength of CoRoT-2b’s dynamo required to explain westward winds, we calculate the ionization fraction, χ_e . The importance of the effect of magnetism on zonal winds can be approximated as the ratio of magnetic to wave timescales τ_{mag}/τ_{wave} . The magnetic timescale if defined as

$$\tau_{mag} = \frac{4\pi\rho\eta}{B^2} \quad (3.17)$$

where ρ is the density, η is the magnetic diffusivity, B is the magnetic field strength, g is the gravity. Hence, we can define the lower limit of $B \sim \sqrt{4\pi\rho\eta/\tau_{wave}}$, i.e. when $\tau_{mag}/\tau_{wave} \sim 1$. The magnetic diffusivity is defined as (Rogers 2017)

$$\eta = 230\sqrt{T}/\chi_e \quad (3.18)$$

where χ_e is the ionization fraction given which we evaluate using a simplified Saha equation that only accounts for potassium (Perna et al. 2010):

$$\chi_e = 6.47 \times 10^{-13} \left(\frac{a_K}{10^{-7}} \right)^{1/2} \left(\frac{T}{10^3} \right)^{3/4} \left(\frac{2.4 \times 10^{15}}{n_n} \right)^{1/2} \frac{\exp(-25188/T)}{1.15 \times 10^{-11}} \quad (3.19)$$

where a_K is the abundance of potassium, T is the dayside temperature of the planet, and n_n is the number density of neutrals and is defined as $n_n = \rho/\bar{m}$ where \bar{m} is the molecular mass of hydrogen.

So, assuming that the planet is mainly made of molecular hydrogen with a gas constant of $R = 3523 \text{ J/kg} \cdot \text{K}$, we calculate a density of $\rho = P/RT = 1.635 \times 10^{-5} \text{ g/cm}^3$ at a pressure of $P = 1 \text{ bar}$ and a temperature $T = 1736 \text{ K}$. Therefore, we get a number density of neutrals of $n_n = \rho/\bar{m} = 4.89 \times 10^{18}$. Approximating a potassium abundance of $a_K = 10^{-7}$, we find an ionization fraction of 9.41×10^{-10} and magnetic diffusivity of $\eta = 1.02 \times 10^{13}$. The wave timescale is defined as

$$\tau_{wave} = \frac{L}{\sqrt{gH}} \quad (3.20)$$

where L is the characteristic length scale of the horizontal flow, $g = 4185 \text{ cm/s}^2$ is the gravity, and H is the depth of the atmosphere. Approximating the characteristic length scale as $L \sim r_p$, where $r_p = 1.06 \times 10^8 \text{ m}$, and calculating $H = kT/\bar{m}g$, where k is the Boltzmann constant, we calculate a wave timescale of $\tau_{wave} = 3.83 \times 10^4$ seconds.

Using the derived values of ρ , η , and τ_{wave} above, we find a lower limit on the magnetic field strength of $B \sim 230 \text{ G}$ to cause atmospheric variability. We note that this is a rough estimation of the planet's magnetic field, better constraints would require magnetohydrodynamic simulations.

Additionally, the circulation should be variable on an Alfvén timescale (Rogers 2017), $\tau_A = a/v_A$, where a is a characteristic scale of the system and v_A is the Alfvén

velocity. We calculate the Alfvén velocity defined as $v_A = B/\sqrt{\mu_0\rho}$, where μ_0 is the permeability of vacuum. Approximating as $a \sim \pi r_p$ and using the density ρ derived above, we obtain a timescale of $\tau_A \sim 23$ days.

Data Availability Statement

Individual fit parameters and uncertainties using various models are provided in the Supplementary Information. Any other data that support the plots within this paper and other findings of this study are available from the corresponding author upon reasonable request.

Correspondence and Requests

Correspondence and requests for materials should be addressed to L.D.

Acknowledgements

L.D. thanks Sean Carey, James Ingalls, and William Glaccum from the Spitzer IRAC team for the helpful discussions that contributed to the reduction of the data. Funding for this work was provided in part by the Natural Sciences and Engineering Research Council of Canada (NSERC) discovery grant and the California Institute of Technology’s Infrared Processing and Analysis Center (Caltech/IPAC) Visiting Graduate Research Fellowship. Work by S. S. was funded by the Google Summer of Code program. This work is based on observations made with the Spitzer Space Telescope, which is operated by the Jet Propulsion Laboratory, California Institute of Technology under a contract with NASA. Support for this work was provided by NASA through an award issued by JPL/Caltech.

Facilities: Spitzer Space Telescope ([Werner et al. 2004](#)), Infrared Array Camera ([Fazio et al. 2004](#))

Software: Numpy ([van der Walt et al. 2011](#)), Scipy ([van der Walt et al. 2011](#)), Astropy ([Astropy Collaboration et al. 2013](#)), Matplotlib ([Hunter 2007](#)), Emcee ([Foreman-Mackey et al. 2013](#)), Batman ([Kreidberg 2015](#)), Corner ([Foreman-Mackey 2016](#)), Jupyter ([Perez & Granger 2007](#)), pysynphot ([STScI Development Team 2013](#))

Author contributions statement

L.D. extracted the photometric measurements from the data, detrended the data, developed and fit the phase curve models, led the analysis and wrote the manuscript. N.B.C. is the P.I. of the successful Spitzer proposal from which we obtained the observations and contributed to the writing of the manuscript. J.C.S contributed materials to the main text. E.R. contributed to the interpretation for the results and to the discussion. M.Z. and H.K. verified the robustness of the analysis and contributed to the interpretation of results. S.S. contributed to the photometric measurements pipeline. J.C.S., E.R, H.K., I.D., M.L., D.D., J.J.F., and M.Z. are co-I.'s of the successful Spitzer proposal from which we obtained the observations. All authors commented on the manuscript.

Additional information

Supplementary information is available for this paper.

Competing Interests

The authors declare no competing financial interests.

3.3 Supplementary Tables

CHAPTER 3. THERMAL PHASE CURVE OF COROT-2B

Name	Symbol	Constraint	Reference
<i>Fitted</i>			
Time of transit (days from start of observations *)	t_0	–	–
Radius of planet	R_p/R_*	–	–
Semi-major axis	a/R_*	6.70 ± 0.03	Alonso et al. (2008)
Orbital inclination (degrees)	i	87.84 ± 0.1	Alonso et al. (2008)
Orbital eccentricity	e	$[0, 1]$	–
Longitude of periastron	ω	$[0, 2\pi]$	–
Limb darkening coefficient	q_1	$[0, 1]$	Kipping (2013)
Limb darkening coefficient	q_2	$[0, 1]$	Kipping (2013)
Eclipse depth (F_p/F_*)	δ_e	$[0, 1]$	–
Phase variation even coefficient (1 st order)	A	$F_p \geq 0$	Keating & Cowan (2017)
Phase variation odd coefficient (1 st order)	B	$F_p \geq 0$	Keating & Cowan (2017)
Phase variation even coefficient (2 nd order)	C	$F_p \geq 0$	Keating & Cowan (2017)
Phase variation odd coefficient (2 nd order)	D	$F_p \geq 0$	Keating & Cowan (2017)
Stellar variation even coefficient (1 st order)	S_1	–	–
Stellar variation odd coefficient (1 st order)	S_2	–	–
<i>Fixed</i>			
Orbital period (days)	P	1.7429964	Alonso et al. (2008)
Rotational period of the host star (days)	P_*	4.522	Lanza et al. (2009)
<i>Derived</i>			
Phase Amplitude (units of Stellar Flux)	A_p	–	–
Phase Offset (in rad)	Φ_p	–	–

Table 3.1: Astrophysical Model Parameters. Note that positive values of Φ_p corresponds to peak occurring after eclipse.

Parameter	Poly2	Poly3	Poly4	Poly5	PLD1	BLISS
t_0	1.0744 ^{+20.1353} _{-20.1353}	1.0744 ^{+0.0002} _{-0.0002}	1.0744 ^{+0.0002} _{-0.0002}	1.0745 ^{+0.0002} _{-0.0002}	1.0746 ^{+0.0002} _{-0.0002}	1.0745 ^{+0.0002} _{-0.0002}
R_p/R_*	0.1698 ^{+0.0008} _{-0.0009}	0.1692 ^{+0.0009} _{-0.001}	0.1689 ^{+0.001} _{-0.001}	0.1689 ^{+0.0009} _{-0.001}	0.1694 ^{+0.0012} _{-0.0013}	0.1685 ^{+0.001} _{-0.001}
a/R_*	6.6843 ^{+0.0237} _{-0.0238}	6.6848 ^{+0.0248} _{-0.0247}	6.6868 ^{+0.0246} _{-0.0265}	6.6891 ^{+0.0243} _{-0.0244}	6.6991 ^{+0.0252} _{-0.0253}	6.6858 ^{+0.0241} _{-0.0246}
i	87.8598 ^{+0.0926} _{-0.0909}	87.8639 ^{+0.0917} _{-0.0897}	87.8603 ^{+0.0969} _{-0.0949}	87.8592 ^{+0.0944} _{-0.0917}	87.8411 ^{+0.0922} _{-0.0954}	87.8626 ^{+0.0928} _{-0.0922}
$e \cos \omega$	-1.6e - 05 ^{+0.000373} _{-0.000388}	1e - 05 ^{+0.000365} _{-0.000355}	2.3e - 05 ^{+0.000409} _{-0.000393}	9e - 06 ^{+0.000376} _{-0.000398}	-4e - 06 ^{+0.000356} _{-0.000361}	-1e - 06 ^{+0.000489} _{-0.000493}
$e \sin \omega$	-0.0 ^{+0.000384} _{-0.000377}	-5e - 06 ^{+0.000334} _{-0.000334}	7e - 06 ^{+0.000394} _{-0.000386}	1e - 06 ^{+0.000375} _{-0.000398}	-8e - 06 ^{+0.000359} _{-0.000366}	-1e - 05 ^{+0.000493} _{-0.000497}
q_1	0.0112 ^{+0.0162} _{-0.0074}	0.0129 ^{+0.0189} _{-0.0087}	0.0147 ^{+0.0228} _{-0.0099}	0.0151 ^{+0.0228} _{-0.0101}	0.0227 ^{+0.0314} _{-0.0146}	0.0161 ^{+0.0216} _{-0.0103}
q_2	0.3211 ^{+0.3796} _{-0.2341}	0.3071 ^{+0.3943} _{-0.228}	0.254 ^{+0.3774} _{-0.1892}	0.2686 ^{+0.3938} _{-0.2023}	0.3494 ^{+0.3923} _{-0.2506}	0.2913 ^{+0.3692} _{-0.2149}
δ_e	0.0045 ^{+0.0002} _{-0.0002}	0.0046 ^{+0.0002} _{-0.0002}	0.0044 ^{+0.0002} _{-0.0002}	0.0044 ^{+0.0002} _{-0.0002}	0.0042 ^{+0.0002} _{-0.0002}	0.0044 ^{+0.0002} _{-0.0002}
A	0.3984 ^{+0.008} _{-0.009}	0.3921 ^{+0.0097} _{-0.0194}	0.3908 ^{+0.0101} _{-0.0115}	0.3907 ^{+0.0117} _{-0.0135}	0.3972 ^{+0.0113} _{-0.0125}	0.3923 ^{+0.0124} _{-0.0141}
B	0.2415 ^{+0.0246} _{-0.0245}	0.2498 ^{+0.0251} _{-0.0267}	0.2567 ^{+0.0281} _{-0.0286}	0.2474 ^{+0.0319} _{-0.0317}	0.2368 ^{+0.0348} _{-0.0359}	0.2382 ^{+0.0341} _{-0.0354}
σ_F	0.00149 ^{+3e-05} _{-2.9e-05}	0.001474 ^{+3.1e-05} _{-2.9e-05}	0.001468 ^{+3.1e-05} _{-3e-05}	0.001461 ^{+3e-05} _{-2.9e-05}	0.0021 ^{+0.0} _{-0.0}	0.0016 ^{+0.0} _{-0.0}
$\log(L)$	7741.73	7758.25	7765.04	7775.53	7296.34	7684.27
E	7677.28	7679.48	7668.37	7657.37	7221.15	---
$\log(L)^\dagger$	339938.37	340400.45	340611.54	340528.36	314954.3	337867.36
E Unbinned	339836.54	340276.0	340458.8	340341.68	314835.69	---
A_p	0.0042 ^{+0.0002} _{-0.0002}	0.0042 ^{+0.0002} _{-0.0002}	0.0041 ^{+0.0002} _{-0.0002}	0.0041 ^{+0.0002} _{-0.0002}	0.0039 ^{+0.0002} _{-0.0002}	0.004 ^{+0.0002} _{-0.0002}
Φ_p	0.544 ^{+0.0503} _{-0.0566}	0.5692 ^{+0.0629} _{-0.0503}	0.5818 ^{+0.0629} _{-0.0629}	0.5629 ^{+0.0692} _{-0.0692}	0.5378 ^{+0.0818} _{-0.0755}	0.544 ^{+0.0755} _{-0.0755}

Table 3.2: Fit parameters using a first order Fourier series to model the phase variation without stellar variation for different detector models. Most probable astrophysical parameter estimates obtained from posterior probability distribution from the MCMC routine using various systematics models. The planetary brightness phase variation is modeled as a first order Fourier series and the model assumes no stellar variability. The largest value of $\log L$ and E for both binned and unbinned data are in bold blue. The errors on the parameters are the 68% confidence region bounds of the posterior distribution obtained from `emcee`.

Parameter	Poly2	Poly3	Poly4	Poly5	PLD1	BLISS
t_0	1.0744 ^{+0.0002} _{-0.0002}	1.0744 ^{+0.0002} _{-0.0002}	1.0744 ^{+0.0002} _{-0.0002}	1.0745 ^{+0.0002} _{-0.0002}	1.0746 ^{+0.0002} _{-0.0002}	1.0744 ^{+0.0002} _{-0.0002}
R_p/R_*	0.1696 ^{+0.0009} _{-0.0009}	0.1691 ^{+0.0009} _{-0.0009}	0.1689 ^{+0.0009} _{-0.0009}	0.1688 ^{+0.0009} _{-0.0009}	0.1702 ^{+0.0011} _{-0.0012}	0.1686 ^{+0.001} _{-0.001}
a/R_*	6.6792 ^{+0.0249} _{-0.024}	6.6821 ^{+0.0238} _{-0.0246}	6.6867 ^{+0.0237} _{-0.0244}	6.6856 ^{+0.0243} _{-0.0247}	6.6946 ^{+0.0251} _{-0.0257}	6.6837 ^{+0.0244} _{-0.025}
i	87.8684 ^{+0.0929} _{-0.0923}	87.8671 ^{+0.0937} _{-0.09}	87.8686 ^{+0.0915} _{-0.0945}	87.8645 ^{+0.0966} _{-0.093}	87.8405 ^{+0.092} _{-0.0922}	87.8694 ^{+0.092} _{-0.0926}
$e \cos \omega$	-0.0 ^{+0.0004} _{-0.0004}	-0.0 ^{+0.0003} _{-0.0004}	-0.0 ^{+0.0003} _{-0.0004}	0.0 ^{+0.0004} _{-0.0004}	0.0 ^{+0.0003} _{-0.0003}	-0.0 ^{+0.0005} _{-0.0005}
$e \sin \omega$	0.0 ^{+0.0004} _{-0.0004}	-0.0 ^{+0.0004} _{-0.0004}	0.0 ^{+0.0004} _{-0.0004}	-0.0 ^{+0.0004} _{-0.0004}	0.0 ^{+0.0003} _{-0.0003}	-0.0 ^{+0.0005} _{-0.0005}
q_1	0.0133 ^{+0.0178} _{-0.0087}	0.0129 ^{+0.0196} _{-0.0085}	0.0133 ^{+0.0182} _{-0.0089}	0.015 ^{+0.0207} _{-0.01}	0.0205 ^{+0.0271} _{-0.0131}	0.0158 ^{+0.0231} _{-0.0103}
q_2	0.2957 ^{+0.3059} _{-0.2192}	0.2951 ^{+0.3034} _{-0.2149}	0.2889 ^{+0.3688} _{-0.2103}	0.2842 ^{+0.3695} _{-0.2112}	0.38 ^{+0.385} _{-0.2688}	0.2874 ^{+0.3852} _{-0.2132}
δ_e	0.0044 ^{+0.0002} _{-0.0002}	0.0046 ^{+0.0002} _{-0.0002}	0.0045 ^{+0.0002} _{-0.0002}	0.0044 ^{+0.0002} _{-0.0002}	0.0048 ^{+0.0002} _{-0.0002}	0.0045 ^{+0.0002} _{-0.0002}
A	0.4443 ^{+0.0133} _{-0.0148}	0.4257 ^{+0.0187} _{-0.0195}	0.4325 ^{+0.0171} _{-0.0196}	0.427 ^{+0.0194} _{-0.0215}	0.3745 ^{+0.0212} _{-0.0213}	0.422 ^{+0.0198} _{-0.0223}
B	0.1934 ^{+0.0341} _{-0.0324}	0.1647 ^{+0.0355} _{-0.0346}	0.1754 ^{+0.0411} _{-0.039}	0.1775 ^{+0.0474} _{-0.0446}	0.1322 ^{+0.0319} _{-0.0298}	0.1748 ^{+0.0459} _{-0.0443}
C	0.0669 ^{+0.0132} _{-0.013}	0.0802 ^{+0.015} _{-0.0163}	0.0756 ^{+0.016} _{-0.0154}	0.0746 ^{+0.0182} _{-0.0189}	0.1096 ^{+0.0135} _{-0.014}	0.0784 ^{+0.018} _{-0.0187}
D	0.0681 ^{+0.0117} _{-0.012}	0.0627 ^{+0.0134} _{-0.0152}	0.0628 ^{+0.0141} _{-0.0154}	0.0638 ^{+0.0174} _{-0.0177}	0.1096 ^{+0.0135} _{-0.014}	0.0715 ^{+0.0163} _{-0.0177}
σ_F	0.001461 ^{+2.9e-05} _{-2.9e-05}	0.001454 ^{+3e-05} _{-2.9e-05}	0.001448 ^{+2.9e-05} _{-2.9e-05}	0.001446 ^{+2.9e-05} _{-2.9e-05}	0.002013 ^{+4e-05} _{-3.9e-05}	0.001536 ^{+3.1e-05} _{-3e-05}
$\log(L)$	7767.25	7776.56	7784.37	7785.60	7350.24	7700.07
E	7695.64	7690.63	7680.54	7660.28	7267.89	--
$\log(L)$ Unbinned	340798.6	340917.09	341131.14	340976.52	317233.61	338357.01
E Unbinned	340685.46	340781.32	340967.09	340778.52	317103.7	--
A_p	0.0043 ^{+0.0002} _{-0.0002}	0.0042 ^{+0.0002} _{-0.0002}	0.0042 ^{+0.0002} _{-0.0002}	0.0041 ^{+0.0002} _{-0.0002}	0.004 ^{+0.0002} _{-0.0002}	0.0041 ^{+0.0003} _{-0.0003}
Φ_p	0.412 ^{+0.0629} _{-0.0566}	0.3491 ^{+0.0632} _{-0.0692}	0.3679 ^{+0.0755} _{-0.0755}	0.3742 ^{+0.0881} _{-0.0943}	0.3365 ^{+0.0629} _{-0.0629}	0.3805 ^{+0.0881} _{-0.0881}

Table 3.3: Fit parameters using a second order Fourier series to model the phase variation without stellar variation for different detector models. Most probable astrophysical parameters estimates obtained from posterior probability distribution from the MCMC routine using various systematics models. The planetary brightness phase variation is modeled as a second order Fourier series and the model assumes no stellar variability. The highlighted fit yields the greatest Bayesian Evidence. The largest value of $\log L$ and E for both binned and unbinned data are in bold blue. The errors on the parameters are the 68% confidence region bounds of the posterior distribution obtained from *emcee*.

Parameter	Poly2	Poly3	Poly4	Poly5	PLD1	BLISS
t_0	$1.0744^{+0.0002}_{-0.0002}$	$1.0744^{+0.0002}_{-0.0002}$	$1.0745^{+0.0002}_{-0.0002}$	$1.0745^{+0.0002}_{-0.0002}$	$1.0746^{+0.0002}_{-0.0002}$	$1.0745^{+0.0002}_{-0.0002}$
R_p/R_*	$0.1693^{+0.0009}_{-0.0009}$	$0.1687^{+0.0009}_{-0.001}$	$0.1683^{+0.0009}_{-0.0009}$	$0.1684^{+0.0009}_{-0.001}$	$0.169^{+0.0012}_{-0.0012}$	$0.1678^{+0.001}_{-0.001}$
a/R_*	$6.6805^{+0.0242}_{-0.0235}$	$6.6824^{+0.0231}_{-0.0248}$	$6.6883^{+0.0249}_{-0.0242}$	$6.6881^{+0.024}_{-0.0237}$	$6.6929^{+0.0249}_{-0.0257}$	$6.6842^{+0.0247}_{-0.0242}$
i	$87.8783^{+0.0916}_{-0.0935}$	$87.8717^{+0.0908}_{-0.0918}$	$87.8616^{+0.0853}_{-0.0906}$	$87.8593^{+0.0843}_{-0.0929}$	$87.8499^{+0.0921}_{-0.0904}$	$87.8652^{+0.0918}_{-0.0929}$
$e \cos \omega$	$-3e - 06^{+0.000398}_{-0.000393}$	$2.3e - 05^{+0.000388}_{-0.000382}$	$-1.4e - 05^{+0.000479}_{-0.000451}$	$-2.4e - 05^{+0.000467}_{-0.000492}$	$-5e - 06^{+0.000398}_{-0.000401}$	$-5e - 06^{+0.000554}_{-0.000555}$
$e \sin \omega$	$7e - 06^{+0.000405}_{-0.000399}$	$1.8e - 05^{+0.000382}_{-0.000383}$	$-1e - 06^{+0.000442}_{-0.000446}$	$2e - 06^{+0.000461}_{-0.000451}$	$-1e - 05^{+0.000407}_{-0.000397}$	$-6e - 06^{+0.000558}_{-0.000561}$
q_1	$0.0137^{+0.0202}_{-0.0201}$	$0.0146^{+0.0202}_{-0.0208}$	$0.0145^{+0.0194}_{-0.0194}$	$0.0144^{+0.0197}_{-0.0194}$	$0.0231^{+0.0284}_{-0.0147}$	$0.0163^{+0.0223}_{-0.0106}$
q_2	$0.2917^{+0.3798}_{-0.2135}$	$0.2688^{+0.3909}_{-0.1969}$	$0.2643^{+0.3814}_{-0.1963}$	$0.2748^{+0.39}_{-0.2033}$	$0.3483^{+0.3442}_{-0.248}$	$0.2998^{+0.3779}_{-0.2219}$
δ_e	$0.0041^{+0.0002}_{-0.0002}$	$0.0043^{+0.0002}_{-0.0002}$	$0.004^{+0.0002}_{-0.0002}$	$0.0041^{+0.0002}_{-0.0002}$	$0.0038^{+0.0002}_{-0.0003}$	$0.004^{+0.0002}_{-0.0003}$
A	$0.2966^{+0.0676}_{-0.0745}$	$0.3543^{+0.0495}_{-0.0817}$	$0.3744^{+0.0413}_{-0.0715}$	$0.3682^{+0.0466}_{-0.0846}$	$-0.2809^{+0.1462}_{-0.1489}$	$0.2414^{+0.1175}_{-0.1459}$
B	$0.1721^{+0.0424}_{-0.0468}$	$0.118^{+0.0416}_{-0.0457}$	$0.0685^{+0.0506}_{-0.0539}$	$0.0779^{+0.051}_{-0.0562}$	$-0.0097^{+0.0731}_{-0.0746}$	$-0.1545^{+0.0829}_{-0.0866}$
S_1	$-0.0028^{+0.0008}_{-0.001}$	$-0.003^{+0.0006}_{-0.0009}$	$-0.0043^{+0.0007}_{-0.0008}$	$-0.0044^{+0.0008}_{-0.0009}$	$-0.2809^{+0.1462}_{-0.1489}$	$-0.0103^{+0.0016}_{-0.0017}$
S_2	$0.1947^{+0.1199}_{-0.0779}$	$0.4273^{+0.1414}_{-0.1493}$	$0.4732^{+0.0856}_{-0.1018}$	$0.4775^{+0.0856}_{-0.1155}$	$-0.0097^{+0.0731}_{-0.0746}$	$0.4637^{+0.0807}_{-0.0806}$
σ_F	$0.001467^{+2.9e-05}_{-2.8e-05}$	$0.001454^{+2.9e-05}_{-2.9e-05}$	$0.001436^{+2.7e-05}_{-2.7e-05}$	$0.001438^{+2.8e-05}_{-2.8e-05}$	$0.002^{+0.0}_{-0.0}$	$0.0015^{+0.0}_{-0.0}$
$\log(L)$	7765.1	7780.55	7798.97	7799.72	7331.22	7728.31
E	7693.49	7694.62	7695.14	7674.41	7248.87	--
$\log(L)$ Unbinned	340661.32	340980.0	341190.60	341021.73	316405.51	338845.64
E Unbinned	340548.18	340844.23	341026.55	340823.74	316275.61	--
A_p	$0.0028^{+0.0007}_{-0.0006}$	$0.0033^{+0.0008}_{-0.0004}$	$0.0031^{+0.0006}_{-0.0004}$	$0.0031^{+0.0007}_{-0.0004}$	$0.0021^{+0.0001}_{-0.0012}$	$0.0024^{+0.0006}_{-0.0006}$
Φ_p	$0.5315^{+0.1006}_{-0.1006}$	$0.3365^{+0.1132}_{-0.1006}$	$0.1855^{+0.1447}_{-0.1258}$	$0.217^{+0.1509}_{-0.1321}$	$-2.7768^{+0.2704}_{-5.7674}$	$-0.5629^{+0.5157}_{-0.3271}$

Table 3.4: Fit parameters using a first order Fourier series to model the phase variation with stellar variation for different detector models. Most probable astrophysical parameters estimates obtained from posterior probability distribution from the MCMC routine using various systematics models. The planetary brightness phase variation is modeled as a first order Fourier series and the model includes stellar variability. The highlighted fits yield the greatest Bayesian Evidences. We note that the fit presented in the two last columns are inconsistent with a westward offset but their $\log(L)$ are significantly lower than the $\log(L)$ of Poly2 presented in Supplementary Table 3. The largest value of $\log L$ and E for both binned and unbinned data are in bold blue. The errors on the parameters are the 68% confidence region bounds of the posterior distribution obtained from `emcee`.

CHAPTER 3. THERMAL PHASE CURVE OF COROT-2B

Parameter	Poly2	Poly3	Poly4	Poly5	PLD1	BLISS
t_0	1.0744 ^{+0.0002} _{-0.0002}	1.0744 ^{+0.0002} _{-0.0002}	1.0745 ^{+0.0002} _{-0.0002}	1.0745 ^{+0.0002} _{-0.0002}	1.0747 ^{+0.0002} _{-0.0002}	1.0745 ^{+0.0002} _{-0.0002}
R_p/R_*	0.1695 ^{+0.0009} _{-0.001}	0.1689 ^{+0.0009} _{-0.001}	0.1686 ^{+0.0009} _{-0.001}	0.1686 ^{+0.001} _{-0.001}	0.1699 ^{+0.0012} _{-0.0012}	0.1681 ^{+0.001} _{-0.001}
a/R_*	6.6803 ^{+0.0228} _{-0.0239}	6.6785 ^{+0.0245} _{-0.0238}	6.686 ^{+0.0237} _{-0.024}	6.6849 ^{+0.0234} _{-0.0224}	6.6888 ^{+0.0246} _{-0.0251}	6.6823 ^{+0.0245} _{-0.025}
i	87.8756 ^{+0.0888} _{-0.0886}	87.8709 ^{+0.0911} _{-0.0896}	87.8662 ^{+0.0937} _{-0.0926}	87.8592 ^{+0.0968} _{-0.0943}	87.8581 ^{+0.0923} _{-0.0909}	87.8693 ^{+0.0954} _{-0.0927}
$e \cos \omega$	0.0 ^{+0.0004} _{-0.0004}	-0.0 ^{+0.0004} _{-0.0004}	-0.0 ^{+0.0005} _{-0.0005}	-0.0 ^{+0.0004} _{-0.0004}	0.0 ^{+0.0003} _{-0.0003}	-0.0 ^{+0.0006} _{-0.0006}
$e \sin \omega$	0.0 ^{+0.0004} _{-0.0004}	-0.0 ^{+0.0004} _{-0.0004}	-0.0 ^{+0.0005} _{-0.0005}	-0.0 ^{+0.0005} _{-0.0005}	0.0 ^{+0.0003} _{-0.0003}	0.0 ^{+0.0006} _{-0.0006}
q_1	0.0126 ^{+0.019} _{-0.0084}	0.0142 ^{+0.0205} _{-0.0095}	0.0147 ^{+0.0202} _{-0.0097}	0.0139 ^{+0.0198} _{-0.0093}	0.0206 ^{+0.0263} _{-0.0132}	0.0164 ^{+0.0225} _{-0.0106}
q_2	0.2912 ^{+0.3934} _{-0.2163}	0.2931 ^{+0.3882} _{-0.2177}	0.2969 ^{+0.3635} _{-0.2218}	0.2899 ^{+0.3927} _{-0.2192}	0.3475 ^{+0.3813} _{-0.2509}	0.2986 ^{+0.3773} _{-0.2215}
δ_e	0.0042 ^{+0.0002} _{-0.0002}	0.0044 ^{+0.0002} _{-0.0002}	0.0041 ^{+0.0002} _{-0.0002}	0.0042 ^{+0.0002} _{-0.0002}	0.0045 ^{+0.0002} _{-0.0002}	0.004 ^{+0.0003} _{-0.0003}
A	0.3662 ^{+0.0423} _{-0.0554}	0.3879 ^{+0.0422} _{-0.0615}	0.3294 ^{+0.0619} _{-0.0837}	0.3565 ^{+0.0605} _{-0.0793}	0.0209 ^{+0.0307} _{-0.0154}	0.2474 ^{+0.0925} _{-0.1138}
B	0.1452 ^{+0.0427} _{-0.0435}	0.1058 ^{+0.0441} _{-0.0431}	0.0047 ^{+0.0571} _{-0.0571}	0.0238 ^{+0.0601} _{-0.0608}	0.0151 ^{+0.0265} _{-0.0203}	-0.1335 ^{+0.0822} _{-0.086}
C	0.0624 ^{+0.0258} _{-0.0292}	0.0618 ^{+0.0324} _{-0.0351}	0.0955 ^{+0.0342} _{-0.04}	0.092 ^{+0.0318} _{-0.0366}	0.1955 ^{+0.0165} _{-0.0195}	0.064 ^{+0.0379} _{-0.0446}
D	0.0795 ^{+0.0233} _{-0.0247}	0.044 ^{+0.0236} _{-0.0253}	-0.0084 ^{+0.0367} _{-0.0384}	0.0022 ^{+0.0332} _{-0.0377}	0.143 ^{+0.029} _{-0.0289}	0.0359 ^{+0.0422} _{-0.0425}
S_1	-0.0018 ^{+0.0006} _{-0.0008}	-0.0019 ^{+0.0006} _{-0.0008}	-0.0038 ^{+0.0008} _{-0.0009}	-0.0037 ^{+0.0008} _{-0.0009}	-0.0045 ^{+0.0004} _{-0.0004}	-0.0089 ^{+0.0017} _{-0.0018}
S_2	0.137 ^{+0.1387} _{-0.1027}	0.4255 ^{+0.2129} _{-0.1939}	0.3925 ^{+0.1183} _{-0.12}	0.4565 ^{+0.1249} _{-0.1388}	-0.3939 ^{+0.085} _{-0.0901}	0.4327 ^{+0.0806} _{-0.0777}
σ_F	0.00146 ^{+3e-05} _{-2.9e-05}	0.00145 ^{+2.8e-05} _{-2.8e-05}	0.001434 ^{+2.9e-05} _{-2.8e-05}	0.001435 ^{+2.9e-05} _{-2.8e-05}	0.001961 ^{+4e-05} _{-3.8e-05}	0.001516 ^{+3.1e-05} _{-2.9e-05}
$\log(L)$	7772.29	7782.91	7800.13	7801.06	7383.08	7728.82
E	7693.52	7689.82	7689.13	7668.59	7293.57	--
$\log(L)$ Unbinned	340908.31	304922.02	341265.45	341080.61	318363.35	338882.05
E Unbinned	340783.86	304774.93	341090.08	340871.3	318222.15	--
A_p	0.0034 ^{+0.0004} _{-0.0004}	0.0036 ^{+0.0005} _{-0.0004}	0.0027 ^{+0.0006} _{-0.0004}	0.0031 ^{+0.0005} _{-0.0005}	0.0024 ^{+0.0002} _{-0.0004}	0.0027 ^{+0.0005} _{-0.0005}
Φ_p	0.4245 ^{+0.0943} _{-0.1006}	0.2925 ^{+0.1132} _{-0.1195}	-0.022 ^{+0.1824} _{-0.1761}	0.0409 ^{+0.1698} _{-0.1635}	0.3176 ^{+0.0755} _{-0.0755}	-0.1415 ^{+0.4088} _{-0.2704}

Table 3.5: Fit parameters using a second order Fourier series to model the phase variation with stellar variation for different detector models. Most probable astrophysical parameters estimates obtained from posterior probability distribution from the MCMC routine using various systematics models. The planetary brightness phase variation is modeled as a second order Fourier series and the model includes stellar variability. The highlighted fits yield the greatest Bayesian Evidences. The highlighted fits yield the greatest Bayesian Evidences. The largest value of $\log L$ and E for both binned and unbinned data are in bold blue. The errors on the parameters are the 68% confidence region bounds of the posterior distribution obtained from `emcee`. We note that the fit presented in last column shows an eastward offset but the $\log(L)$ is significantly lower than the $\log(L)$ of Poly2 presented in Supplementary Table 3. Despite having a high $\log(L)$, Poly 4 and Poly 5, which are consistent with a null planetary offset, have a $\Delta E > 6$ (or $\Delta \text{BIC} > 12$) when compared to the fit with highest E . Therefore, these fits are significantly worse than Poly2 presented in Supplementary Table 3 ?

Parameter	Scheme 1	Scheme 2	Scheme 3	Scheme 4
t_0	$1.0745^{+0.0002}_{-0.0002}$	$1.0744^{+0.0002}_{-0.0002}$	$1.0742^{+0.0002}_{-0.0002}$	$1.0744^{+0.0002}_{-0.0002}$
R_p/R_*	$0.1672^{+0.0012}_{-0.0012}$	$0.1697^{+0.0009}_{-0.0009}$	$0.1709^{+0.0009}_{-0.001}$	$0.1717^{+0.001}_{-0.001}$
a/R_*	$6.7048^{+0.0254}_{-0.0264}$	$6.6818^{+0.0228}_{-0.0229}$	$6.6732^{+0.0241}_{-0.0244}$	$6.67^{+0.0248}_{-0.0243}$
i	$87.8299^{+0.094}_{-0.0962}$	$87.8771^{+0.0895}_{-0.092}$	$87.8992^{+0.0906}_{-0.0947}$	$87.8904^{+0.0943}_{-0.0882}$
$e \cos \omega$	$-0.0^{+0.0003}_{-0.0003}$	$0.0^{+0.0004}_{-0.0004}$	$-0.0^{+0.0005}_{-0.0005}$	$0.0^{+0.0004}_{-0.0004}$
$e \sin \omega$	$0.0^{+0.0003}_{-0.0003}$	$0.0^{+0.0004}_{-0.0004}$	$-0.0^{+0.0005}_{-0.0005}$	$-0.0^{+0.0004}_{-0.0004}$
q_1	$0.0218^{+0.0305}_{-0.0145}$	$0.0118^{+0.0174}_{-0.0079}$	$0.0085^{+0.0125}_{-0.0059}$	$0.0125^{+0.017}_{-0.0082}$
q_2	$0.3157^{+0.3819}_{-0.2321}$	$0.3198^{+0.3903}_{-0.2364}$	$0.4278^{+0.3581}_{-0.302}$	$0.4092^{+0.368}_{-0.2808}$
δ_e	$0.0043^{+0.0002}_{-0.0002}$	$0.0044^{+0.0002}_{-0.0002}$	$0.0047^{+0.0002}_{-0.0002}$	$0.0047^{+0.0002}_{-0.0002}$
A	$0.4^{+0.0196}_{-0.0216}$	$0.445^{+0.0134}_{-0.0155}$	$0.4633^{+0.0084}_{-0.0113}$	$0.4424^{+0.0125}_{-0.0129}$
B	$0.1684^{+0.0364}_{-0.0346}$	$0.1966^{+0.0329}_{-0.0326}$	$0.1758^{+0.0318}_{-0.0316}$	$0.2345^{+0.0348}_{-0.0349}$
C	$0.0936^{+0.0143}_{-0.0149}$	$0.066^{+0.0136}_{-0.0129}$	$0.0627^{+0.0111}_{-0.0115}$	$0.0243^{+0.0153}_{-0.0153}$
D	$0.0782^{+0.0128}_{-0.0132}$	$0.0686^{+0.0118}_{-0.0118}$	$0.0554^{+0.0108}_{-0.0101}$	$0.07^{+0.0139}_{-0.0142}$
σ_F	$0.002^{+0.0}_{-0.0}$	$0.0015^{+0.0}_{-0.0}$	$0.0017^{+0.0}_{-0.0}$	$0.0018^{+0.0}_{-0.0}$
$\log(L)$	7352.42	7767.37	7566.86	7519.72
E	7280.82	7695.76	7495.25	7448.11
$\log(L)$ Unbinned	283683.77	340759.43	309315.81	297155.75
E Unbinned	283570.62	340646.28	309428.95	297268.89
A_p	$0.0043^{+0.0002}_{-0.0002}$	$0.0046^{+0.0003}_{-0.0003}$	$0.0047^{+0.0002}_{-0.0002}$	$0.0047^{+0.0002}_{-0.0002}$
Φ_p	$0.412^{+0.0629}_{-0.0566}$	$0.3994^{+0.0692}_{-0.0692}$	$0.3616^{+0.0566}_{-0.0629}$	$0.4874^{+0.0629}_{-0.0629}$

Table 3.6: Fit parameters using a second order Fourier series to model the phase variation without stellar variation for different photometric extraction schemes. Most probable astrophysical parameters estimates obtained from posterior probability distribution from the MCMC routine using various photometric schemes (See Photometry Extraction in Methods). The planetary brightness phase variation is modeled as a second order Fourier series and the detector model is second order polynomial. The highlighted fits yield the greatest Bayesian Evidences. The largest value of $\log L$ and E for both binned and unbinned data are in bold blue. The errors on the parameters are the 68% confidence region bounds of the posterior distribution obtained from `emcee`.

3.4 Supplementary Figures

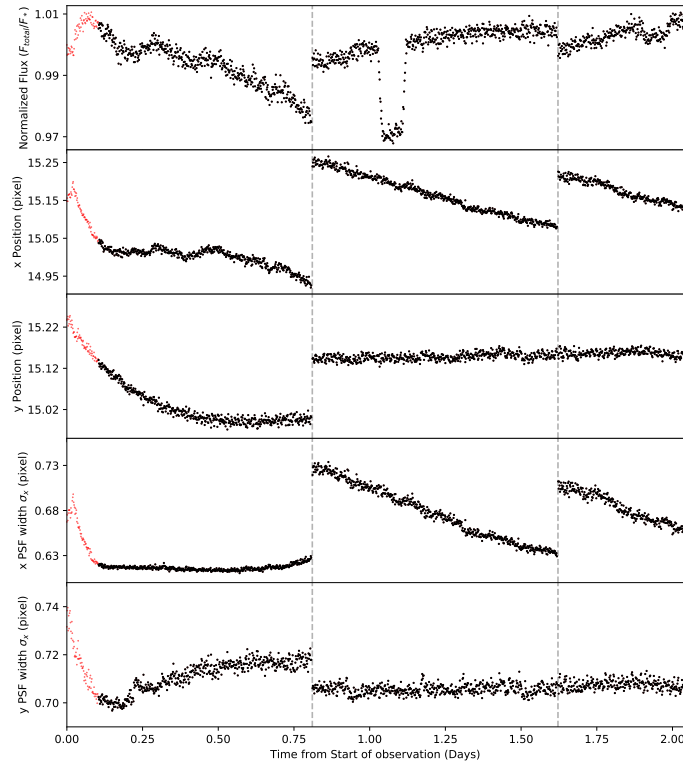


Figure 3.6: Raw normalized photometry and PSF diagnostics. *Spitzer* 4.5 μm photometry and PSF diagnostics after median binning by data cube excluding the discarded AORs. The vertical gray dashed lines denotes the start and end of the different AORs. The red dots represent the data excluded from our analysis due to the rapid change in telescope pointing.

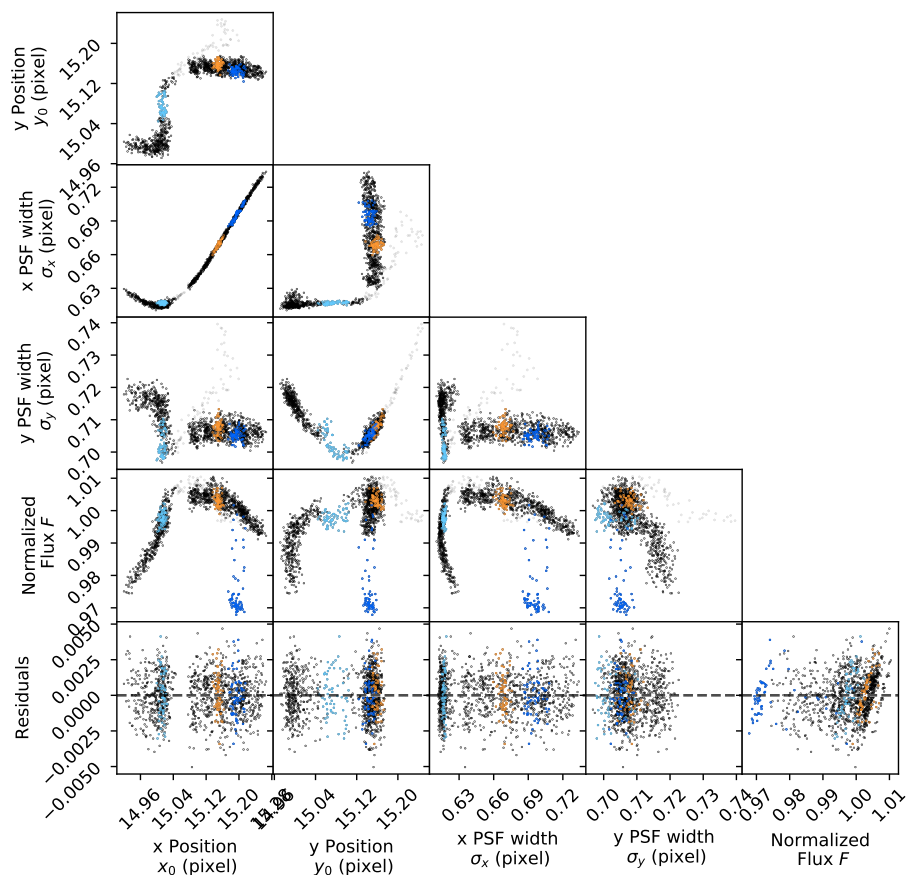


Figure 3.7: PSF diagnostics for our observations of CoRoT-2b. Each point represent the median of a data cube. The light and dark blue dots denote the first and second secondary eclipse, respectively. The orange dots represent the transit and the gray dots are the data cubes at the start of the observations that were discarded from our analysis.

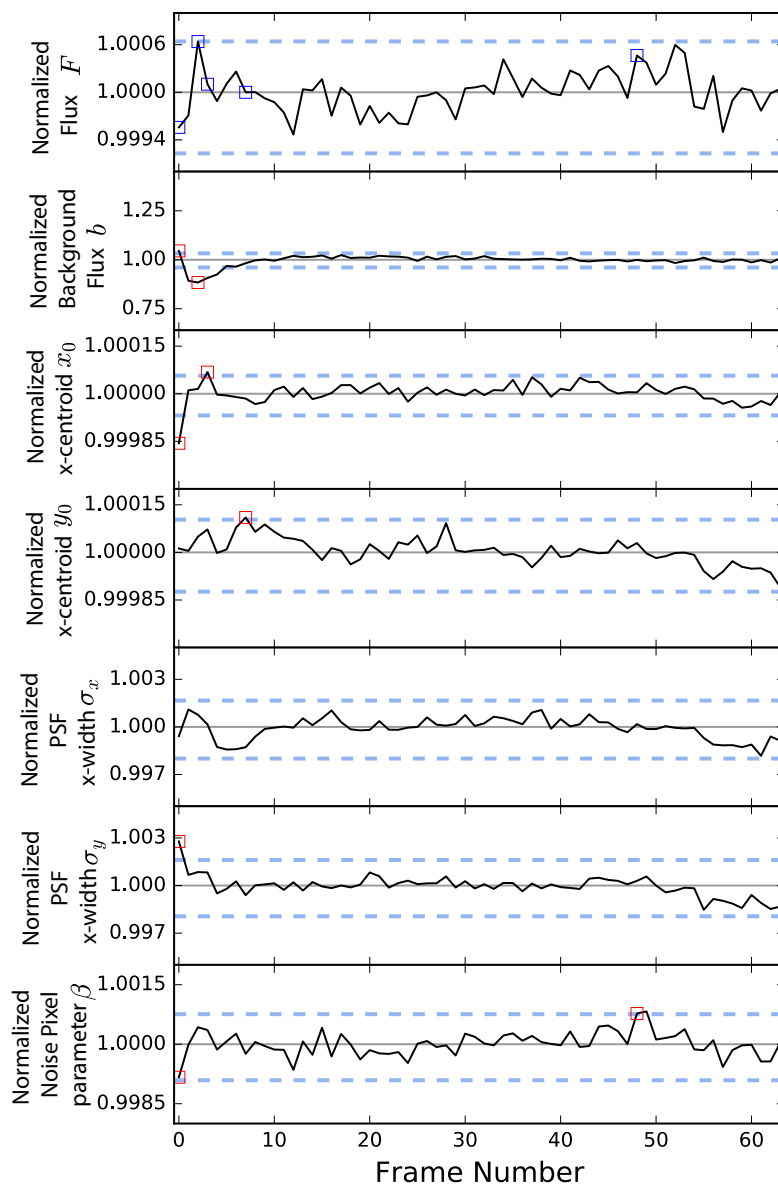


Figure 3.8: Systematic changes in photometry within a 64-frame data cube. All the values presented in this figure are normalized to their respective data cube median. The top panel shows the background-subtracted photometry using a 2.5 pixel radius hard circular aperture centered on the pixel (15, 15). The second panel shows systematic changes in the background flux and the panels below are the systematic changes in the PSF diagnostics. The last panel shows the systematic changes in the noise pixel parameter. The gray lines represent the mean parameter values and the blue dashed lines are the 3σ boundaries. The blue squares highlight to unusual frames with usable photometry despite their unusual PSF metrics identified with red squares.

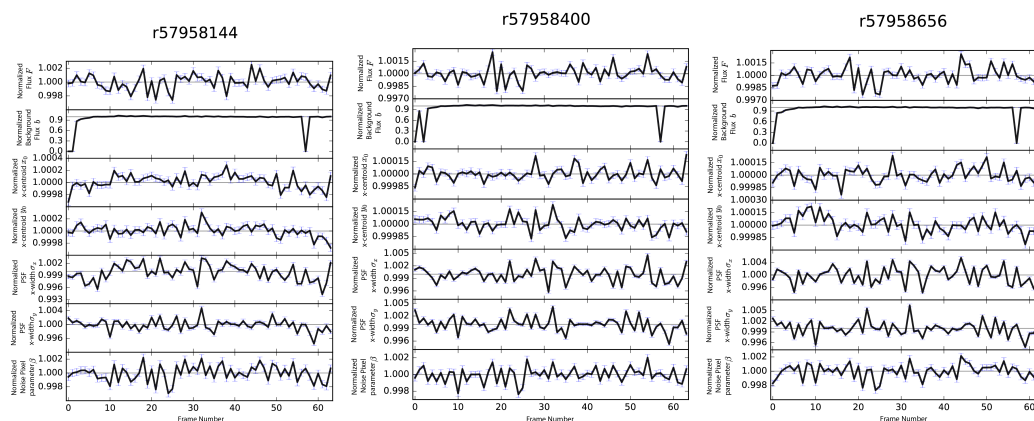


Figure 3.9: Frame diagnostics for AORs r57958144, r57958400, and r57958656 respectively. The background subtracted flux exhibit a repeating zigzag pattern between the 18th and 26th frames. This effect was introduced at the Sky Dark subtraction stage, the only frame-dependent process that affects IRAC data. We used an image stack provided by the IRAC team to remove this effect and also correct for the known low 58th frame background level error. Note that the first few frames will still have low backgrounds, which is due to the *first frame effect* that impacts every IRAC observation and depends on the delay time since last exposure. This was not corrected by the image stack, but since it does not affect our photometry significantly, we chose to keep the first frame photometry.

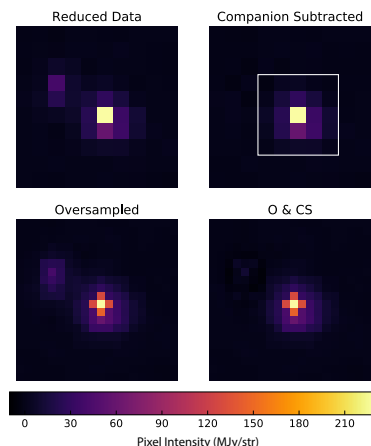


Figure 3.10: Modified images for different photometric schemes. *Top Left:* Background-subtracted image of CoRoT-2b and its visual companion, 2MASS J19270636+0122577, on the left. *Top Right:* Same image after the subtraction of the companion. The white rectangle encapsulates the pixels used to estimate the centroid and widths of the PSF. *Bottom Left:* Oversampled image of the background subtracted image (top-left). *Bottom Right:* Same image (bottom left) after the subtraction of the PSF of the companion.

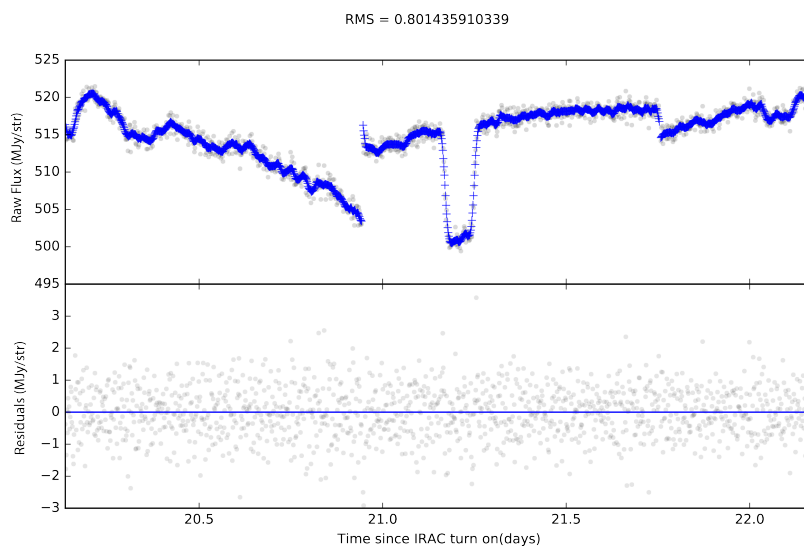


Figure 3.11: Root mean square calculation example. In the top panel, the grey points are raw data and the blue light curve is the smoothed lightcurve obtained by boxcar averaging with a length of 50 using the `astropy.convolution` module in Python. The lower panel show the difference between the raw and smoothed lightcurve used to estimate the RMS scatter.

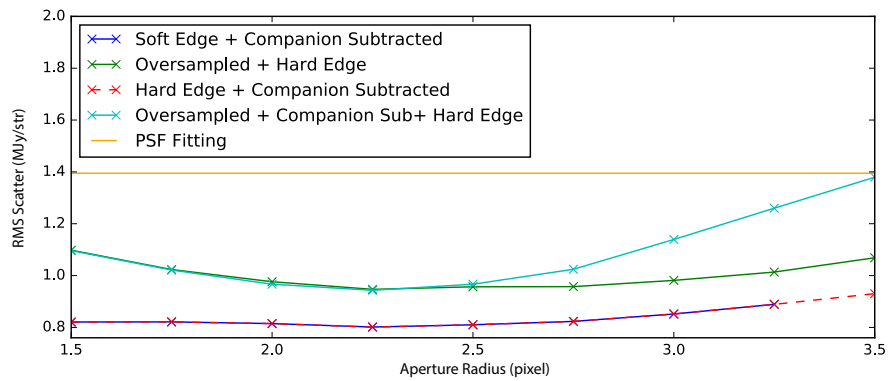


Figure 3.12: RMS scatter for different photometric schemes. In all cases, an aperture with a radius of $r = 2.25$ is optimal as it minimizes the RMS scattering. The non-oversampled, soft-edge and companion subtracted photometric scheme yield the smallest RMS scatter. Note that the RMS scatter for PSF fitting is constant since there is no aperture involved.

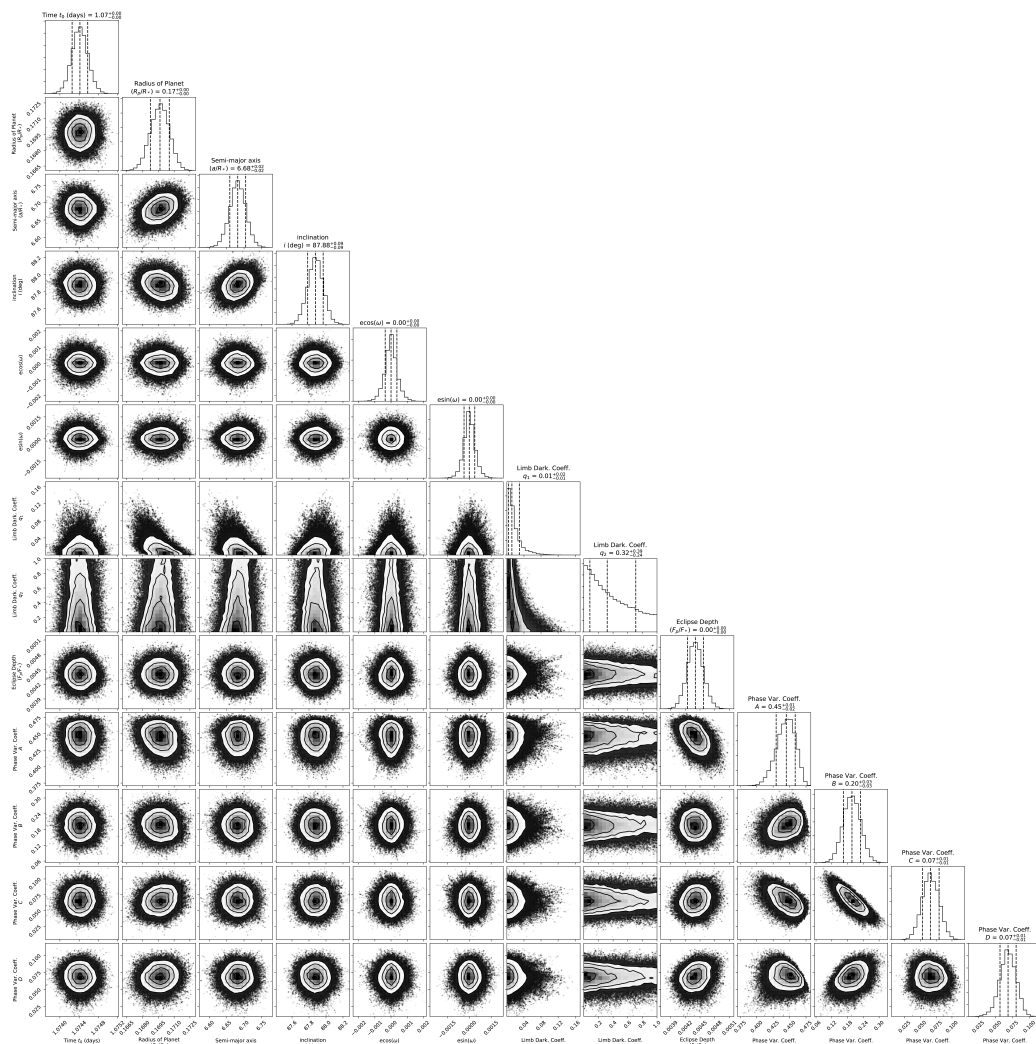


Figure 3.13: Corner plot of the fit parameters’ posterior distribution. Pairs plot showing the posterior distribution of the astrophysical fitting parameters from MCMC. The panels on the diagonal show the marginalized posterior distribution for each fitting parameter. The 68% credible confidence region is marked by vertical dashed lines and quantified above the panel. The off-diagonal panels show the two-dimensional marginalized distribution for pairs of parameters, with the gray shading corresponding to the probability density and black contours indicating the 68%, 95%, and 98% confidence regions. The outer black points are individual MCMC walkers positions outside of the 98% confidence region. This plot is made using the `corner` Python package.

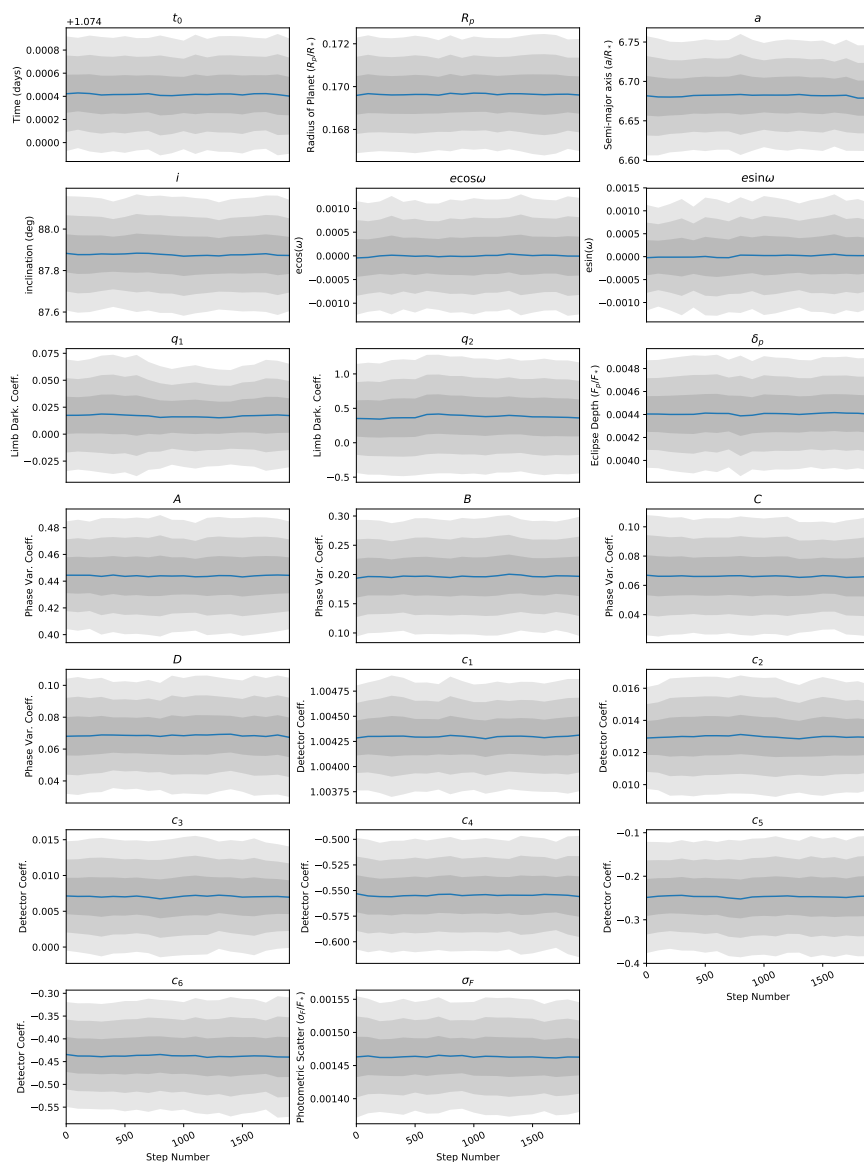


Figure 3.14: Distribution of walkers positions for the last 2000 steps of the MCMC for our best fit model. The blue line denoted the best-fit parameter value at each step and the gray areas are the 68%, 95% and 98% confidence regions obtained from the distribution of the walkers at each step.

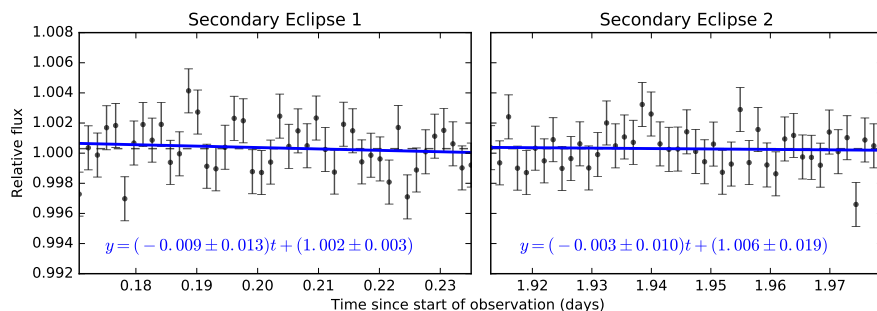


Figure 3.15: In-eclipse diagnostics for the model with the greatest E . The left and right panels show the first and second in-eclipse portions of the lightcurve respectively. The black points are the photometry after the removal of detector systematics (see Table 3.3; Poly 2). We fit a linear function to the in-eclipse portion and find that the fit is consistent within 1σ with the absence of trend. The error bars are the photometric scatter estimated with a Markov Chain Monte Carlo (MCMC) in the fitting routine.

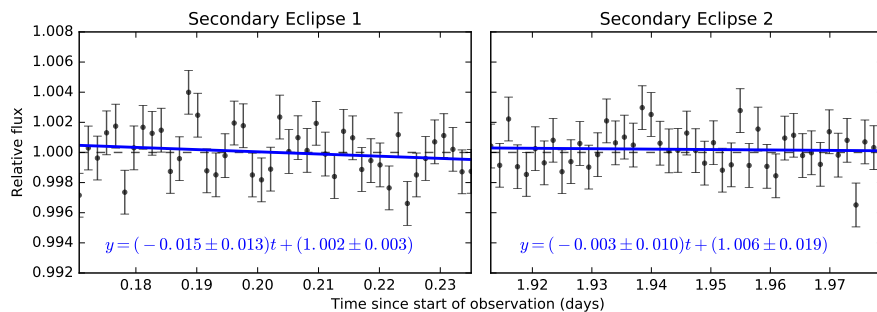


Figure 3.16: In-eclipse diagnostics for the model with the second greatest E . The left and right panels show the first and second in-eclipse portions of the lightcurve respectively. The black points are the photometry after the removal of detector systematics and stellar variability (see Table 3.4; Poly3). We fit a linear function to the in-eclipse portion. We find that the fit for the second eclipse is consistent within 1σ with the absence of trend, but the first in-eclipse portion exhibit a trend with a slope of -0.015 ± 0.013 . The error bars are the photometric scatter estimated with a Markov Chain Monte Carlo (MCMC) in the fitting routine.

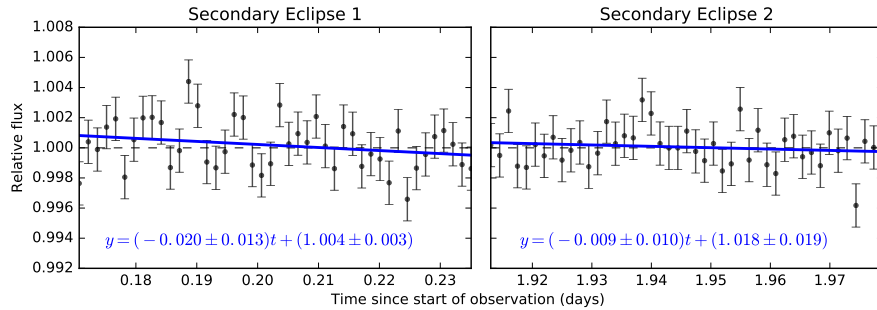


Figure 3.17: In-eclipse diagnostics for the model with the third greatest E . The left and right panels show the first and second in-eclipse portions of the lightcurve respectively. The black points are the photometry after the removal of detector systematics and stellar variability (see Table 3.4; Poly4). We fit a linear function to the in-eclipse portion. We find that the fit for the second eclipse is consistent within 1σ with the absence of trend, but the first in-eclipse portion exhibit a trend with a slope of -0.020 ± 0.013 . The error bars are the photometric scatter estimated with a Markov Chain Monte Carlo (MCMC) in the fitting routine.

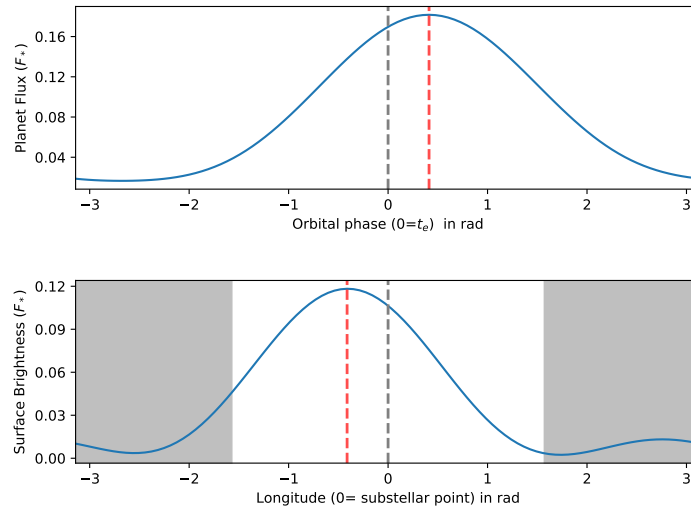


Figure 3.18: 1D brightness map of CoRoT-2b from inverting the orbital phase function. *Top panel:* The brightness variation of the planet as a function of orbital phase. The gray dashed line denote the orbital phase of secondary eclipse and the red dashed line denoted the orbital phase of the peak of the phase variation which is 0.41 ± 0.06 rad after the secondary eclipse. *Bottom panel* The surface brightness of CoRoT-2b as a function of longitude shown in the bottom panel Cowan & Agol (2008). The gray dashed line denotes the substellar meridian of the planet and the red dashed line denotes the brightest longitude on the planet located west of the substellar meridian. The gray shaded area represents the night hemisphere of the planet.

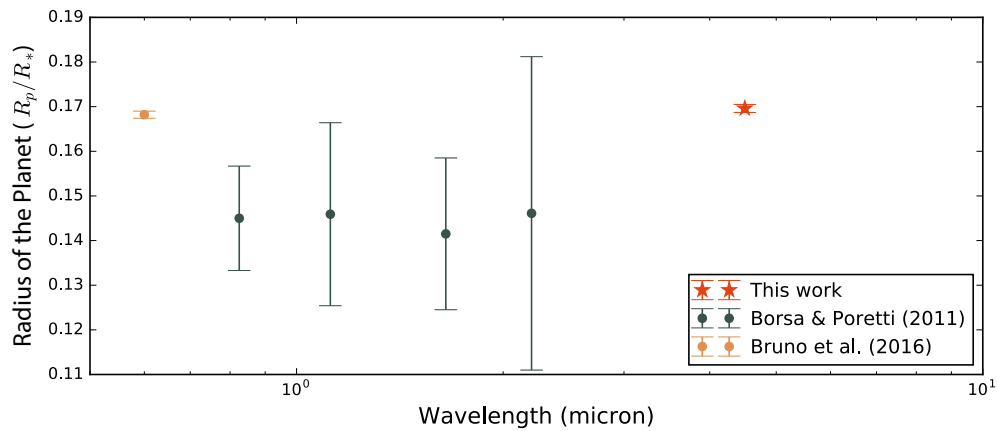


Figure 3.19: Transmission spectrum of CoRoT-2b. Our transit depth measurement and error estimates obtained with a Markov Chain Monte Carlo (MCMC) is shown along with ground-based measurements and their respective uncertainties [Borsa & Poretti \(2011\)](#) and the re-analysis of the *CoRoT* observations [Bruno et al. \(2016\)](#). Given the large errors on the ground-based measurements and the sparsity of the measurements, we did not attempt to fit the transmission spectrum. Observations from future space mission such as JWST would be required to obtain a meaningful transmission spectrum.

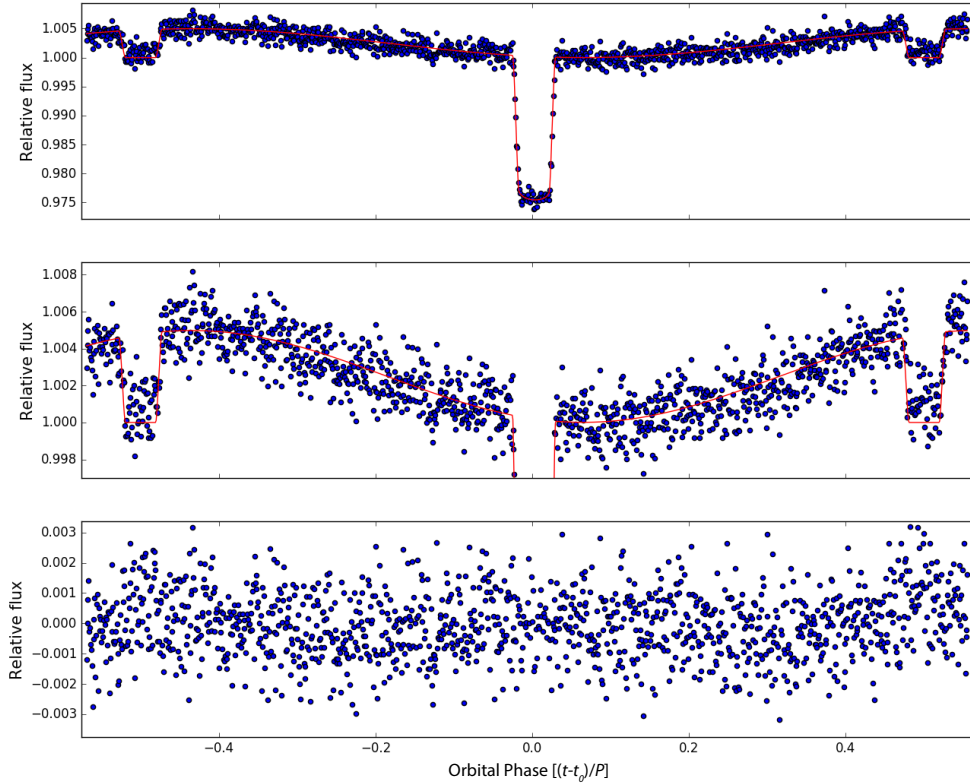


Figure 3.20: Fit using an independent photometry and fitting pipeline ?. The top panel show the astrophysical fit (line) and the data after the removal of the systematics (dots). The second panel is a zoomed-in version of the first panel to better see the planetary phase variation. The bottom panel shows the residuals between the corrected data and the astrophysical fit. Using an independent fitting pipeline, the result shows a westward offset of 25.6 ± 1.9 degrees, which is consistent with the result obtained using the method described in this paper.

3.5 Supplementary Information

3.5.1 Data Reduction

For our analysis, we use basic calibrated data which are corrected (dark subtracted, flat-fielded, linearized and flux calibrated) using the S19.2.0 IRAC pipeline. After the data cube diagnostics described in Supplementary Information, we find a frame respective flux modulation introduced by inaccurate dark subtraction. We then correct for the flux modulation using an image stack provided by the IRAC team, which also fixes the known 58th frame error in *Spitzer* sub-array data (Deming et al. 2011).

We convert the pixel intensity from MJy/str to electron counts by multiplying the pixel values by $\text{GAIN} \times \text{EXPTIME}/\text{FLUXCONV}$. We use the parameter values AINTBEG and ATIMEEND to obtain the middle of each exposure assuming uniform temporal spacing between each frame. We mask the pixels with *NaN* values which are a result of energetic particle hits or pixel defects. Masking is preferred over replacing them with average values to minimize the correction and manipulation of the data.

We perform pixel-level sigma clipping by comparing each pixel with the median of the same pixel of all the frames in its respective data cube and masking 4σ outliers. Frames containing a sigma-clipped pixel located in a 5×5 pixel box centered on the central pixel of the target are discarded entirely. A total of 191 images were tossed out, representing 0.22% of the total data.

We perform frame-by-frame background subtraction where sky background level is estimated as the median pixel value of the frame excluding a 7×7 pixel box centered on the pixel (15, 15) containing both the target and the companion. Additionally, the retained data exhibit a 2.5 hours ramp-like behaviour at the beginning with rapidly changing PSF metrics. This effect may be related to the settling of the telescope at a new pointing (Knutson et al. 2012). Experimenting with and without removing the ramp-like behaviour, we find that it is difficult to constrain the detector model during the 2.5 hours as the the PSF properties are notably different from the rest of the data, as described below. Since trimming is standard practice for *Spitzer* phase curves (Knutson et al. 2012; Wong et al. 2015), we elect to discard the first 2.5 hours of data. After data removal, the remaining data we use for our analysis contains 1288 data cubes.

3.5.2 Photometry Extraction

Observations of CoRoT-2 ($K = 10.31$) (Cabrera et al. 2009) show the presence of a close-in visual companion, 2MASS J19270636+0122577 ($K = 12.03$) (Cutri et al. 2003). Due to the proximity of the companion, naively performing aperture photometry could lead to inaccurate estimation of the transit and secondary eclipse depths. We experiment with different strategies to retrieve our target’s flux while reducing the contamination from the second source.

First, we fit for both sources simultaneously using two 2D Gaussians for each frame and retrieve the photometry from the fit. The second strategy is to fit for both sources, then subtract the fit for the companion from each frame and perform aperture photometry on the companion-subtracted image. The third strategy is to oversample the images by a factor of 2 and use aperture photometry. The fourth scheme combines the second and third strategy: we fit for both sources simultaneously using the oversampled images and then subtract the fit for the companion and use aperture photometry.

To retrieve the target’s flux, we experiment with various apertures: hard-edged and soft-edged circular apertures of various radii. While the PSF metrics vary from one frame to another, we chose to keep the position of the aperture fixed. As the centroids only moves over a tenth of the area of a pixel throughout the observation, an aperture of radius 2-3 pixels is large enough to collect all the flux despite the changes in centroid. In principle, an aperture varying in shape and size should improve the photometry, but in practice, we find that a fixed aperture performs better. This suggests that the uncertainties on measurements of the PSF’s position and shape for each frame introduce noise into the time-varying aperture photometry.

To determine the best photometric schemes, we calculate the root-mean-squared (RMS) scatter for each light curve as shown in Supplementary Fig. 3.12 and choose the one exhibiting the smallest RMS scatter. In general, we find that the light curves obtained from PSF fitting and aperture photometry on oversampled images exhibit larger RMS scatter. Ultimately, we use photometry on non-oversampled images using a soft-edged circular aperture with a radius of 2.25 pixel after the subtraction of the PSF of the companion as it yields the smallest RMS scatter.

Moreover, the residual flux from the companion subtraction is less than 0.05% of the target flux, which does not significantly impact centroid measurements. We estimate the residual flux by placing a circular aperture ($r = 2.25$ pixels) at a symmetric location on the other side of CoRoT-2’s companion on the companion-subtracted images. Therefore, the counts in this aperture are the residuals from companion

subtraction.

3.5.3 Centroids

Due to drift and jitter of the telescope pointing, the position of the target point spread function (PSF) on the detector varies with time. After the frame by frame removal of the companion, we determine the centroid (x_0, y_0) of CoRoT-2 in each frame by calculating the flux-weighted mean of a 5×5 box centered on the brightest pixel located at (15, 15):

$$x_0 = \frac{\sum_i F_i x_i}{\sum_i F_i}, \quad (\text{S1})$$

$$y_0 = \frac{\sum_i F_i y_i}{\sum_i F_i}. \quad (\text{S2})$$

The shape of the PSF also changes from one frame to another. We first calculate the target's noise pixel parameter, $\tilde{\beta}$ (Mighell 2005):

$$\tilde{\beta} = \frac{(\sum_i I_i)^2}{\sum_i I_i^2}. \quad (\text{S3})$$

The noise pixel parameter is commonly used as an estimate of the PSF width assuming an isotropic PSF. We instead opt to estimate the x and y extent of the point spread function of the target separately by computing the standard deviation along each direction for each frame:

$$\sigma_x = \sqrt{\frac{\sum_i F_i (x_i - x_0)^2}{\sum_i F_i}}, \quad (\text{S4})$$

$$\sigma_y = \sqrt{\frac{\sum_i F_i (y_i - y_0)^2}{\sum_i F_i}}. \quad (\text{S5})$$

As shown in Figure 3.7, the size of the PSF shape is a non-monotonic function of the centroid position on the pixel. As previously mentioned, the data collected during the first 2.5 hours of the observation exhibit a ramp-like behavior which coincide with a brief change in the position and shape of the PSF (Lanotte et al. 2014).

3.5.4 Noise in *Spitzer* IRAC Data due to Bias Dark Subtraction

Unlike cryogenic *Spitzer* data, the *Warm Spitzer* sub-array data exhibit a frame dependent background flux systematics (Deming et al. 2011). Such known systematics include the *58th frame error* and the *first frame effect*. The *58th frame error* is due to a problem in the skydark subtraction stage which leaves the background level in that frame different from the rest. On the other hand, the first few frames have low backgrounds, due the "first frame effect" which impacts every IRAC observation and depends on the delay time since last exposure. In principle, the background-subtracted flux of the target should be immune to such variations, but this has not been borne out in practice, leading researchers to remove certain frames from their analysis (Deming et al. 2011).

Once we obtained the sky background level, centroid position, and PSF shape for each frame, we perform aperture photometry on the background and companion subtracted images for each frame using a soft-edged 2.25 pixel radius circular aperture. We normalize each value to its respective data cube median. We then find the median value for each frame number presented in Figure 3.8. While performing this analysis, we notice that the background subtracted flux exhibits a repeating zigzag pattern between the *18th* and *26th* from one AOR to the other as shown in Figure 3.9. This modulation was introduced at the Sky Dark subtraction stage of the S19.2.0 IRAC pipeline, the only frame-dependent process that affect IRAC data. Indeed, when we perform aperture photometry on the central pixels of the dark calibration cube, we see the same zigzag pattern in reverse. The IRAC team provided us with an image stack to remove this effect which also fixed the *58th frame error*. After the correction, our analysis shows no significant flux variation, therefore all frames within a data cube provide usable photometry.

3.5.5 Binning

Although the recalibration cube provided by the IRAC team corrected the obvious frame dependent systematics (see Supplementary Information), subarray data are still subject to effects such as the *first frame effect*, which in principle should not affect the photometry. Nonetheless, we choose to play it safe and elect to median bin the data by datacube. Given our 2 seconds exposures, the binned data have a temporal resolution of 128 seconds. Since the duration of ingress and egress of the system is over 1400 seconds, such resolution is still short enough to resolve the shape of occultations.

Binning data before fitting a model has many advantages (Deming et al. 2015). First, binning data filters out high frequency noise, including the datacube systematics. Secondly, it increases the accuracy of our measurement of the PSF metrics. Our instrumental models are a function of PSF metrics, hence more accurate measurements improve our ability to decorrelate the detector systematics from the astrophysical signal. Finally, reducing the number of data points ultimately makes model fitting significantly faster.

3.5.6 Upper Limit on Stellar Variability at 4.5 μm

The Spitzer Space Telescope is on a heliocentric Earth-trailing orbit and is drifting away from Earth at about 0.1 AU per year. Consequently, at the time of our CoRoT-2 system observations, *Spitzer* was approximately 1.5 AU away from Earth and therefore had a significantly different field of regard than the Earth. For this reason, we could not obtain ground-based optical observations of the system around the time of the *Spitzer* observations to monitor stellar variability.

Instead, we estimate the upper limit of the magnitude of stellar variability at 4.5 μm using the observations acquired by the *CoRoT* mission. The *CoRoT* observations show that the optical stellar flux varies by at most 5% in 2-day intervals (Alonso et al. 2008), due to the inhomogeneous star spot area coverage of CoRoT-2. Using the reported mean star spots temperature (Silva-Valio et al. 2010), T_{o} , of 4700 ± 300 K, so assuming an isophotal wavelength, λ , of the CoRoT passband of 700 nm, one can approximate an out of transit stellar flux as:

$$F_s(T_*, T_{\text{o}}, f, \lambda) = (1 - f) B_{\lambda}(T_*, \lambda) + f B_{\lambda}(T_{\text{o}}, \lambda) \quad (\text{S6})$$

where $T_* = 5625$ K is the effective photospheric temperature of star, f is the fraction of total spot area and $B_{\lambda}(T, \lambda)$ is Planck's law. Assuming a 4.0% spot coverage on one of the hemispheres, we calculate that a 13% spot coverage on the other hemisphere corresponds to the maximal 5% flux variation. Extrapolating this to 4.5 μm , we find a stellar variability upper limit of 2.0%,

3.5.7 Surface Brightness

As described in the methods section, the planetary phase variation can be described more generally as a Fourier series of order N :

$$F_p(\xi) = F_0 + \sum_{j=1}^N C_j \cos(j\xi) + D_j \sin(j\xi) \quad (\text{S7})$$

where ξ is the orbital phase. Note that sinusoidal modes with odd j other than $j = 1$ are not expected to have a phase function signature for an edge-on orbit [Cowan & Agol \(2008\)](#); [Cowan et al. \(2013\)](#). If the rotation period of the planet is known, then phase variations allow us to constrain the longitudinal brightness of a planet. For tidally locked planets, the above phase variation corresponds to a longitudinal surface brightness map $J(\phi)$ given by:

$$J(\phi) = A_0 + \sum_{j=1}^N A_j \cos(j\xi) + B_j \sin(j\xi) \quad (\text{S8})$$

where ϕ is the longitude from the substellar point. One can directly relate the coefficient from equations S7 and S8 [Cowan & Agol \(2008\)](#):

$$\begin{aligned} A_0 &= \frac{1}{2}F_0 \\ A_1 &= \frac{2}{\pi}C_1 \\ B_1 &= \frac{-2}{\pi}D_1 \\ &\vdots \\ A_j &= (-1)^{j/2} \left[\frac{-(j^2-1)}{2} \right] C_j \\ B_j &= (-1)^{j/2} \left[\frac{(j^2-1)}{2} \right] D_j \end{aligned} \quad (\text{S9})$$

where j is even. Phase variations do not provide any latitudinal brightness constraints for an edge-on orbit. One can therefore express the flux contribution of an infinitesimal longitudinal slice as:

$$J(\phi) = \int_0^\pi I(\phi, \theta) \sin^2 \theta d\theta \quad (\text{S10})$$

where θ is the latitude from the substellar point and $I(\phi, \theta)$ is the brightness at the coordinates (ϕ, θ) . Assuming that the brightness drops off away from the equator as the sine of co-latitude, one can express intensity at a infinitesimal surface area at longitude ϕ and latitude θ as:

$$I(\phi, \theta) = \frac{3}{4}J(\phi) \sin(\theta). \quad (\text{S11})$$

Epilogue

In this chapter, I present the first of many pieces of evidences that the climate of hot Jupiters is not solely governed by their current orbital configuration and cannot be explained by pure hydrodynamical simulations. For example, the westward offset of CoRoT-2b could be linked to its youth and rotational state. To analyze the data set presented in this chapter, I conceptualized and developed the *Spitzer* Phase Curve Analysis (SPCA) pipeline, an open-source, modular analysis package that uses a variety of detector noise modelling. The pipeline was later improved and streamlined by my colleague Taylor Bell and has since been used for a series of investigations (e.g. [Bell et al. 2019](#); [Keating et al. 2019](#)).

Later, I joined the *Spitzer* Ultimate Phase Curve collaboration and helped acquire and analyze phase curves observations of hot Jupiters to uncover the atmospheric processes at play. My early contribution to atmospheric characterization of exoplanets with *Spitzer* led to 2 successful *Spitzer* programs that doubled the number of photometric phase curves observations ([Bean et al. 2018](#); [Beatty et al. 2018](#)). As a result, it opened the doors to comparative exoplanetology approaches to investigate the diversity of short-period planets. Since, population study approach is now a recurrent theme for many successful programs and future missions such as the *Ariel* Exoplanet Surveyor, a European Space Mission launching in the late 2020's. I've co-authored preliminary comparative exoplanetology studies ([Keating et al. 2019](#); [Bell et al. 2021](#); [May et al. 2022](#)) where we find the hot Jupiters to have uniform nightside temperatures which is suggestive of cloud formation of the same species or same cloud-top temperatures.

Chapter 4

Pixel Level Decorrelation in Service of the *Spitzer* Microlens Parallax Survey

*This thesis chapter originally appeared in the literature as
Dang et al. 2020, Monthly Notices of the Royal Astronomical Society*

Authors

Lisa Dang^{1,2,3}, Sebastiano Calchi Novati², Sean Carey², Nicolas B. Cowan^{1,3}

¹ Department of Physics, McGill University, Montréal, QC, Canada

² IPAC, Mail Code 100-22, California Institute of Technology Pasadena, CA 91125, USA

³ Department of Earth & Planetary Sciences, McGill University, Montréal, Canada

Prologue

Though the concept of measuring the microlens satellite parallax effect had been known for decades (Refsdal 1966), the first space-based microlens parallax was observed over half a century later by *Spitzer* (Dong et al. 2007). With the increased importance of the search for microlensing planets, *Spitzer* carried out a pilot program in 2014 to obtain simultaneous space-based monitoring of exoplanetary microlensing events detected from ground-based surveys to constrain their mass and distance, one of the biggest challenge faced by the microlensing technique (Udalski et al. 2015b). Due to the success of the pilot program, the Spitzer Space Telescope acquired a new role as a microlens satellite to build a distribution of microlens planets towards the galactic bulge.

My work on SPCA and expertise on *Spitzer* detector systematics led to one of the few cross-disciplinary forays into the field of gravitational microlensing from atmospheric characterization. I was recruited by the Spitzer Microlensing Team to improve the photometric precision of their survey and was awarded a Visiting Graduate Fellowship to visit Caltech in 2017. In this chapter, I adapt Pixel Level Decorrelation (PLD) initially developed for atmospheric studies to the Spitzer Microlensing Survey. I show that PLD can further clean instrumental noise and remove leftover detector noise that mimics planetary anomaly.

Abstract

Microlens parallax measurements combining space-based and ground-based observatories can be used to study planetary demographics. In recent years, the Spitzer Space Telescope was used as a microlens parallax satellite. Meanwhile, *Spitzer* IRAC has been employed to study short-period exoplanets and their atmospheres. As these investigations require exquisite photometry, they motivated the development of numerous self-calibration techniques now widely used in the exoplanet atmosphere community. Specifically, Pixel Level Decorrelation (PLD) was developed for starrng-mode observations in uncrowded fields. We adapt and extend PLD to make it suitable for observations obtained as part of the *Spitzer* Microlens Parallax Campaign. We apply our method to two previously published microlensing events, OGLE-2017-BLG-1140 and OGLE-2015-BLG-0448, and compare its performance to the state-of-the-art pipeline used to analyses *Spitzer* microlensing observation. We find that our method yields photometry 1.5–6 times as precise as previously published. In addition to being useful for *Spitzer*, a similar approach could improve microlensing photometry with the Nancy Grace Roman Space Telescope.

4.1 Introduction

Gravitational microlensing is a powerful tool to discover planets through the gravitational effect they have on light from more distant sources. Unlike other planet detection methods, gravitational lensing does not rely on the detection of photons from the planet or its host star. Therefore, this method allows us to find planets well beyond the Solar neighborhood. Moreover, in contrast with the other detection methods, gravitational microlensing is best suited to detecting planets beyond their stars’ snowline (for a review, see [Gaudi 2012](#); [Tsapras 2018](#)).

In most microlensing events, the primary observable is the Einstein timescale:

$$t_E = \frac{\theta_E}{\mu_{rel}}, \quad (\text{S1})$$

where μ_{rel} is the lens-source relative proper motion and θ_E is the angular Einstein radius, defined as

$$\theta_E = \sqrt{\kappa M_L \pi_{rel}}, \quad (\text{S2})$$

where M_L is the mass of the lens, π_{rel} is the source-lens relative parallax and κ is a constant. The latter quantities are defined as

$$\pi_{rel} = \left(\frac{D_L - D_S}{D_L D_S} \right) \text{AU} \quad (\text{S3})$$

and

$$\kappa = \frac{4G}{c^2 \text{AU}} \simeq 8.14 \frac{\text{mas}}{M_\odot}, \quad (\text{S4})$$

where D_S and D_L are the distance to the source and the lens, respectively (Yee et al. 2015b).

Hence, the lens’s mass and distance, M_L and D_L , and the relative motion between the source and the lens, μ_{rel} , are encoded in the primary observable, t_E , and are difficult to disentangle. In most planetary microlensing lightcurves, it is possible to determine θ_E via the finite source effect (Yoo et al. 2004). Assuming the distance to the source is known, e.g., for observations towards the Bulge, most sources are Bulge stars, the only degeneracy remaining is between the mass of the lens and the distance to the lens.

One way of breaking this degeneracy is by measuring a quantity known as the microlens parallax vector, $\boldsymbol{\pi}_E$, defined as

$$\boldsymbol{\pi}_E = \frac{\pi_{rel} \boldsymbol{\mu}_{rel}}{\theta_E \mu_{rel}}. \quad (\text{S5})$$

One can measure the microlens parallax by simultaneously observing an event from two well-separated observatories. The two observatories will see a different alignment between the lens and the source, so the projected separation and time of closest alignment will be different. This requires that the two observatories are far enough from each other, $\mathcal{O}(1 \text{ AU})$, for the lightcurves to be significantly different (Refsdal 1966; Gould 1994).

At $>1 \text{ AU}$ away from Earth for the past 6 years, the *Spitzer* Space Telescope (Werner et al. 2004) was ideal for measuring microlens parallax (PI: A. Gould; PID 10036, 11006, 12013, 12015, 13005, 14012, PI: S. Dong; PID: 13250, PI: S. Carey; PID 14121). Following the successful 2014 pilot program, *Spitzer* took on a new role as a “microlens parallax satellite” with the primary objective of measuring the galactic distribution of exoplanets towards the bulge (Udalski et al. 2015b, 2018; Yee et al. 2015b,a; Calchi Novati et al. 2015a,b, 2018, 2019; Zhu et al. 2015b,a, 2016, 2017c,a; Shvartzvald et al. 2015, 2016, 2017, 2019; Street et al. 2016; Poleski et al. 2016; Bozza et al. 2016; Han et al. 2016, 2017, 2018; Chung et al. 2017, 2019; Shin et al. 2017, 2018; Ryu et al. 2018; Albrow et al. 2018; Wang et al. 2018; Shan et al. 2019; Jung et al. 2019; Li et al. 2019; Zang et al. 2020a,b; Gould et al. 2020; Hirao et al. 2020).

4.1.1 Decorrelation Techniques Developed for Spitzer Observations

We need accurate lens properties, so it is crucial to obtain excellent photometry. However, extracting high precision photometry from *Spitzer* observations can be challenging. The channel 1 ($3.6 \mu\text{m}$) of the IRAC instrument (Fazio et al. 2004) was used for the *Spitzer* Microlensing Campaign. With a mean pixel scale of $1.221''/\text{pixel}$ and a point spread function (PSF) with a mean full width at half maximum (FWHM) of $1.66''$, the images are moderately undersampled. The systematics are primarily due to the convolution of changes in the telescope pointing and the significant variation of the sensitivity across each pixel. Inconveniently, the instrumental systematics can masquerade as the signature of planetary companions (e.g., Poleski et al. 2016).

Many techniques for decorrelating structured noise from astrophysical signals in IRAC data have been developed over the past decade. Ingalls et al. (2016) tested the effectiveness of widely used decorrelation methods. They reported that Pixel Level Decorrelation (PLD) (Deming et al. 2015), BiLinearly Interpolated Subpixel Sensitivity mapping (Stevenson et al. 2012) and Independent Component Analysis (Morello et al. 2014; Morello 2015) perform best to recover the underlying astrophysical signal.

The *Spitzer* microlensing team currently uses a Point Response Function (PRF) method* that uses information about the PSF, the detector sampling and the intrapixel sensitivity variation (Calchi Novati et al. 2015b). The method is tailored to work on time series data and, additionally, allows multiple sources to be fitted simultaneously. The current photometric extraction pipeline works for most targets, but there are cases showing possible residual red noise, e.g. OGLE-2016-BLG-1195Lb (Shvartzvald et al. 2017) and KMT-2018-BLG-0029 (Gould et al. 2020). In particular, the single lens model fitted to the *Spitzer* observations of OGLE-2015-BLG-0448 resulted in residuals with significant trends as seen in Figure 2 of Poleski et al. (2016) and reproduced in the bottom-right panel of our Figure 4.5. Poleski et al. (2016) acknowledged that the residuals could be due either to a planetary companion or instrumental systematics.

Photometry extraction procedures designed for planetary transit observations have been adapted for a microlensing survey with *K2* campaign 9 (*K2C9*, Henderson et al. 2016). Zhu et al. (2017b) presented a photometry extraction method based on the protocol developed by Huang et al. (2015) for less crowded fields. In this method, the instrumental systematics are decorrelated against the spacecraft's pointing and

*The concept of effective point spread function for the reduction of undersampled data was first discussed in Anderson & King (2000) for the analysis of *Hubble Space Telescope* data.

are fitted simultaneously with the astrophysical microlensing model.

Poleski et al. (2019) introduced an open-source alternative *K2* photometry extraction method build upon Wang et al. (2016)’s Causal Pixel Model, a data-driven instrumental model that was also developed for obtaining photometry for planetary occultations in less crowded fields. This Modified Causal Pixel Model differs in the use of the PRF to account for contamination from nearby sources.

Photometry extraction for *Spitzer* is not as challenging as for *K2*, as it benefits from more precise telescope pointing and smaller pixel scale, so there has been no attempt to use a photometry extraction method other than the pipeline described in Calchi Novati et al. (2015b). However, Koshimoto & Bennett (2020) claimed that the distribution of t_E and π_E for the sample of 50 single lens events from the 2015 *Spitzer* campaign cannot be reproduced by Galactic models. The authors suggested that investigating instrumental noise in the *Spitzer* photometry itself may resolve the discrepancy. Shan et al. (2019) also carried out Galactic model tests and found the model predictions to be consistent with the *Spitzer* parallaxes, but Koshimoto & Bennett (2020) claim this smaller sample of 13 published events suffers from publication bias. Better detector decorrelation methods could help resolve this tension.

In a similar vein to the work of Zhu et al. (2017b) and Poleski et al. (2019), we extend Pixel Level Decorrelation (Deming et al. 2015), developed for *Spitzer* secondary eclipse observations, to microlensing campaigns. In section 2, we discuss the differences between a typical observing sequence for short-period planets and for a microlensing event. In section 3, we describe our decorrelation method. We apply our method on a few sample data sets in section 4. We summarize and conclude in section 5.

4.2 Observations

4.2.1 Challenges with Spitzer Microlensing Campaign

Before we attempt to apply Pixel Level Decorrelation to the *Spitzer* Microlensing Survey, it is important to understand the differences between typical observations of transiting planets and of a microlensing event.

4.2.2 Timescale

Both science cases require time series photometry of a point source. However, the observing schemes are not quite the same. The duration of transiting planet observations is between a few hours for a transit or secondary eclipse to a couple days for full-orbit phase curves. Given the short length of the observations, time series observations of transiting exoplanets are generally collected in starrng-mode. On the other hand, a typical microlensing event lasts for weeks which is not ideal for starrng-mode observations over the full length of the event.

Moreover, a microlensing campaign only lasts for 40 consecutive days – the days during which the galactic bulge is visible from *Spitzer*. As the science objective of the *Spitzer* Microlensing Campaign is to constrain exoplanet demographics, it is crucial to maximize the number of targets during this visibility window and to get a large temporal coverage of the microlensing event. For this reason, *Spitzer* will only point at each target 4 times per day at most. In contrast, transiting planets are observed at a very high cadence (e.g., an image every second).

4.2.3 Pointing

Additionally, unlike transiting planet observations, microlensing observations are dithered on six or more slightly different positions in order to minimize the contribution from bad pixels and cosmic rays and to avoid background saturation (see Figure 4.1). Moreover, dithering the position of the PSF on different part of the detector allows for a better characterization of the shape of the PSF. Consequently, the pointing of the telescope for a microlensing campaign is not as precise as starrng-mode observations. During a starrng-mode observation, the target is positioned on the “sweet-spot” (peak response) and the centroid of the target’s point-spread function varies by 1/10th of a pixel. On the other hand, for dithered observations towards the Galactic bulge, the centroid of the source for each dither position changes by almost a pixel along the 40-days season.

4.2.4 Field Rotation

Another consequence of the long duration of microlensing events is that the orientation of the camera changes during the course of the observations. Hence, the target’s PSF and that of nearby sources rotate on the detector, and this may affect the *Spitzer* photometry as discussed for the observations of KMT-2018-BLG-0029 (Gould et al.

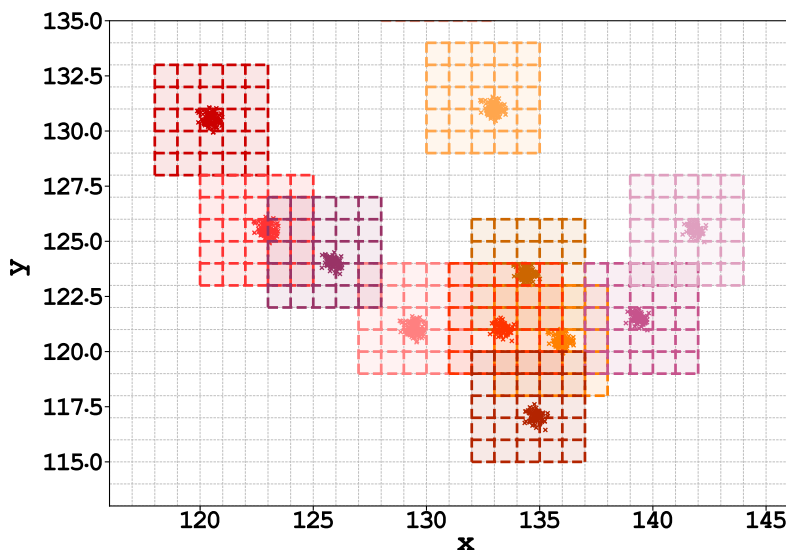


Figure 4.1: Visualization of the position of the PSF centroids and the **12 different dither** positions on the detector for *Spitzer* observations of OGLE-2015-BLG-0448. The dots represent the centroid for each observation and the different colors indicate a different dither position. The 5×5 grid around the centroids at each dither position represent the pixels used to extract the target’s photometry using Pixel Level Decorrelation.

2020). During the 40-day microlensing season, the rotation of the field of view is about 1 degree. For staring-mode observations, on the other hand, the field rotation is negligible.

4.2.5 Relative Brightness

Unlike transiting systems usually observed by *Spitzer*, microlensing events are often detected in crowded fields, e.g. towards the bulge of the galaxy. In general, transiting short-period planets observed with *Spitzer* are isolated bright targets, hence, the exposure time is approximately a second to avoid saturation. Microlensing targets are fainter and the exposure time is 30 seconds.

4.2.6 Magnitude of the Signal

In general, the amplitude of transits, secondary eclipses, and phase variations are a percent or less of the stellar flux. The magnification of microlensing events depends on the source-lens projected separation but is typically up to a few magnitudes.

4.2.7 Signal Coverage

Most transiting planets observed with *Spitzer* have well-known ephemerides. Hence it is possible to carefully plan the observations to cover the entire duration of the occultation. In contrast, microlensing events are unforeseeable and are first detected from ground-based surveys. These alerts then go through the selection process described by Yee et al. (2015a). The ones that pass the selection process are then scheduled for *Spitzer* follow-up observation. Given the unpredictable nature of microlensing events and the short visibility window of the galactic bulge, some *Spitzer* microlensing targets observations do not cover the baseline and/or the peak magnification of the event.

4.3 Method Description

Pixel Level Decorrelation (PLD) differs fundamentally from all other methods used to analyze *Spitzer* data. Other decorrelation methods rely on defining an instrumental noise model that depends on the position and shape of the point-response-function (PRF). In contrast, PLD decorrelates against the intensities of the individual pixels. Unlike the current photometric pipeline used for the *Spitzer* microlensing campaign, the instrumental effects are evaluated simultaneously with the microlensing model fit.

4.3.1 Photometry Extraction

For the photometric extraction, we identify the position of the target’s PRF on each *Spitzer*/IRAC image using the same procedure as Calchi Novati et al. (2015b). For each dither position, we identify the central pixel (see Figure 4.1), i.e. the pixel where the centroid of the target is most often located. Note that the centroid of the target varies by at most a pixel between epochs and the centroid of the target is sometimes located on one of the neighboring pixels. We use a 5×5 pixel square aperture to obtain an initial photometric measurement for each frame. To estimate the fractional flux recorded by each pixel, we divide by the sum of intensities in the 5×5 stamp. For consistency and better pixel characterization, we do not recenter the stamp on the centroid of the target for each frame, rather, we keep the stamp location fixed for each dither position (see Figure 4.1).

The raw photometry at a given time, F^{t_i} , is the sum of the intensities measured by pixels within the square aperture. To characterize and remove the systematics, we define the raw photometry as a multiplication of the astrophysical signal $F_{\mu lens}(t_i)$

and the instrumental noise $D(P_1^{t_i}, \dots, P_{25}^{t_i})$

$$F^{t_i} = \sum_{j=1}^{25} P_j^{t_i} = F_{\mu lens}(t_i) \times D(P_1^{t_i}, \dots, P_{25}^{t_i}), \quad (\text{S6})$$

where the superscript t denotes the epoch of the observations and the subscript i indicates the dither position, and j denotes the pixel ID (see Figure 4.2).

P_1	P_2	P_3	P_4	P_5
P_6	P_7	P_8	P_9	P_{10}
P_{11}	P_{12}	P_{13}	P_{14}	P_{15}
P_{16}	P_{17}	P_{18}	P_{19}	P_{20}
P_{21}	P_{22}	P_{23}	P_{24}	P_{25}

Figure 4.2: Pixel labelling

4.3.2 Detrending

In PLD, the detector model for each dither position is defined as some arbitrary function of the fractional flux measured by each pixel, P_j . To first order, we can approximate the detector model as linear:

$$D(P_1^{t_i}, \dots, P_{25}^{t_i}) = \sum_{j=1}^{25} c_j \frac{P_j^{t_i}}{\sum_n P_n^{t_i}} = \sum_{j=1}^{25} c_j \hat{p}_j^{t_i}, \quad (\text{S7})$$

where c_j is the PLD coefficient corresponding to the j th pixel and $\hat{p}_j^{t_i}$ is the fractional flux measured by the j th pixel at a given time, t_i . As the instrumental systematics is not expected to behave the same way at different location on the detector, we allow each dither position, i , its own independent PLD coefficients.

In principle, as PLD uses pixel fractional fluxes as regressors, the detector model does not need to know what causes variations in pixel fractional fluxes to model them. In particular, any effect that leads to changes in pixel fractional fluxes such as the translation and rotation of the field would be modeled by PLD.

4.3.3 Astrophysical Model

We can fit a point-source-point-lens model (1L1S) and a binary-lens model (2L1S) to the *Spitzer* data. The single-lens magnification $A(t)$ is modelled with a standard (Paczynski 1986) model with the time of closest alignment between the lens and the source, t_0 , the impact parameter, u_0 , and the Einstein ring crossing time, t_E , as fitting parameters. The magnification for a 2L1S is evaluated using the `VBinaryLensing` algorithm (Bozza 2010; Bozza et al. 2018) described by 4 additional parameters: the planet-host projected separation in units of θ_E , s , the planet-host mass ratio, q , the angular radius of the source in units of θ_E , ρ , and the angle between the planet-host axis and the trajectory of the source, α . The astrophysical signal as seen from the observer, $F_{\mu lens}(t_i)$, is also dependent on the baseline flux F_b and the source's flux F_s :

$$F_{\mu lens}(t_i) = F_b + F_s \cdot A(t_i). \quad (\text{S8})$$

If *Spitzer* observations include the baseline and the peak of the microlensing event, then we can estimate the microlensing parameters solely using *Spitzer* observations. Otherwise, we also use published ground-based observations from surveys such as the Optical Gravitational Lensing Experiment (OGLE; Udalski et al. 2015a) to further constrain the astrophysical parameters. In this scenario, we use the `MulensModel` package to evaluate the microlensing lightcurves (Poleski & Yee 2019).

Simultaneous ground-based and space-based observations allow us to constrain the microlens parallax vector components, $\boldsymbol{\pi}_E = (\pi_{E,N}, \pi_{E,E})$. We use the location coordinates of the ground-based telescope and *Spitzer* for the duration of the observations to obtain the magnifications as seen from each observatory, $A_g(t_i)$ and $A_s(t_i)$. Hence, the astrophysical signal for the ground-based telescope and space-based satellite, $F_{\mu lens,g}(t_i)$ and $F_{\mu lens,s}(t_i)$ are modelled as:

$$\begin{aligned} F_{\mu lens,g}(t_i) &= F_{b,g} + F_{s,g} \cdot A_g(t_i) \\ F_{\mu lens,s}(t_i) &= F_{b,s} + F_{s,s} \cdot A_s(t_i) \end{aligned} \quad (\text{S9})$$

where $F_{b,g}$ and $F_{b,s}$ are the baseline flux for the ground-based and space-based lightcurves, respectively, and $F_{s,g}$ and $F_{s,s}$ are the source flux as seen from the ground-based and space-based observatory, respectively.

4.3.4 Regressors

As mentioned above, we first obtained a raw time series photometry for each dither position, i , Y_i with N_{dat_i} data using aperture photometry. We initially fit a 1L1S or

2L1S model to the raw light curve to obtain initial estimates for the astrophysical parameters. Since PLD uses the fractional flux from each pixel as regressors, the total number of regressors is $N_{reg,total} = 25 \times N_{dither}$, where N_{dither} is the number of dither position for a given set of observations. In order to apply PLD on dithered observations, we evaluated the detector model parameters separately for each dither position but kept the astrophysical model the same for all dithered position.

We use the fractional flux of a 5×5 stamp, hence there are $N_{reg} = 25$ regressors per dither position. For each dither position i , we can now express equation S6 in vector form as

$$Y_i = A_i X_i \quad (\text{S10})$$

where A_i is the $N_{dat_i} \times N_{reg}$ design matrix constructed with the set regressors $\hat{p}_j^{t_i}$ from equation S7 multiplied by the astrophysical model $F_{\mu lens}(t_i)$ from equation S8. Hence, the elements of A_i are defined as $a_{i,j} = F_{\mu lens}(t_i) \hat{p}_j^{t_i}$. X_i is the $N_{reg} \times 1$ vector containing the PLD coefficients.

In other words, we construct the following matrices:

$$\begin{aligned} Y_i &= \begin{bmatrix} y_1 \\ y_2 \\ \dots \\ y_{N_{dat_i}} \end{bmatrix} \\ A_i &= \begin{bmatrix} a_{1,1} & a_{1,2} & \dots & a_{1,N_{reg}} \\ a_{2,1} & a_{2,2} & \dots & a_{2,N_{reg}} \\ \dots & \dots & \dots & \dots \\ a_{N_{dat_i},1} & a_{N_{dat_i},2} & \dots & a_{N_{dat_i},N_{reg}} \end{bmatrix} \\ X_i &= \begin{bmatrix} c_1 \\ c_2 \\ \dots \\ c_{N_{reg}} \end{bmatrix}. \end{aligned} \quad (\text{S11})$$

For a given astrophysical model, $F_{\mu lens}(t_i)$, equation S10 is linear. Hence, we can evaluate the PLD coefficients analytically by solving the generalized least square problem for each trial astrophysical model

$$X_i = [A_i^T \ C_i^{-1} \ A_i]^{-1} [A_i^T \ C_i^{-1} \ Y_i] \quad (\text{S12})$$

where C_i is the $N_{dat_i} \times N_{dat_i}$ covariance matrix of the data

$$C_i = \begin{bmatrix} \sigma_{y_1}^2 & 0 & \dots & 0 \\ 0 & \sigma_{y_2}^2 & \dots & 0 \\ \vdots & \vdots & \ddots & \vdots \\ 0 & 0 & \dots & \sigma_{y_{N_{dat_i}}}^2 \end{bmatrix}. \quad (\text{S13})$$

4.3.5 Fitting Process

To fit the lightcurves, we develop two fitting strategies. The first is to fit only the *Spitzer* data and the second is to simultaneously fit ground-based and space-based observations when the *Spitzer* data alone are insufficient to constrain the microlensing parameters. In either case, we use a Markov Chain Monte Carlo (MCMC) to estimate the fit parameters and their uncertainties.

Spitzer Observations Solely

To demonstrate our new detrending approach, we re-analyzed published *Spitzer* microlensing data (Poleski et al. 2016; Calchi Novati et al. 2018). We first fit the astrophysical model to the raw photometry with a Levenberg–Marquardt (L-M) algorithm, using parameter values close to those from the literature as initial values.

The estimates obtained from the initial minimization are then used as initial guesses for our MCMC. We use `emcee` (Foreman-Mackey et al. 2013) to estimate the parameters that maximize the log-likelihood, $\ln L$:

$$\begin{aligned} \ln L = & -\frac{\chi_{Spit}^2}{2} - \sum_{i=1}^{N_{dat}} \ln \sigma_{y_i} \\ & - \frac{N_{dat}}{2} \ln 2\pi + \ln L_{reg} \end{aligned} \quad (\text{S14})$$

where χ_{Spit}^2 is the usual badness-of-fit,

$$\chi_{Spit}^2 = \sum_{i=1}^{N_{dat}} \frac{[F(t_i) - F_{\mu lens}(t_i) \times D(P_1^{t_i}, \dots)]^2}{\sigma_{y_i}^2}, \quad (\text{S15})$$

and $\ln L_{reg}$ is an added term to constrain the flexibility of PLD and is defined as

$$\begin{aligned} \ln L_{reg} = & - \sum_{i=1}^{N_{dat}} \frac{[F(t_i) - F_{\mu lens}(t_i)]^2}{2\sigma_{raw}^2} \\ & - N_{dat} \ln \sigma_{raw} - \frac{N_{dat}}{2} \ln 2\pi \end{aligned} \quad (\text{S16})$$

where σ_{raw} is an estimate of the photometric scatter of the raw data. Without this term, our detector model tends to overfit the data and absorb the astrophysical flux variation. Since we are confident that the slow and large flux variation is due to microlensing magnification of the primary lens, we use the difference between the astrophysical model and raw lightcurve to regulate our MCMC.

We first fit the astrophysical model to the raw photometry with a L–M and use this fit as the initial guess for our MCMC. We initialize 300 MCMC walkers widely distributed around this guess. Note that only the astrophysical parameters are jump parameters: the PLD coefficients are evaluated analytically at each step of the MCMC. We perform an initial burn-in to let the walkers explore a wide region in parameter space during which each walker performs 300 steps to identify the region in parameter space that yields the greatest log-likelihood. We then perform an MCMC where the walkers are spread around the best parameter space region until our MCMC walkers converge. To insure the convergence of our MCMC, we require that 1) the log-likelihood of the best fit does not change over last 1000 steps of the MCMC chain and 2) the distribution of walkers along each parameters over the last 1000 steps is constant. Lastly, we build a posterior probability distribution and compute the 1σ confidence region of each parameter by marginalizing over all the walkers, over the last 1000 MCMC steps, along each parameter.

Simultaneous Ground-Based and *Spitzer* Observations

If we cannot evaluate the microlensing parameters from the *Spitzer* observations alone, we use published ground-based observations to further constrain the microlensing parameters by measuring the microlens parallax. As explained in section 3.3, both ground-based and space-based lightcurves are generated and fitted simultaneously. To accommodate the additional data set, we modify the log-likelihood function to

$$\begin{aligned} \ln L = & -\frac{\chi_{Spit}^2}{2} - \sum_{i=1}^{N_{dat,s}} \ln \lambda_s \sigma_{y_{i,s}} \\ & - \frac{N_{dat,s}}{2} \ln 2\pi + \ln L_{reg} + \ln L_{ground}, \end{aligned} \quad (S17)$$

where $\ln L_{ground}$ accounts for the goodness-of-fit to the ground-based observations and is defined as

$$\begin{aligned} \ln L_{ground} = & - \sum_{i=1}^{N_{dat,g}} \frac{[F_g(t_i) - F_{\mu lens,g}(t_i)]^2}{2(\lambda_g \sigma_{y_{i,g}})^2} \\ & - \sum_{i=1}^{N_{dat,g}} \ln \lambda_g \sigma_{y_{i,g}} - \frac{N_{dat,g}}{2} \ln 2\pi. \end{aligned} \quad (S18)$$

The s and g subscripts denote the space-based and ground observations, respectively. Following [Yee et al. \(2012\)](#) and [Calchi Novati et al. \(2018\)](#), we multiply the

Spitzer uncertainties, $\sigma_{y_{i,s}}$ and σ_{raw} , by a factor, λ_s , and the ground-based observations uncertainties, $\sigma_{y_{i,g}}$, by λ_g . We then fit the data using the procedure in the previous subsection with the addition of the scaling factors as fit parameters.

4.3.6 Model Comparison

While most microlensing analyses use χ^2 as a metric for model comparison, we opted to use the Bayesian Information Criterion (BIC) instead, particularly when comparing models with different number of parameters such as the 1L1S and 2L1S models. Generally, increasing the number of parameters in a model also increased its flexibility. Consequently, the fit using a model with more parameters is likely to have a smaller χ^2 . For this reason, we compute the BIC for each model (Schwarz 1978; Wit et al. 2012):

$$BIC = N_{\text{par}} \ln N_{\text{dat}} - 2 \ln L \quad (\text{S19})$$

where N_{par} is the number of fit parameters, N_{dat} is the total number of ground-based and space-based data points and $\ln L$ is the log-likelihood function defined in section 4.3.5.

4.4 Examples

We applied our method to two microlensing events. Note that, we assume that the target is the only time-variable source in the aperture box used to extract the raw photometry. In principle, if the nearby sources are stable, then the time-varying contamination from these sources will be modelled by PLD. However, if they are variable sources, then one would need to model their variability as well, since PLD only decorrelates against non-astrophysical variation. For this reason, we selected targets that are located in less crowded fields or with only stable and fainter sources nearby.

The first OGLE-2017-BLG-1140, has *Spitzer* observations covering the entire event, allowing us to constrain the microlensing parameters solely with the space-based data. For the second example, OGLE-2015-BLG-0448, the *Spitzer* data do not cover the entire microlensing event. We therefore perform a simultaneous fit to the *Spitzer* and OGLE observations.

Moreover, we selected these published events because the *Spitzer* observations offer good coverage of the entire event. Note that typical microlensing *Spitzer* observations do not benefit from the same generous coverage due to observing strategy

of the *Spitzer* microlensing program described in Yee et al. (2015a). Poor coverage of an event makes the estimation of the microlensing parameters more challenging, in particular the microlens parallax parameters. Since our objective is to test the effectiveness of PLD, we chose two events with good coverage to adequately test the performance of the detector model during the fitting process.

4.4.1 OGLE-2017-BLG-1140b

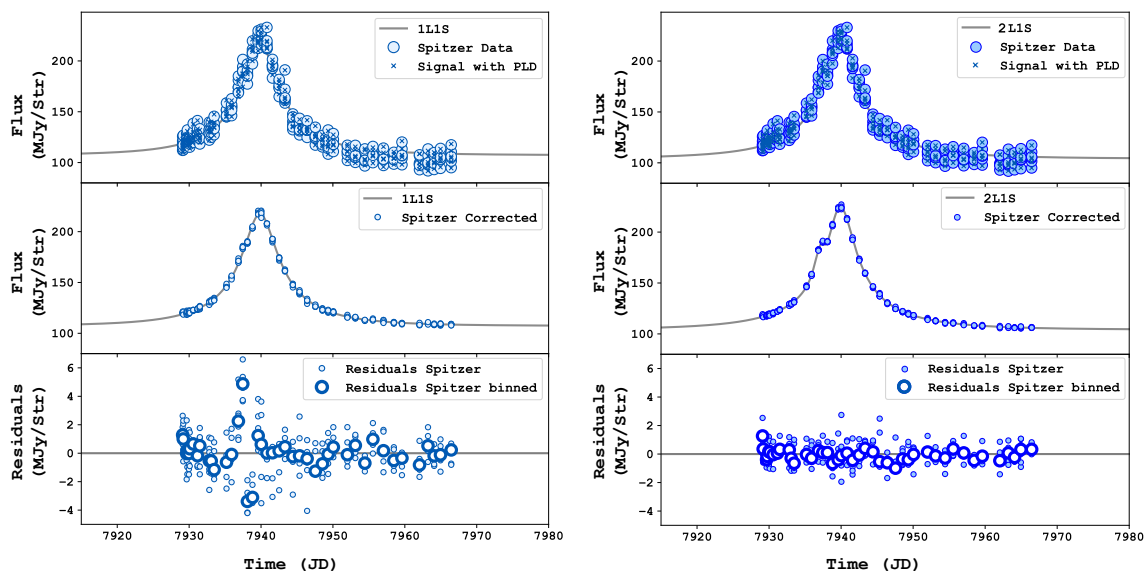


Figure 4.3: The single-lens-single-source (1L1S; left) and binary-lens-single-source (2L1S, right) fits to the *Spitzer* observations of OGLE-2017-BLG-1140. The top panels show the raw aperture as the blue circles, while the blue x’s represent the best-fit model including the detector noise model. The grey line represents the best-fit astrophysical model. The second panels show the corrected photometry after Pixel Level Decorrelation. Again, the grey line represents the best-fit astrophysical model. The bottom panels show the residuals as filled blue circles and binned residuals for each epoch as white-filled circles.

The event OGLE-2017-BLG-1140, (RA, Dec) = (17:43:31.93, -24:31:21.6) was first analyzed by Calchi Novati et al. (2018). In their analysis, the *Spitzer* lightcurve exhibits a stronger deviation from the single lens model than the deviation in ground-based lightcurve. We opt to apply our method solely to the space-based observations as it covers the entire event allowing us to estimate the microlensing parameters without ground-based observations. The *Spitzer* observations consist of 43 epochs, each consisting 6 dither positions. We first fit a single lens model to the raw lightcurve

to estimate an initial root mean square (RMS) residuals of 6.80 MJy/str. We fit a single lens and binary lens models to the observations using the method described in section 3.5.1; the results are listed in Table 5.2 and shown in Figure 4.3. While Calchi Novati et al. (2018) do not report the best-fit parameters for their 1L1S fit, their best-fit parameters for the binary lens model to the *Spitzer* lightcurve are within 3σ of ours.

The final residual RMS of our PLD method is ~ 4 and ~ 9 times lower than the raw photometric scatter, for the single lens and binary lens fit, respectively. We report each fit’s Bayesian Information Criterion (BIC) to compare their goodness of fit. There is a noticeably larger scatter in the residuals from the single lens model in Figure 4.3. The scatter is significantly more pronounced near the time of planetary anomaly predicted by the binary lens model. Additionally, we see in Table 5.2 that the binary lens model is strongly preferred with a $\Delta\text{BIC} > 1000$. This test confirms that our detector model is not overfitting the planetary anomaly in the *Spitzer* data.

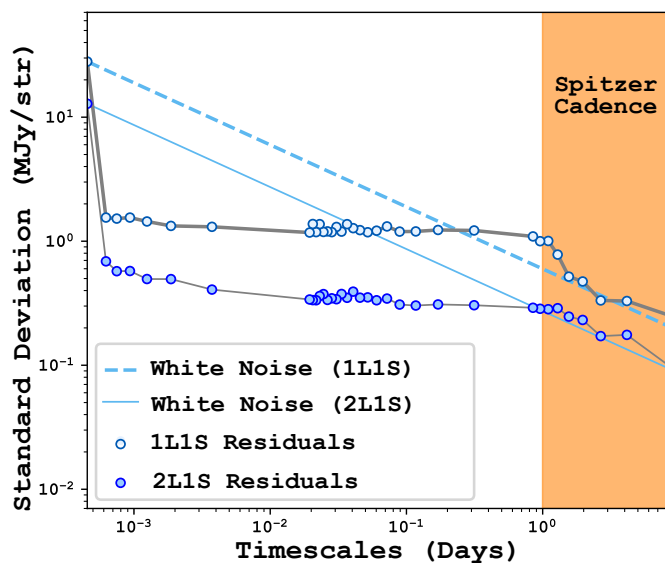


Figure 4.4: Standard deviation of our models fit to the *Spitzer* observations of OGLE-2017-BLG-1140 on different timescales. The dashed and solid light blue lines represent the expected standard deviations for the single lens and binary lens model if our residuals had been white noise. The light and dark blue dots are the calculate standard deviations for the 1L1S and 2L1S models, respectively. The orange-shaded area represents the timescales of interest for microlensing anomalies in the *Spitzer* data.

We measure the level of correlation in the residuals of our fits by calculating the standard deviation of the binned residuals (Figure 4.4). We compare them with

expected standard deviations if the residuals were white noise. We see that the scatter in the residuals for the single lens fit is consistently larger than the binary fit which confirms that the binary model is preferred. Note that the step-like residual RMS is due to the non-regular cadence of the data: the roughly constant RMS scatter in Figure 4.4 for timescales shorter than a day is due to the epoch cadence of the observations and the large step at very short timescale is evaluated timescale shorter than the time interval between two exposures at two different dither positions within the same epoch. Since the cadence of observations is on the order of 1 day, only anomalies on longer timescales can be confidently detected; our residuals RMS reaches the white noise limit on these timescales.

4.4.2 OGLE-2015-BLG-0448

The event OGLE-2015-BLG-0448, (RA, Dec) = (18:10:14.38, -31:45:09.4), was first presented by Poleski et al. (2016) who used the photometry from Calchi Novati et al. (2015b). The ground-based observations display no significant deviation from the single lens model. The *Spitzer* residuals, however, show an obvious deviation from a 1L1S model. There are many possible explanations for correlated residuals: 1) leftover instrumental systematics or 2) possible microlensing origin. The latter is possible in principle since the ground-based and space-based observatories probe different parts of the Einstein ring (Gould & Horne 2013). For example, the binary anomaly of OGLE-2018-BLG-1130 was only detected by *Spitzer* while showing no binarity in the ground-based observations (Wang et al. 2018).

For OGLE-2015-BLG-0448, Poleski et al. (2016) explored different possible microlensing scenarios to explain the data: 1) a binary source or 2) a binary lens. The

Table 4.1: OGLE-2017-BLG-1140 Fit Parameters Based on *Spitzer* Data

Parameter	Single Lens	Binary Lens
BIC	5671.78	4231.42
t_0 [HJD-2457939.0]	0.848 ± 0.007	0.789 ± 0.007
u_0	0.192 ± 0.01	0.125 ± 0.007
t_E [days]	$12.6^{+0.6}_{-0.5}$	16.2 ± 0.8
s	...	0.9 ± 0.02
q	...	$0.0048^{+0.0006}_{-0.0005}$
ρ	...	0.032 ± 0.003
α [rad]	...	$0.59^{+0.008}_{-0.007}$
$F_{b,Spitzer}$	82.0 ± 1.0	86.5 ± 1.0
$F_{s,Spitzer}$	$26.0^{+2.0}_{-1.0}$	18.0 ± 1.0
RMS [MJy/str]	1.57	0.71

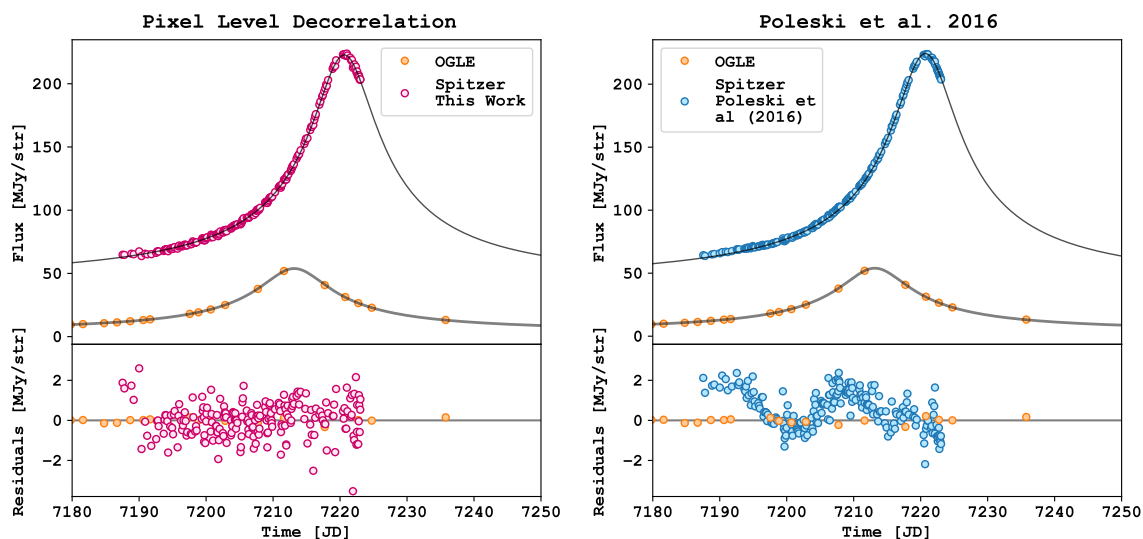


Figure 4.5: Our best-fit 1L1S model with the lowest BIC, (+, −), and Poleski et al (2016)’s 1L1S model with the lowest χ^2 , (−, +), are shown in the left and right panel, respectively. In the top panels, the pink and blue dots represent our PLD corrected lightcurve and the photometry obtained on the current *Spitzer* Microlensing pipeline described in Calchi Novati et al. (2015b), respectively. The orange dots represent the OGLE photometry. In the bottom panels, the pink and blue dots represent the residuals from our PLD decorrelation and the current *Spitzer* microlensing pipeline, respectively. Note that PLD removes the correlated residuals in the Poleski et al (2016) data that could be mistaken for a planetary anomaly.

binary source hypothesis is ruled out as the source is already very red, so it would also appear in the OGLE data. As for the binary lens scenario, they attempt a binary lens fit to the observations and find that a Saturn-mass planet can explain the observations. They also note that the best-fitting binary lens model does not remove all of the time-correlated residuals, hence, unmodeled systematics is not ruled out. Consequently, they do not claim to have detected a planet.

We apply our PLD method to this event by fitting a single-lens-single-source 1L1S model to the data. Since the *Spitzer* observations only partially cover the event, we used OGLE ground-base observations to further constrain the microlensing parameters as described in section 3.5.1. The *Spitzer* observations consist of 210 epochs, each consisting of 6 different dithers. A total of 12 dither positions were used as shown in Figure 4.1. For the OGLE data, we used 59 data points from HJD = 2457084.88043 to HJD = 2457301.5155. The single lens model suffers from a four-fold degeneracy. The results from our fits are presented in Table 4.2. The raw *Spitzer* photometry had an RMS scatter 5.90 MJy/str and our method reduced the scatter

Table 4.2: OGLE-2015-BLG-0448 Fits Parameters Based on *Spitzer* and OGLE Data

Parameter	Single Lens (+, +)	Single Lens (+, -)	Single Lens (-, +)	Single Lens (-, -)
BIC	18358.04	18352.85	18367.05	18358.76
$t_0[HJD - 2457213.0]$	$0.161^{+0.009}_{-0.01}$	0.162 ± 0.009	0.162 ± 0.009	0.160 ± 0.009
u_0	$0.0875^{+0.0007}_{-0.001}$	$0.0881^{+0.0007}_{-0.001}$	$-0.0879^{+0.001}_{-0.0007}$	$-0.088^{+0.0009}_{-0.0007}$
t_E [days]	$60.8^{+0.6}_{-0.4}$	$60.6^{+0.6}_{-0.4}$	$60.6^{+0.6}_{-0.4}$	$60.6^{+0.5}_{-0.4}$
$\pi_{E,N}$	-0.0178 ± 0.0003	-0.136 ± 0.001	$0.1145^{+0.0008}_{-0.0012}$	0.0014 ± 0.0003
$\pi_{E,E}$	$-0.0922^{+0.0008}_{-0.0007}$	$-0.0886^{+0.0008}_{-0.0006}$	$-0.1084^{+0.001}_{-0.0008}$	$-0.0968^{+0.0009}_{-0.0007}$
$F_{b,OGLE}$	$0.04^{+0.05}_{-0.03}$	$0.02^{+0.05}_{-0.03}$	$0.03^{+0.05}_{-0.03}$	$0.02^{+0.04}_{-0.03}$
$F_{s,OGLE}$	$4.71^{+0.04}_{-0.05}$	$4.73^{+0.04}_{-0.05}$	$4.73^{+0.04}_{-0.05}$	$4.73^{+0.04}_{-0.05}$
$F_{b,Spitzer}$	32.1 ± 0.3	32.0 ± 0.3	32.4 ± 0.3	32.1 ± 0.3
$F_{s,Spitzer}$	14.3 ± 0.1	$14.7^{+0.1}_{-0.2}$	13.7 ± 0.1	14.3 ± 0.1
λ_{OGLE}	2.0 ± 0.2	2.0 ± 0.2	2.0 ± 0.2	2.0 ± 0.2
$\lambda_{Spitzer}$	2.58 ± 0.04	$2.58^{+0.04}_{-0.03}$	2.59 ± 0.04	2.58 ± 0.04
RMS [MJy/str]	1.44	1.43	1.44	1.43

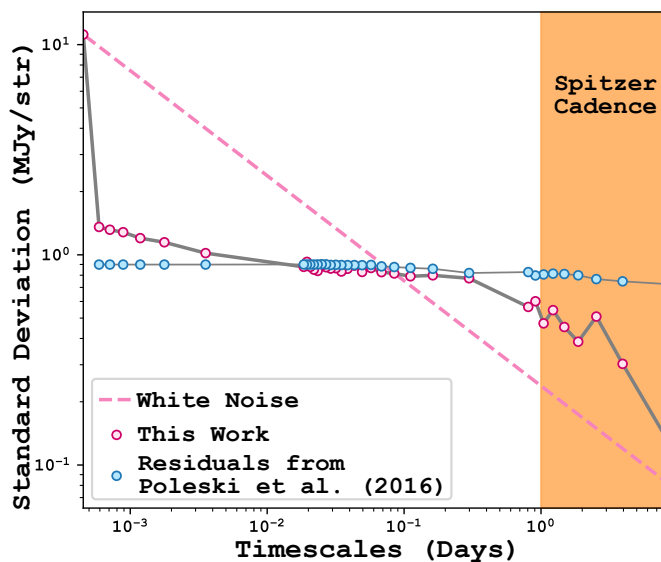


Figure 4.6: The standard deviation of our PLD corrected 1L1S (+, -) residuals and Poleski et al (2016)'s 1L1S (-, +) residuals are represented by the pink and blue dots, respectively. The dashed pink line represents the expected standard deviations if our residuals had been white noise. The orange-shaded area represents the timescales of interest for microlensing anomalies in the *Spitzer* data.

by a factor of ~ 4 .

In Figure 4.5, we compare our corrected photometry with the photometry from Poleski et al. (2016) obtained using Calchi Novati et al. (2015b)’s method. As *Spitzer* flux extracted by Calchi Novati et al. (2015b) is in arbitrary units, we rescaled their lightcurve such that the peak and the baseline is equal to our decorrelated lightcurve. We note that the significant trend observed by Poleski et al. (2016) is not present in our single lens fit residuals. Hence, the deviation from the single models in the previous analysis of OGLE-2015-BLG-0448 were likely due to detector systematics not accounted for by the Calchi Novati et al. (2015b) reduction. To further evaluate the performance of PLD, we evaluate the residuals RMS of our best-fit single lens model with the lowest BIC at different timescales and compare it with the residual RMS from Poleski et al. (2016)’s single lens fit. We note that Calchi Novati et al. (2015b)’s method combines all dithers per epoch to evaluate the photometry while we use all exposure in our decorrelation, hence, evaluating the scatter for a given timescale is essential for the comparison. The standard deviations vs. timescales calculations are presented in Figure 4.6. While Poleski et al. (2016)’s residuals are slightly less scattered at short timescales, they are significantly more correlated at timescales longer than the *Spitzer* observations cadence. On a timescale of ~ 9 days, our method reduced the noise by a factor of 5.9, when compared to the single lens and binary lens fit, respectively. On a timescale of ~ 4 and ~ 2.5 days, our method improves the noise by a factor of 2.5 and 1.5, respectively, in comparison with the photometry from Calchi Novati et al. (2015b). While our single lens residual RMS is above the photon noise limit, it still outperforms the current pipeline used for the *Spitzer* microlensing campaign.

4.5 Discussion and Conclusion

We present an alternative method to extract and reduce photometry for the *Spitzer* Microlensing campaigns using Pixel Level Decorrelation, a method initially developed to decorrelate lightcurves of transiting exoplanets with *Spitzer*. This method uses the fractional flux recorded by each pixel as regressors to model the systematics. PLD models the instrumental systematics and flux contribution from nearby stars. Advantages of this method includes not requiring precise centroid measurements for each exposure, not needing dithered observations, and better noise reduction.

We have tested PLD on *Spitzer* observations of OGLE-2017-BLG-1140 and OGLE-2015-BLG-0448. We find that PLD is able to reduce the RMS scatter in the raw photometry by at least a factor of 1.5. We also find that for the event OGLE-2015-

BLG-0448, our decorrelation produces photometry up to an order of magnitude more precise than the Calchi Novati et al. (2015b) pipeline on timescales of microlensing anomalies. We note that there are significant differences between the two methods. Most published *Spitzer* microlensing lightcurve analyses are done in 2 steps: first reduce the photometry, then evaluate the microlensing parameters. Similarly to photometry extraction methods developed for *K2* microlensing observations (Zhu et al. 2017b; Poleski et al. 2019), the PLD method fits the microlensing model and the noise model simultaneously.

We note that both events tested in this work have benefited from *Spitzer* observations with good coverage over the duration of the microlensing event. For events with poor coverage, the microlensing parameters will be difficult to constrain with great precision. However, to model the detector systematics with PLD, the key is to have more data to better characterize the detector noise. Even without full coverage of the event, PLD will be able to remove the systematics if there are a large number of exposures. The microlensing parameters, however, will have larger uncertainties.

The *Spitzer* Microlensing campaign has enabled unprecedented microlens parallax measurements to build a planet distribution in the galaxy. However, tensions have been claimed between the results from this campaign and prediction from commonly used Galactic models (Koshimoto & Bennett 2020) suggesting that the photometry extraction could be the source of error. Alternative photometry extraction schemes such as PLD could help investigate the source of the discrepancies.

The Pixel Level Decorrelation technique for noise characterisation is not uniquely applicable to *Spitzer* observations. For example, PLD has been successful when applied to *K2* observations of transiting exoplanets (Luger et al. 2016, 2018). Hence, given the versatility of this method, it could be adapted to other microlensing campaigns with other space telescopes such as the *Kepler* Space Telescope for the *K2C9* campaign.

The forthcoming Nancy Grace Roman Space Telescope, formerly known as the Wide Field Infrared Survey Telescope (*WFIRST*, Spergel et al. 2015), will perform a Galactic Exoplanet Survey (*RGES*) and is expected to detect thousands of exoplanets via microlensing (Penny et al. 2019; Johnson et al. 2020). However, its infrared detector will share similarities with *Spitzer*'s, including intra-pixel sensitivity variations. Beyond more standard methods to address this issue (Anderson & King 2000), the photometry reduction for the *RGES* may also benefit from decorrelation methods such as PLD.

Acknowledgements

We would like to thank our referee, D. Bennett, for constructive criticism. We would also like to thank P. Mroz for the discussions of microlensing modelling and R. Poleski for help with `MulensModel` and useful comments on the manuscript. This work was supported in part through a Visiting Graduate Researcher Fellowship (VGRF) at Caltech's Infrared Processing and Analysis Center (Caltech/IPAC), McGill University's Graduate Mobility Award, the Technologies for Exo-Planetary Science (TEPS) International Internship program, and the Natural Sciences and Engineering Research Council of Canada (NSERC)'s Postgraduate Scholarships-Doctoral Fellowship. This work is based on archival data obtained with the Spitzer Space Telescope, which is operated by the Jet Propulsion Laboratory, California Institute of Technology under a contract with NASA. Support for this work was provided by an award issued by JPL/Caltech.

Data Availability

The *Spitzer* data underlying this article are publicly available and were provided by NASA/IPAC Infrared Science Archive. The remaining data and code underlying this article will be shared on reasonable request to the corresponding author.

Epilogue

This chapter presents the first alternative reduction method for the *Spitzer* Microlensing Campaign. As discussed, contamination from instrumental effects and nearby sources are a large source of errors in the estimation of lens properties and some of the published *Spitzer* lightcurves exhibit significant residual noise. Indeed, (Koshimoto & Bennett 2020) proposed that detector systematics could be the source of discrepancy between the *Spitzer* microlensing results and Galactic models. Another way to resolve the classic mass-distance degeneracy is by measuring the proper motion of the lens relative to the source once they are out of alignment a few years later with a space-based telescope of adaptive optics (AO) (Bennett et al. 2007). Recent proper motion determination with follow-up Keck observations are discrepant with results from the *Spitzer* Microlensing Campaign and I am now collaborating with Katie Vandourou, Gioia Rau, and David Bennett at NASA Goddard to obtain follow-up AO observations of high-profile targets from the *Spitzer* Campaign and provide a PLD analysis to investigate these disagreements. Resolving these discrepancies will improve our ability to convert microlensing observable into useful units for demographics studies which is particularly relevant for the upcoming *Roman* microlensing surveys.

Even though *Spitzer* is now decommissioned, a consensus has not yet been concluded from the microlensing data set acquired from 2014 to 2020 and a systematically uniform analysis of the entire data set is therefore in order. To do so, I have been supervising an undergraduate student, Tarik Bouchoutrouch-Ku, to turn my PLD adaptation for *Spitzer* microlensing into open-source modular and user-friendly pipeline for the community to use, similar to the *Spitzer* Phase Curve Analysis pipeline. In addition, streamlining the PLD pipeline will enable the uniform analysis of the entire campaign.

Chapter 5

Thermal Phase Curves of XO-3b: an Eccentric Hot Jupiter at the Deuterium Burning Limit

*This thesis chapter originally appeared in the literature as
Dang et al. 2022, *The Astronomical Journal**

Authors

Lisa Dang^{1,2}, Taylor J. Bell³, Nicolas B. Cowan^{1,2,4,5}, Daniel Thorngren², Tiffany Kataria⁶, Heather Knutson⁷, Nikole K. Lewis⁸, Keivan G. Stassun⁹, Jonathan J. Fortney¹⁰, Eric Agol¹¹, Gregory Laughlin¹², Adam Burrows¹³, Karen A. Collins⁹, Drake Deming¹⁴, Diana Jovmir¹, Jonathan Langton¹⁵, Sara Rastegar¹⁶, and Adam Showman¹⁷

¹ Department of Physics, McGill University, Montréal, QC, Canada

² Institut de Recherche sur les Exoplanètes (iREx), Université de Montréal, QC, Canada

³ Bay Area Environmental Research Institute, NASA Ames Research Center, USA

⁴ Department of Earth & Planetary Sciences, McGill University, Montréal, Canada

⁵ Space Science Institute, 4765 Walnut St, Suite B, Boulder, CO, USA

⁶ NASA Jet Propulsion Laboratory, Pasadena, CA USA

⁷ Division of Geological & Planetary Sciences, California Institute of Technology, USA

⁸ Department of Astronomy and Carl Sagan Institute, Cornell University, Ithaca, NY, USA

⁹ Vanderbilt University, Department of Physics & Astronomy, Nashville, TN, USA

¹⁰ Department of Astronomy and Astrophysics, University of California, Santa Cruz, CA, USA

¹¹ Astronomy Department, University of Washington, Seattle, WA, USA

¹² Department of Astronomy, Yale University, New Haven, CT, USA

¹³ Department of Astrophysical Sciences, Princeton University, NJ, USA

¹⁴ Department of Astronomy, University of Maryland, College Park, USA

¹⁵ Physics Department, Principia College, Illinois, USA

¹⁶ Department of Earth Planetary Sciences, Northwestern University, Evanston, IL, USA

¹⁷ Lunar and Planetary Lab, University of Arizona Tucson, AZ, USA

Prologue

Most short-period planets with thermal phase curve measurements thus far are close-in exoplanets with their rotation synchronized. However, with constant insolation it is impossible to distinguish between the radiative timescale and advective timescale from phase curve observations. Meanwhile, the variable insolation experienced by eccentric planets allows one to break this degeneracy and constrain the average wind speed and the depth of the atmospheric convective layer. XO-3b is one of the best characterized eccentric hot Jupiter with *Spitzer* – repeated observations of XO-3b eclipses were extensively studied and were the subject of many studies of *Spitzer* systematics (Ingalls et al. 2016; Krick et al. 2020). Its thermal emission detectability and short orbital period made XO-3b the ideal target for a full-orbit phase curve. In this chapter, I present the 3.6 and 4.5 μm phase curve of a $\sim 12 M_{\text{Jup}}$ gas giant nearing the deuterium burning limit. I detect seasonal variation on an exoplanet and hints of excess thermal emission.

Abstract

We report *Spitzer* full-orbit phase observations of the eccentric hot Jupiter XO-3b at 3.6 and 4.5 μm . Our new eclipse depth measurements of 1770 ± 180 ppm at 3.6 μm and 1610 ± 70 ppm at 4.5 μm show no evidence of the previously reported dayside temperature inversion. We also empirically derive the mass and radius of XO-3b and its host star using Gaia DR3’s parallax measurement and find a planetary mass $M_p = 11.79 \pm 0.98 M_{\text{Jup}}$ and radius $R_p = 1.295 \pm 0.066 R_{\text{Jup}}$. We compare our *Spitzer* observations with multiple atmospheric models to constrain the radiative and advective properties of XO-3b. While the decorrelated 4.5 μm observations are pristine, the 3.6 μm phase curve remains polluted with detector systematics due to larger amplitude intrapixel sensitivity variations in this channel. We focus our

analysis on the more reliable $4.5 \mu\text{m}$ phase curve and fit an energy balance model with solid body rotation to estimate the zonal wind speed and the pressure of the bottom of the mixed layer. Our energy balance model fit suggests an eastward equatorial wind speed of $3.13_{-0.83}^{+0.26}$ km/s, an atmospheric mixed layer down to $2.40_{-0.16}^{+0.92}$ bar, and Bond albedo of $0.106_{-0.106}^{+0.008}$. We assume that the wind speed and mixed layer depth are constant throughout the orbit. We compare our observations with a 1D planet-averaged model predictions at apoapse and periapse and 3D general circulation model (GCM) predictions for XO-3b. We also investigate the inflated radius of XO-3b and find that it would require an unusually large amount of internal heating to explain the observed planetary radius.

5.1 Introduction

As a transiting planet orbits around its host star, the apparent brightness of the planet varies as seen by a distant observer. Infrared phase variations reveal a planet’s response to spatial, diurnal and seasonal forcing. Short-period planets on circular orbits are subject to strong tidal interaction with their host star and hence are expected to have zero obliquity and to be tidally spun down into synchronous rotation. This means that they don’t experience seasons or diurnal forcing, so their atmospheric circulation is driven by the fixed spatial pattern of stellar irradiation and Coriolis forces, resulting in steady-state circulation patterns (e.g. [Showman & Guillot 2002](#)). Their thermal phase curves can therefore be translated into a longitudinal thermal map of the planet.

While most hot Jupiters have circular orbits, a few have been found on eccentric orbits. These gas giants are expected to form either in-situ ([Bodenheimer et al. 2000](#)) or beyond the snow line in their protoplanetary disk far from their stellar hosts and later migrate inwards via gas disk ([Lin et al. 1996](#)), planet-planet scattering ([Rasio & Ford 1996](#)), secular interaction ([Wu & Lithwick 2011](#)) or Kozai-Lidov migration ([Weidenschilling & Marzari 1996](#); [Naoz et al. 2013](#)). In addition to providing insights into gas giants migration mechanisms, hot Jupiters on eccentric orbits are of particular interest for atmospheric studies.

Unlike their circular counterparts, eccentric hot Jupiters experience time-variable heating such that their phase curve reflects a balance between incoming flux, heat transport efficiency (a combination of rotation and winds), and time required to radiate away energy. Therefore, the variable stellar irradiation experienced by eccentric hot Jupiters allows us to break the degeneracy between the heat transport and radiative timescales that limits our studies of typical hot Jupiters on circular orbit ([Langton](#)

& Laughlin 2008; Iro & Deming 2010; Cowan & Agol 2011a; Kataria et al. 2013). In contrast with short-period planets on circular orbits, exoplanets on eccentric orbits present additional challenges when one attempts to retrieve information about their atmosphere from thermal phase observations. In particular, it is difficult to disentangle the flux variation due to the planet’s rotation and the change in stellar irradiation. While the dayside of the planet should experience spatial and temporal variability over the course of an orbit, the phase curve should be relatively stable from one orbit to the next (Showman et al. 2009; Lewis et al. 2010; Kataria et al. 2013).

Thermal phase variations have now been published for more than a dozen gas giants on circular orbits with the *Spitzer* Space Telescope: CoRoT-2b (Dang et al. 2018, PID 11073); HAT-P-7b (Wong et al. 2016, PID 60021); HD 149026b (Zhang et al. 2018, PID 60021); HD 189733b (Knutson et al. 2012, PID 60021); HD 209458b (Zellem et al. 2014, PID 60021); KELT-1b (Beatty et al. 2019, PID 11095); KELT-9b (Mansfield et al. 2020, PID 14059); KELT-1b (Beatty et al. 2019, PID 11095); KELT-16b (Bell et al. 2021, PID 14059); MASCARA-1b (Bell et al. 2021, PID 14059); Qatar-1b (Keating et al. 2020, PID 13038); WASP-12b (Cowan et al. 2012a, PID 70060; Bell et al. 2019, PID 90186); WASP-14b (Wong et al. 2015, PID 80073); WASP-18b (Maxted et al. 2013, PID 60185); WASP-19b (Wong et al. 2016, PID 80073); WASP-33b (Zhang et al. 2018, PID 80073); WASP-43b (Stevenson et al. 2017, PID 11001); WASP-76b (May et al. 2021, PID 13038); and WASP-103b (Kreidberg et al. 2018, PID 11099). The many published *Spitzer* thermal phase curves have also enabled various comparative studies (Adams & Laughlin 2018; Keating et al. 2019; Bell et al. 2021). Thermal phase curves have also been observed with the *Hubble* Space Telescope (e.g. Stevenson et al. 2014; Kreidberg et al. 2018; Arcangeli et al. 2019, 2021) and more recently with the Transiting Exoplanet Survey Satellite (e.g. Wong et al. 2020; Daylan et al. 2021; von Essen et al. 2021). In contrast, only 3 exoplanets with an eccentricity greater than 0.15 have published phase curves: HAT-P-2b (Lewis et al. 2013, PID 90032), GJ 436b (Lanotte et al. 2014, PID 30129) and HD 80606b (de Wit et al. 2016, PID 60102).

XO-3b (Johns-Krull et al. 2008) is an eccentric hot Jupiter ($e = 0.2769$) orbiting a F5V star (Figure 5.1) and is a tantalizing target for follow-up observations. With a mass of $M_p = 11.79 \pm 0.98 M_{\text{Jup}}$, XO-3b provides an important link between giant exoplanets and low-mass brown dwarfs. In addition, its unusually large radius measurements of $R_p = 1.295 \pm 0.066 R_{\text{Jup}}$ is difficult to explain with traditional evolution models for hot Jupiters with an age of $2.82^{+0.58}_{-0.82}$ Gyr (e.g. Liu et al. 2008; Winn et al. 2008). Finally, the incident stellar flux on XO-3b at periapse is 3.3 times that at apoapse, which could cause large variations in atmospheric temperature, wind speed, chemistry, and clouds.

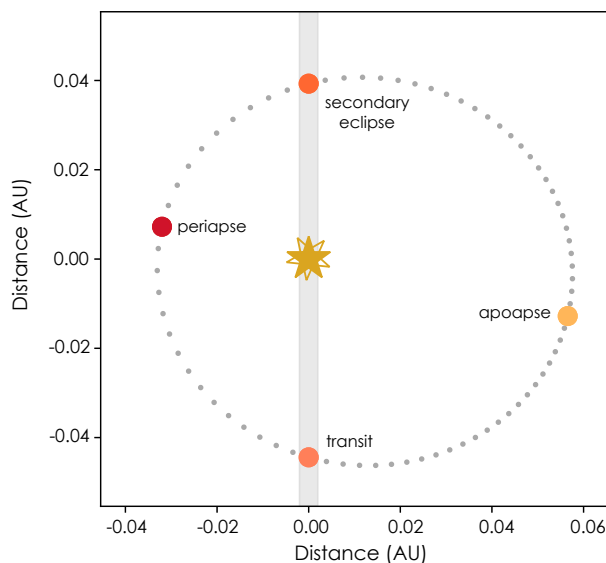


Figure 5.1: Top-view of XO-3b’s orbit with parameters from [Wong et al. \(2014\)](#). The gray dots represent the planet’s position at 1 hour intervals and the planet revolves counter-clockwise. The shaded area represents our line of sight (the Earth is off the bottom of the plot).

Naturally, the puzzling system of XO-3 has been the subject of various observational studies. Planets on eccentric orbits are often misaligned with their stellar spin. [Hébrard et al. \(2008\)](#) measured a sky-projected spin-orbit misalignment for the star XO-3 of $\lambda = 70 \pm 15^\circ$ using SOPHIE observations. This quantity has been revised by [Winn et al. \(2009\)](#) to $\lambda = 37.3 \pm 3.7^\circ$. [Turner et al. \(2017\)](#) obtained ground-based transit observations and suggest that the anomalously large transit depth they measure in *B*-band could be indicative of scattering in its atmosphere. [Machalek et al. \(2010\)](#) measured eclipses of XO-3b in the four *Spitzer*/IRAC wavebands to infer the planet’s vertical temperature profile. They found that the dayside of the planet exhibited a temperature inversion (temperature increasing with height over a limited pressure range). [Wong et al. \(2014\)](#) and [Ingalls et al. \(2016\)](#) analyzed 12 secondary eclipses of XO-3b at $4.5 \mu\text{m}$. These measurements favor a greater eclipse depth than reported by [Machalek et al. \(2010\)](#), and hence strengthen the claimed temperature inversion. With the baseline eclipse observations of XO-3b at $4.5 \mu\text{m}$ extended to 3 years, [Wong et al. \(2014\)](#) place an upper limit on the periastron precession rate of 2.9×10^{-3} deg/day.

In this paper, we present and analyze the full-orbit 3.6 and $4.5 \mu\text{m}$ phase curves of XO-3b obtained with the *Spitzer* Space Telescope. In addition, we analyze an unpublished $3.6 \mu\text{m}$ *Spitzer* secondary eclipse observation. We use these observations

to constrain the radiative and dynamical properties of the atmosphere of XO-3b. The observation and data reduction are presented in Section 5.2 and the models and methods are described in Sections 5.3 and 5.4. Our results are presented in Section 5.5. Section 5.6 summarizes the main conclusions from our analysis and presents ideas for future work.

5.2 Observation and Reduction

We observed two continuous full-orbit phase curves of XO-3b (PI H.A. Knutson, PID: 90032): one in each of the $3.6\ \mu\text{m}$ (channel 1) and $4.5\ \mu\text{m}$ (channel 2) bands of the Infrared Array Camera (IRAC; Fazio et al. 2004) on board the Spitzer Space Telescope (Werner et al. 2004). The observations at $3.6\ \mu\text{m}$ and $4.5\ \mu\text{m}$ were acquired on UT 2013 April 12-16 and UT 2013 May 5-8, respectively. Both observations were scheduled to start approximately 5 hours before the start of a secondary eclipse and end approximately 2 hours after the subsequent secondary eclipse. Due to long-term drift of the spacecraft pointing, the telescope was repositioned approximately every 12 hr in order to re-center the target. Hence the observations at each waveband were separated into 9 Astronomical Observation Requests (AORs). We used the sub-array mode with a 2 second frame time (effective exposure time of 1.92 s) for 3.56 days in each waveband which yielded a total of 2400 datacubes in each channel. Every datacube consists of 64 frames of 32×32 pixels ($39''\times 39''$) resulting in a total of 153,600 images in each waveband.

As explained later, the $3.6\ \mu\text{m}$ phase observations exhibit strong detector systematics during one of the secondary eclipse that biases the eclipse depth measurements. To better constrain the $3.6\ \mu\text{m}$ eclipse depth, we also analyze the eclipse portion of XO-3b's $3.6\ \mu\text{m}$ partial phase curve (PI: P. Machalek, PID 60058). The $3.6\ \mu\text{m}$ phase observations were acquired on UT 2010 March 21-23. Again, the sub-array mode with a 2 second frame time (effective exposure time of 1.92 s) was used and a total 419 datacubes were included in our analysis.

5.2.1 Data Reduction

We use the Spitzer Science Center's basic calibrated data (BCD), which have been dark-subtracted, flat-fielded, linearized and flux calibrated using version S19.2.0 of the IRAC software pipeline. Deming et al. (2011) first noted that the post-cryogenic *Spitzer*/IRAC data collected in sub-array mode exhibit frame-dependent background flux: they display a settling effect over the 64 frames as well as a sudden increase

or decrease in background flux at the 58th frame. Dang et al. (2018) found that data calibrated using the S19.2.0 pipeline exhibit frame-dependent flux modulation introduced during the sky dark subtraction stage. The 58th frame error and the flux modulation are both fixed using correction image stacks for each AOR; these were provided by the IRAC team.

We use the Spitzer Phase Curve Analysis Pipeline* (SPCA; Dang et al. 2018; Bell et al. 2021), an open-source, modular, and automated pipeline to reduce and analyze our data. After correcting for frame-dependent systematics, we convert the pixel intensity from MJy/str to electron counts and obtain time stamps for each exposure using values from each FITS file. We masked *NaN* pixels and perform a pixel-by-pixel 4σ sigma clip where the standard deviation, σ , for each pixel is determined along its respective datacube. We choose to mask rather than replace sigma-clipped pixels with average values to minimize the manipulation of the data. We then perform a pixel-level sigma-clipping by comparing each pixel with the pixel located at the same coordinate on all 64 frames of the same datacube and masking all 5σ outliers. Frames containing a sigma-clipped pixel located in a 5×5 pixel box centered on the central pixel of the target are discarded entirely.

We then evaluate the level of background flux for each frame by masking all the pixels within a 7×7 pixel box centered on the target and measuring the median pixel intensity of the remaining unmasked pixels. We then perform background subtraction on each frame. Finally, we estimate the centroid coordinates (x_0, y_0) for each frame using the flux-weighted mean along the x and y axes and measure the Point-Spread-Function (PSF) width $(\sigma_{x_0}, \sigma_{y_0})$ along the x and y axes.

5.2.2 Extracting the Photometry

Aperture Photometry

We perform aperture photometry using soft-edge and hard edge circular apertures as defined in Bell et al. (2021) with radii from 1.25 to 7.25 pixels. We center the aperture on the PSF flux-weighted mean centroid of each frame. To determine the best photometric scheme, we calculate the root-mean-squared (RMS) scatter from a smoothed lightcurve by boxcar averaging with a length of 50. Figure 5.2 shows the resulting RMS for all our considered aperture choices; we select the scheme with the smallest RMS. We find that the best photometric schemes are hard-edge apertures

*Details about how to install and use SPCA can be found at <https://spca.readthedocs.io>

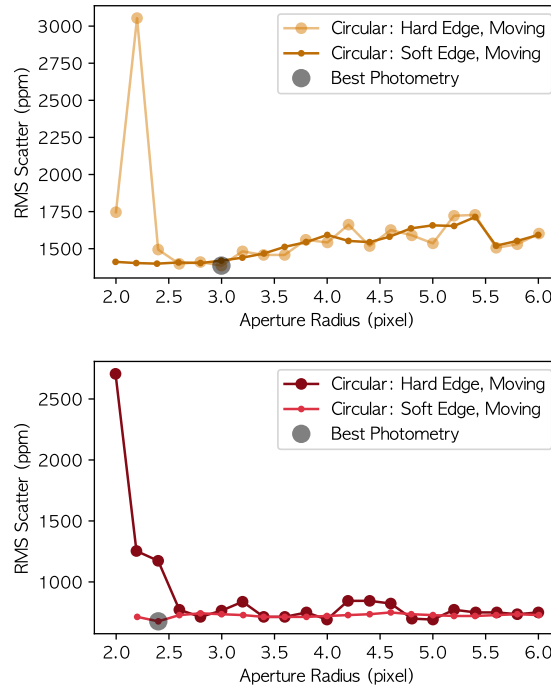


Figure 5.2: The top and bottom panels show the root-mean-squared (RMS) scatter for various photometry schemes performed on $3.6 \mu\text{m}$ and $4.5 \mu\text{m}$ data, respectively. The schemes resulting in the smallest RMS scatter are hard-edge circular apertures with a radius of 3.0 pixels for the $3.6 \mu\text{m}$ observations and a soft-edge aperture of 2.4 pixel for the $4.5 \mu\text{m}$ observations; these are denoted by a gray circle in each panel.

with a radius of 3.0 and soft-edge apertures with a radius 2.4 pixels for the $3.6 \mu\text{m}$ and $4.5 \mu\text{m}$ channels, respectively. The raw photometry and PSF metrics are presented in Figure 5.3.

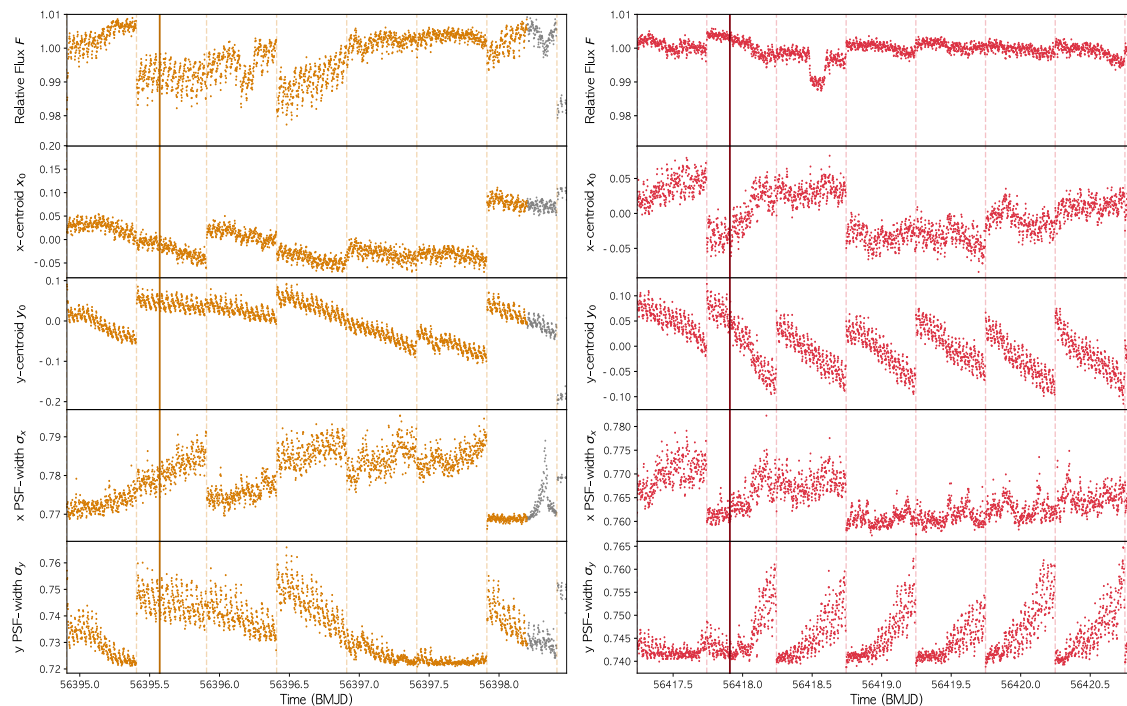


Figure 5.3: Raw photometry at $3.6 \mu\text{m}$ (left) and $4.5 \mu\text{m}$ (right). The top panel shows photometry using the preferred extraction scheme. The second and third panels show the x and y centroid coordinates, respectively. The fourth and fifth panels show PSF width along the x and y axes, respectively. The colored data points represent those used in the analysis while the gray points are discarded from the analysis. The vertical dark colored line represents the time of periastron passage. The vertical dashed lines represent the AOR breaks when the pointing of the spacecraft is readjusted. Note that the data were binned by 64-frame data cube for better visualization.

Pixel Level Decorrelation Photometry

Pixel Level Decorrelation (PLD) models the systematics as a function of the fractional flux measured by each pixel within a stamp (Deming et al. 2015). SPCA’s PLD photometry routine takes a 3×3 or 5×5 pixel stamp centered on the pixel position (15, 15). The cleaning routine applied to each pixel lightcurve is described in Bell et al. (2021).

5.2.3 PSF Diagnostics

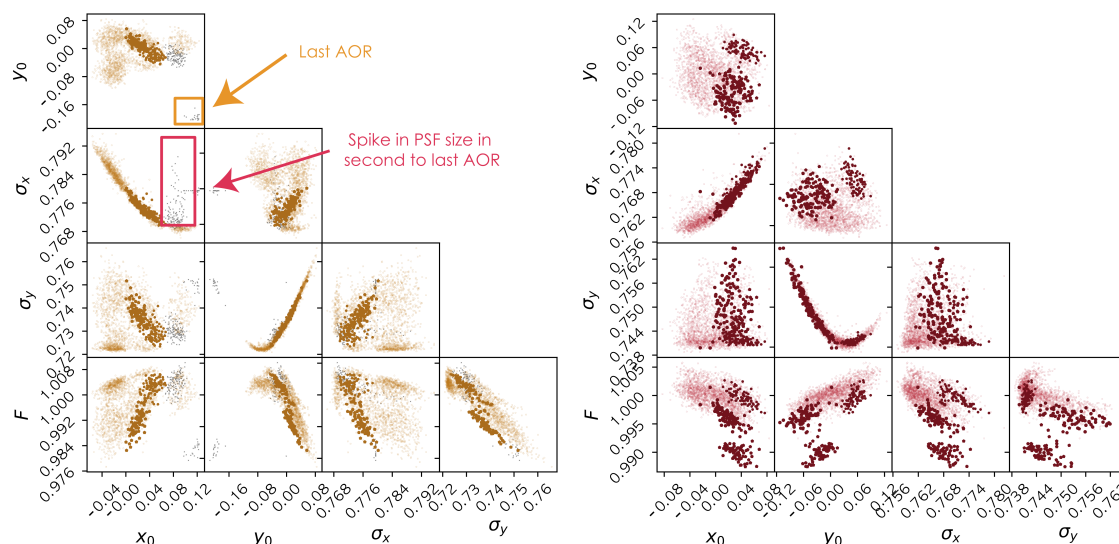


Figure 5.4: PSF metrics for the $3.6 \mu\text{m}$ (left) and the $4.5 \mu\text{m}$ (right) observations. Each point represent the median of a datacube. The grey dots in the $3.6 \mu\text{m}$ plot represent data that were discarded from our analysis due to deviant PSF centroids or widths. The darker points represent the in-eclipse and in-transit points data.

As noted by [Lanotte et al. \(2014\)](#) and [Challener et al. \(2021\)](#), sharp fluctuations in the PSF width can alter the photometry. We search for anomalous PSF behavior by exploring the correlation between the PSF centroids and width shown in Figure 5.4. Inspecting the PSF centroids for the $3.6 \mu\text{m}$ data, we find 2 distinct centroid clusters: a large cluster containing most of the data and a smaller cluster which corresponds to the centroid of the last AOR. Unfortunately, it is difficult to constrain the instrumental systematics of the smaller cluster due to the sparse data covering the area. We therefore elect to discard the last AOR of $3.6 \mu\text{m}$ observations.

As seen in Figure 5.4, for both channels, the PSF width follows a parabolic function of centroid. However, with closer inspection of the PSF size plotted against the centroid along the x-direction of the $3.6 \mu\text{m}$ data, there is a significant deviation from the parabolic trend marked in gray. These deviant points corresponds to the greyed out points in the second to last AOR in Figure 5.3. Note that this spike in PSF size coincides with a v-shape in the photometry and occurs during a secondary eclipse. The flux decrement is still seen using a larger aperture, which rules out the hypothesis that the inflated PSF causes some of the flux to fall outside the aperture. This detector systematic therefore remains unexplained but is presumably electronic in origin. We incorporate the PSF size into our detector sensitivity model as explained

in Section 5.3, but we were still unable to completely model out the instrumental signal. Upon analyzing the 2010 partial phase curve, we find that the spike feature led to an over-estimation of the eclipse depth. For this reason, we opt to discard these deviant points from our analysis.

Additionally, we elect to discard the first AOR from each phase curves containing 12 datacubes since the target was placed on a different pixel than the rest of the dataset for calibration purposes. After data reduction, a total of 2191 datacubes and 2388 datacubes are kept for analysis for the 3.6 μm and 4.5 μm channels, respectively. The products of our photometry extraction are shown in Figure 5.3 and 5.4. We then bin each dataset by datacube (64 frames) to reduce the computational cost of fitting the data with our many different decorrelation models.

5.3 Model

SPCA models the photometry as the product of the astrophysical model, $A(t)$, and the detector response, D : $F_{\text{total}} = A(t) \times D$. Both models are evaluated simultaneously. We experiment with astrophysical models of varying complexity and with different parametric and non-parametric detector response models, as described below. This experiment results in a statistical analysis to determine which combination of astrophysical and detector model is preferred by the data.

5.3.1 Astrophysical Model

The stellar flux is assumed to be constant except during transit. The shape of the transit is modeled using `batman` (Kreidberg 2015) with quadratic limb darkening. We modeled the astrophysical signal $A(t)$ as the sum of the stellar flux, $F_{\star}(t)$, and the planetary flux, $F_p(t)$:

$$A(t) = F_{\star}(t) + F_p(t). \quad (\text{S1})$$

The planetary flux, $F_p = E(t) \times \Phi(t)$, is modeled as a sinusoidal phase variation multiplied by the secondary eclipse, $E(t)$, modeled assuming a uniform disk using `batman` (Kreidberg 2015). We did not account for the light travel time as it is only 45.02 seconds at superior conjunction and does not affect our analysis. The phase variation is modeled as a second order sinusoidal function, Φ , and is expressed following (Lewis et al. 2013):

$$\begin{aligned} \Phi(\theta) = & 1 + A[\cos(\theta) - 1] + B \sin(\theta) \\ & + C[\cos(2\theta) - 1] + D \sin(2\theta), \end{aligned} \quad (\text{S2})$$

where $\theta = f + \omega + \pi/2$ is the orbital phase measured from mid-eclipse and f and ω are the true anomaly and the argument of periastron, respectively. We also experiment with a first-order sinusoid with C and D set to 0 to determine the degree of complexity statistically preferred. The phase variation function is scaled such that it is 0 during secondary eclipse and $E(t) = F_p/F_*$ outside of occultation, where F_p/F_* is the eclipse depth in terms of stellar flux. This parameterization allows for eclipse depth to be an explicit fit parameter. Despite its simple sinusoidal appearance, this parameterization captures the basic behaviour of more sophisticated simulations: rapid changes in flux near periastron when the planet’s orbital phase and temperature both vary quickly, and slower flux evolution near apoastron.

5.3.2 Detector Model

The *Spitzer*/IRAC 3.6 μm and 4.5 μm channels exhibit significant intrapixel sensitivity variations: for a given astrophysical flux, the electron count varies with the location and spread of the target’s PSF on the detector (Charbonneau et al. 2005; Lanotte et al. 2014). Over the years, several decorrelation techniques have been developed to achieve an exquisite level of precision (e.g., Ingalls et al. 2016). We tested several of these methods, namely 2D polynomials, BiLinear Interpolated Sub-pixel Sensitivity (BLISS) mapping, and Pixel Level Decorrelation (PLD). We briefly describe these methods below.

2D Polynomial Model

The 2D polynomial model uses the PSF centroids as regressors and polynomial coefficients are fit parameters (Charbonneau et al. 2005; Cowan et al. 2012a). We experiment with second order to fifth order polynomials, including all cross terms.

BLISS Mapping

We also experiment with BLISS mapping, first proposed by Stevenson et al. (2012). In summary, BLISS mapping is a data-driven iterative process to interpolate an intrapixel sensitivity map of the central pixel, which will in turn be used to decorrelate the data. The area over which the PSF centroids are distributed is divided into subpixels, also called “knots”, and each datum is associated with a knot. The data–astrophysical residuals are used to estimate the sensitivity of each knot and the sensitivity of each location of the detector is then estimated by bilinearly interpolating between the surrounding knots. We note that BLISS performs best with continuous uninterrupted

Spitzer observations. Since our observation scheme included more AOR breaks than most hot Jupiter phase curves, it may not be the best-suited dataset for this decorrelation method.

Pixel-Level Decorrelation

In contrast with BLISS mapping and polynomials, Pixel Level Decorrelation (Deming et al. 2015; Luger et al. 2018) does not explicitly depend on the PSF centroids. Rather, this method uses the fractional flux measured by each pixel to model the detector systematics. In principle, astrophysical flux variations would change the intensities of all the pixels in the stamp that encompasses the target’s PSF; however, they would not change the fractional fluxes of these pixels in the absence of detector systematics (e.g., spacecraft drift, thermal fluctuation). We experiment with 3×3 and 5×5 pixel stamps to explore the trade-off between capturing more stellar flux and more background flux. We test fits using a linear PLD and a second-order PLD that does not include cross-terms as they don’t improve the quality of the fit (Zhang et al. 2018).

PSF Width

Previous studies have shown that detector models including a function of the PSF width in x and y dramatically improve the photometric residuals (Knutson et al. 2012; Lewis et al. 2013). Mansfield et al. (2020) and Challener et al. (2021) experimented with linear, quadratic, and cubic dependencies on the PRF width in both the x and y directions and find the linear model to be preferred. Hence, we include the function of PSF width, $D_{\text{PSFW}}(\sigma_{x_0}, \sigma_{y_0})$, as a multiplicative term to the detector models listed above:

$$D_{\text{PSFW}}(\sigma_{x_0}, \sigma_{y_0}) = d_0 + d_1\sigma_{x_0} + d_2\sigma_{y_0} \quad (\text{S3})$$

where d_i are the fit parameters. We indeed find that including a PSF shape dependent model significantly reduces the red noise in the residuals when decorrelating data from both *Spitzer*/IRAC channels.

Step Function

For the $4.5 \mu\text{m}$ data, we could not get a good fit using any combination of the above detector models: the residuals showed a discontinuity between the first 2 AORs and the following 5 AORs. Often AOR discontinuities can be addressed by also fitting

for a linear trend (e.g. [Bell et al. 2019](#)), however, an unmodeled linear trend would exhibit a discontinuity at all the AOR breaks, which isn't the case here. To mitigate the problem, we added an additional detector sensitivity model as a multiplicative term:

$$D_{step} = h_1[H(t - h_2)] + 1, \quad (\text{S4})$$

where $H(t)$ is a Heaviside step function, h_1 is the amplitude of the DC offset, which we set as a fit parameter and h_2 is the time of the discontinuity which we fixed to the break between the 2nd and 3rd AOR. Our phase curve also includes 2 eclipses observations on either sides of the step to help constrain its magnitude.

5.4 Parameter Estimation and Model Comparison

We use the Affine Invariant Markov Chain Monte Carlo (MCMC) Ensemble Sampler from the `emcee` package to estimate the parameters and their respective uncertainties ([Foreman-Mackey et al. 2013](#)). We elect to fix the orbital period, P , the semi-major axis, a , the inclination, i , the eccentricity, e , and the argument of periastron, ω , to the values reported by [Wong et al. \(2014\)](#). We opt to fix the values rather than to impose a Gaussian prior on these parameters to significantly improve the analysis runtime. Although using fixed values instead of distributions can lead to an underestimation of the other model parameter uncertainties, the published uncertainties on the fixed parameters represent less than 0.1% of the reported value and therefore their contribution is negligible.

We initialize the astrophysical parameters to be the values reported by [Wong et al. \(2014\)](#). We begin an initial stage of parameter optimization as described in [Bell et al. \(2021\)](#). We require that transit depths and eclipse depths be between zero and unity. We use the parametrization of [Kipping \(2013\)](#) for the limb-darkening coefficients to ensure that our walkers only explore physically plausible solutions with uniform uninformative sampling.

By default, our pipeline includes a prior rejecting all models with phase variation coefficient that yield negative phase curves ([Keating & Cowan 2017](#)). Since an eccentric planet like XO-3b is subject to eccentricity seasons and is expected to have a time-variable atmosphere, we cannot map the planet following [Cowan & Agol \(2008\)](#) and hence cannot apply the more stringent constraint that the implied planetary map is non-negative ([Keating & Cowan 2017](#); [Keating et al. 2019](#)). Nonetheless, our ability to fit the phase variations with an energy balance model in § 5.5.2 demonstrates that they do not require regions with negative flux. In any case, due to the deep eclipse depths, the fraction of rejected phase curves is less than 0.0001%.

Table 5.1: Best-fit Model Parameter Estimates ^a

Name	Symbol	Prior	Reference	3.6 μm	4.5 μm
Fitted					
Time of transit (BJD)	t_0	–	–	$56418.5434^{+0.0004}_{-0.0005}$	56418.5421 ± 0.0002
Radius of planet	R_p/R_*	[0,1]	–	$0.0866^{+0.0014}_{-0.0012}$	0.0891 ± 0.0008
Eclipse depth (ppm)	F_p/F_*	[0,1]	–	1770 ± 180	1610 ± 70
Limb Darkening coeff.	q_1	[0,1]	–	$0.05^{+0.06}_{-0.05}$	$0.05^{+0.03}_{-0.02}$
Limb Darkening coeff.	q_2	[0,1]	–	$0.2^{+0.6}_{-0.4}$	$0.8^{+0.3}_{-0.4}$
Phase var. coeff (order 1)	A	–	–	0.21 ± 0.04	0.34 ± 0.02
Phase var. coeff (order 1)	B	–	–	-0.01 ± 0.04	$-0.08^{+0.02}_{-0.03}$
Phase var. coeff (order 2)	C	–	–	–	0.05 ± 0.02
Phase var. coeff (order 2)	D	–	–	–	$0.07^{+0.01}_{-0.02}$
Fitted					
Period (days)	P	$3.19153285 \pm 0.000000058$	Wong et al. (2014)	–	–
Semi-major axis	a/R_*	$7.052^{+0.076}_{-0.097}$	Wong et al. (2014)	–	–
Inclination	i	84.11 ± 0.16	Wong et al. (2014)	–	–
Eccentricity	e	$0.2769^{+0.0017}_{-0.0016}$	Wong et al. (2014)	–	–
Longitude of periaapse	ω	$347.2^{+1.7}_{-1.6}$	Wong et al. (2014)	–	–
Derived					
Periastron passage after transit (days)	–	2.5645	–	–	–
Phase curve peak after transit (days)	–	–	–	2.11 ± 0.09	2.17 ± 0.03
Phase curve trough after transit (days)	–	–	–	-0.04 ± 0.10	-0.27 ± 0.04
Phase curve peak after eclipse (hrs)	–	–	–	-0.53 ± 1.98	0.95 ± 0.82

^aThe uncertainties for the fitted parameters to the 3.6 μm data have been inflated by a factor of 1.72 to account for the correlated noise in the residuals (Fig. 5.6).

We make the photometric uncertainty, σ_F , a fitted parameter and use `emcee` to estimate the set of parameters that maximizes the log-likelihood:

$$\ln(L) = -\frac{1}{2}\chi^2 - N_{\text{dat}} \ln \sigma_F - \frac{N_{\text{dat}}}{2} \ln(2\pi), \quad (\text{S5})$$

where N_{dat} is the number of data. The badness-of-fit is defined as

$$\chi^2 = \frac{\sum_i^{N_{\text{dat}}} [F_i - F_{i,\text{model}}]^2}{\sigma_F^2}, \quad (\text{S6})$$

where F_i are brightness measurements and $F_{i,\text{model}}$ are the predicted brightness from the astrophysical model described in section 5.3.

We initialize 300 MCMC walkers as a Gaussian ball distributed tightly around our initial guess. We perform an initial burn-in to let the walkers explore a wide region in parameter space during which each walker performs 5000 steps. We then perform a 1000 steps production run while making sure we meet our convergence criteria: 1) the log-likelihood of the best walker does not change over last 1000 steps of the MCMC chain and 2) the distribution of walkers is constant over the last 1000 steps along each parameter. We then obtain a posterior distribution and estimate the 1σ confidence region as the 16th to 84th percentile of the posterior distribution of each parameter using all the walkers over the last 1000 MCMC steps.

5.4.1 Model Comparison

As mentioned previously, we experiment with various astrophysical and detector response models. Generally, when the number of fit parameters increase, the fit to the data also improves since the model becomes more flexible. Instead of comparing the badness-of-fit or log-likelihood of the best-fit obtained by each model, we therefore compare the Bayesian Information Criterion (BIC; Schwarz et al. 1978) of the different models:

$$BIC = N_{\text{par}} \ln N_{\text{dat}} - 2 \ln L, \quad (\text{S7})$$

where N_{par} is the number of fit parameters. By definition, a smaller BIC is preferred. A comprehensive model comparison can be found in Figure 5.7 which shows the shape of the astrophysical phase variation for each model fit and their relative BIC. In principle, the more fit parameters a model has, the more flexible it is and the better goodness-of-fit it achieves. The BIC allows us to justify or rule out having a more complex model with more fit parameters. We note that BLISS does not have any explicit fit parameters, instead we use the number of BLISS knots as number of parameters to estimate its BIC. This could explain why BLISS seems to exhibit

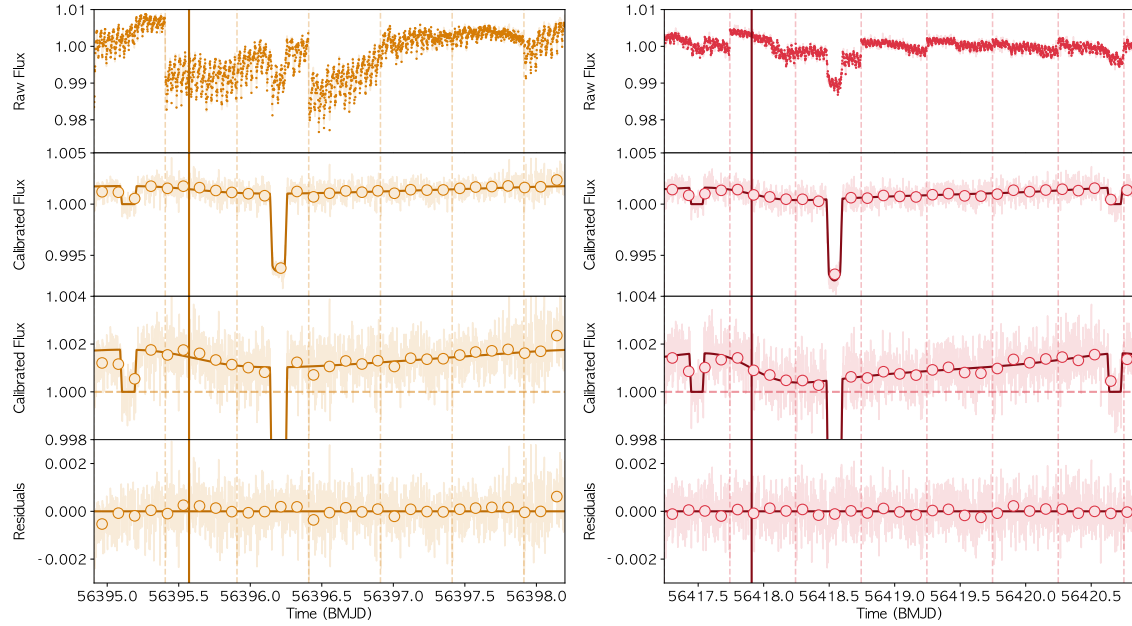


Figure 5.5: The best-fit models to the $3.6 \mu\text{m}$ and $4.5 \mu\text{m}$ observations are presented in the left and right panels, respectively. The vertical dashed lines represent the AOR breaks and the dark vertical lines represent the time of periapse passage. The raw photometry is plotted in the top panels in pale yellow and red while the best-fit signal, F_{total} , is shown in dark yellow and red. The corrected photometry is shown in the second panels in pale yellow and red and the best-fit astrophysical models are shown in darker colors. The third panels are a zoomed-in version of the second panels to more clearly show the phase variations. The last panels shows the residuals. Note that the $3.6 \mu\text{m}$ and $4.5 \mu\text{m}$ channels data were fitted independently.

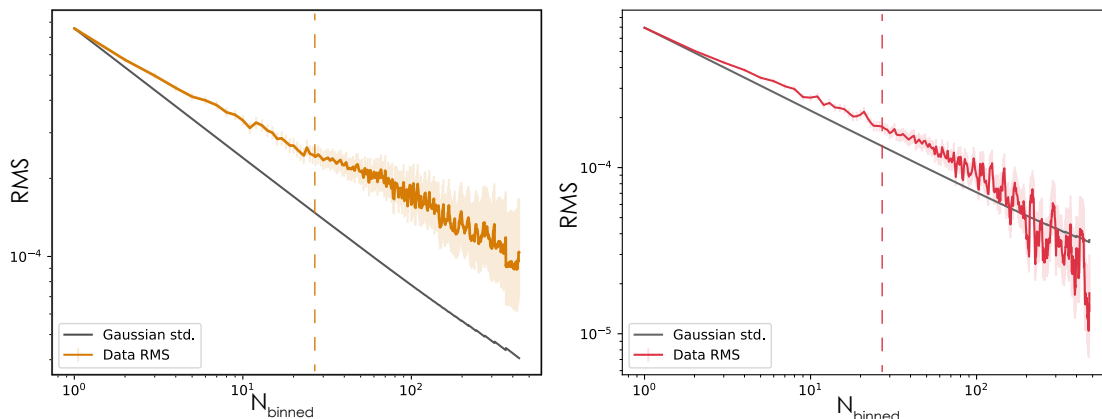


Figure 5.6: Red-noise test for our best-fit models as a function of bin size for $3.6 \mu\text{m}$ (left) and $4.5 \mu\text{m}$ (right) fit. We binned the data into bins of different size, N_{binned} , and computed the binned residuals RMS. The lighter shaded area is the uncertainty that the MC3 package computed (Cubillos et al. 2017). The grey line represents the expected decrease in RMS if the residuals are purely white noise. We find that there is significant red noise in the residuals of the $3.6 \mu\text{m}$ fit, while the residuals of the $4.5 \mu\text{m}$ fit are less correlated. The vertical dashed line represents the number of bins contained in the duration of an eclipse depth.

systematically worst BIC than the other decorrelation methods (Figure 5.2), however, we note that the BLISS phase curves also have systematically different amplitudes and shapes than that of the phase curves retrieved using different decorrelation methods.

5.5 Results

5.5.1 SPCA Fits

As shown in Figure 5.7, for our $3.6 \mu\text{m}$ phase observations, the first-order PLD model using a 5×5 pixels stamp and a first-order sinusoidal phase curve was the preferred model. For our $4.5 \mu\text{m}$ observations, the preferred solution is a first-order PLD model using a 3×3 pixels stamp and a second-order sinusoidal phase curve. Both preferred fits are shown in detail in Figure 5.5. We note that the $3.6 \mu\text{m}$ fit leaves noisier residuals than the $4.5 \mu\text{m}$. Figure 5.6 shows a red-noise test performed on the residuals of the $3.6 \mu\text{m}$ and $4.5 \mu\text{m}$ fits. The black line on both plots represent the expected decrease in root-mean-squared (RMS) scatter when uncorrelated data are binned. While the $4.5 \mu\text{m}$ RMS is in good agreement with this line, the larger than expected RMS of the $3.6 \mu\text{m}$ channel is indicative of leftover detector or astrophysical

CHAPTER 5. THERMAL PHASE VARIATIONS OF XO-3B

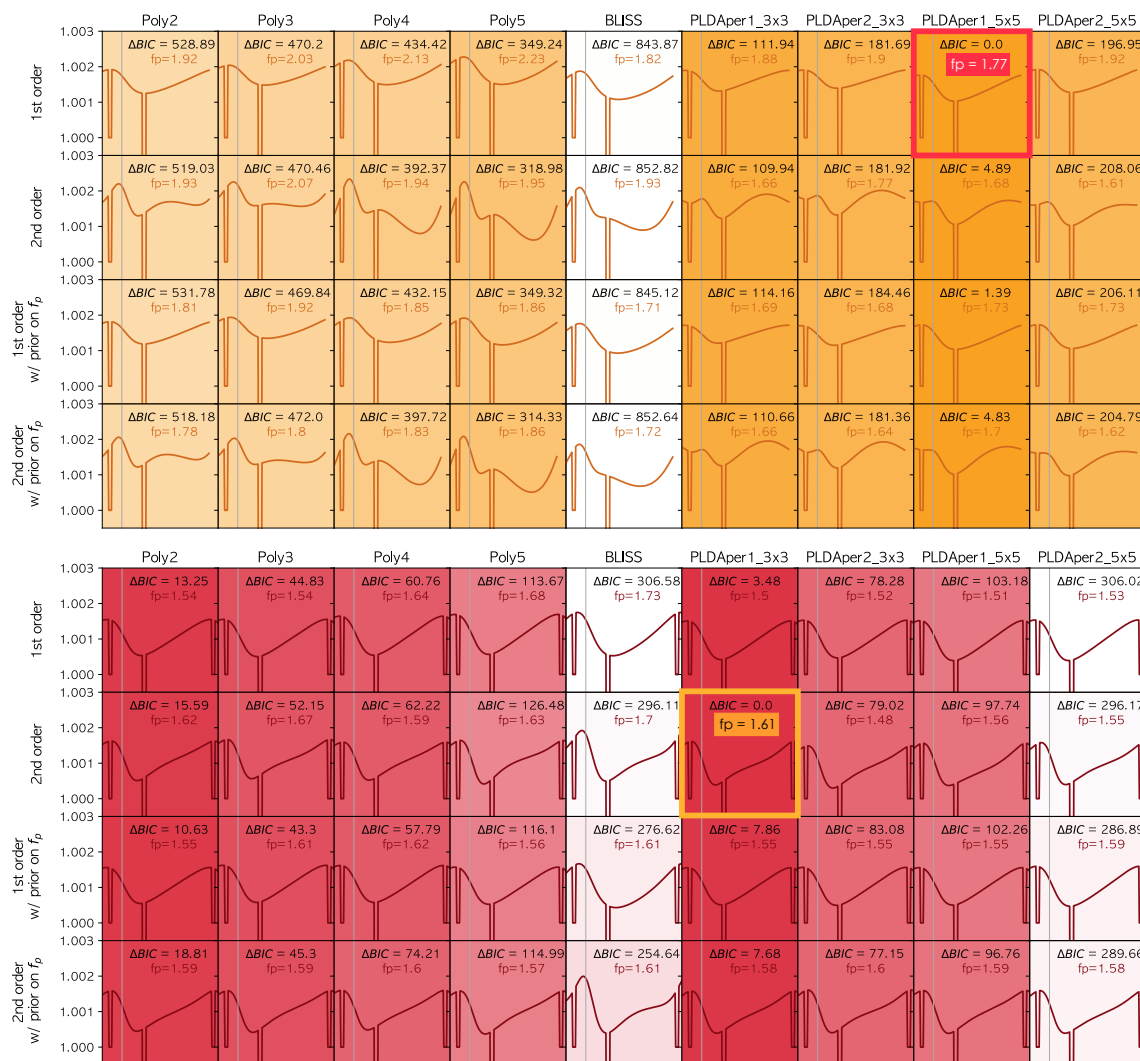


Figure 5.7: Model comparisons for Spitzer $3.6 \mu\text{m}$ (top) and $4.5 \mu\text{m}$ (bottom) phase variations of XO-3b. The best-fit astrophysical model to the *Spitzer* data obtained using different detector models and phase variation models are shown here. Each column indicates the detector model used. The rows indicate the phase variation model used and whether or not a prior was imposed on the secondary eclipse depth. The ΔBIC from the preferred solution of each fit are indicated in each box and the opacity of the background of each box reflects fit preference (darker is better). The eclipse depth for each fit is denoted by f_p , in parts-per-mille. *Top:* The fit using a first-order PLD with a 5×5 stamp using a first-order sinusoidal model is preferred. In principle, the shape of the best-fit phase curve is dependent on the models and priors chosen. Fortunately, the shape of the first-order phase variation model is robust against the choice of detector model and prior on the secondary eclipse depth. *Bottom:* The preferred fit uses a first-order PLD with a 3×3 stamp and a second-order sinusoidal model. Note that the shape of the $4.5 \mu\text{m}$ phase curves is robust against prior and model choices, but the $3.6 \mu\text{m}$ phase curve shape is not.

variations that our model could not fit.

The best-fit astrophysical parameters for the *Spitzer* observations are presented in Table 5.1. We find a ratio of planet to star radius of $R_p/R_* = 0.0866^{+0.0014}_{-0.0012}$ and 0.0891 ± 0.0008 with the 3.6 μm and 4.5 μm observations, respectively. We measure secondary eclipse depths of 1770 ± 180 ppm and 1610 ± 70 ppm at 3.6 μm and 4.5 μm , respectively. The 4.5 μm eclipse depth is within 1σ of that reported by Wong et al. (2015) and Ingalls et al. (2016). While both phase curves were analyzed independently of each other, their shapes are similar (Figure 5.8). The 3.6 μm and 4.5 μm phase curves peak 2.11 ± 0.09 and 2.17 ± 0.03 days after transit, respectively. The minimum of the phase curves occur 0.04 ± 0.10 and 0.27 ± 0.04 days before transit. We also note that the 3.6 μm and 4.5 μm best-fit transit time differs by $\Delta t_0 = 0.0013 \pm 0.0005$ days. This less than 3σ discrepancy is about the temporal resolution of our phase curve, hence the difference in the 3.6 and 4.5 μm t_0 isn't meaningful.

5.5.2 Energy Balance Model

To extract radiative and advective properties of the atmosphere of XO-3b, we use the `Bell_EBM` semi-analytical energy balance model (EBM) to fit our detrended phase variations (Bell & Cowan 2018). As the atmospheric temperature does not exceed 2500 K, we did not include the effect of recombination and dissociation of hydrogen. The model treats the advection of atmospheric gas via solid body rotation at angular velocity ω_{wind} , assumes a uniform Bond albedo, A_B , and a uniform atmospheric pressure, P_0 , at the bottom of the mixed layer (the part of the atmosphere that responds to diurnal and seasonal forcing). These quantities are treated as fit parameters and remain constant throughout the orbit. Depending on the efficiency of turbulent mixing (Youdin & Mitchell 2010; Bordwell et al. 2018) and varying barotropic large-scale flows vertical thickness, P_0 could be deeper in the atmosphere than the pressure at which incoming optical light is absorbed.

Given the significant correlation in the 3.6 μm residuals and that different wavelengths probe different photospheres (Dobbs-Dixon & Cowan 2017), we opt to evaluate each phase curve separately. The energy balance model is fit to the phase curves using the MCMC package `emcee` (Foreman-Mackey et al. 2013). Again, we decide to fix the orbital period, P , the semi-major axis, a , the inclination, i , the eccentricity, e , and the argument of periastron, ω , with values reported in Table 5.2. We use the stellar effective temperature from *Gaia* DR2 (Gaia Collaboration et al. 2018) as well as the updated radius and mass of XO-3 based on *Gaia* DR2 parallaxes (Stassun et al. 2017, Stassun et al. in prep).

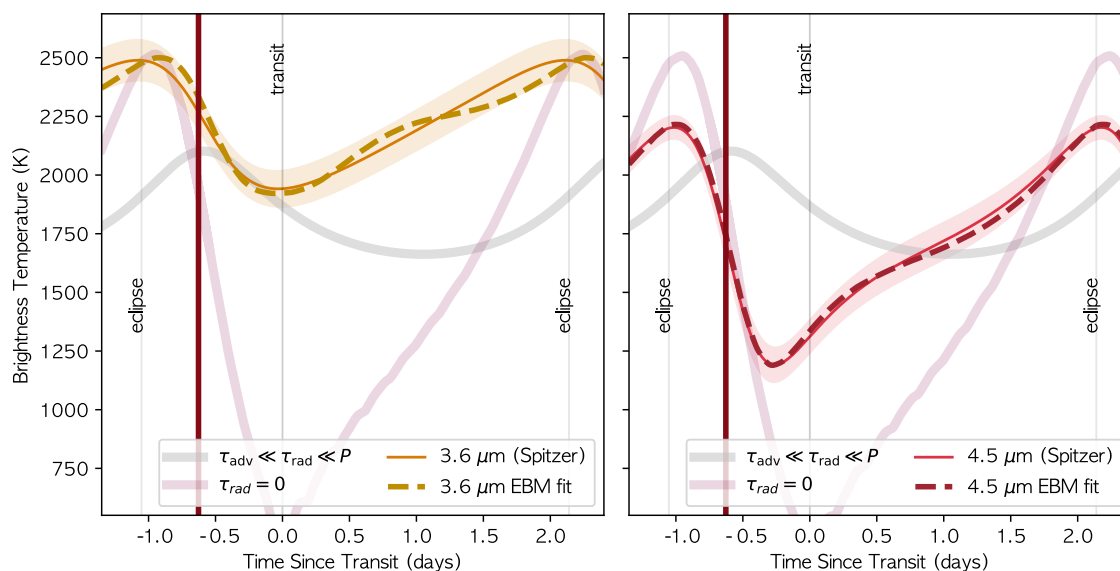


Figure 5.8: The yellow (*left*) and red (*right*) line and swath represent the brightness temperature and uncertainties of XO-3b based on the *Spitzer* 3.6 μm and 4.5 μm observations, respectively. The dark yellow and red dashed lines represent the energy balance model fits to the temperature curves. The light grey lines represent the time of secondary eclipse and the dark grey line indicates the transit time. The vertical brown line represents the periastron passage. In both panels, the grey transparent curve represent the limiting case with a short advective timescale $\tau_{adv} \ll \tau_{rad} \ll P$ and the pink transparent line represents the limiting case of a short radiative timescale, $\tau_{rad} = 0$.

Table 5.2: Energy Balance Model Fit

Parameter	Prior	Reference	3.6 μm	4.5 μm
Fitted				
P_0 (bar)	$[10^{-3}, 20]$	–	$0.15^{+0.21}_{-0.11}$	$2.40^{+0.92}_{-0.16}$
Equatorial Wind Speed, V_{wind} , (km/s)	–	–	$12.1^{+3.0}_{-4.4}$	$3.13^{+0.26}_{-0.83}$
Internal Energy, E_{int} , (W/m^2)	$[0, +\infty]$	–	$(7.21^{+0.11}_{-0.17}) \times 10^5$	$(1.6^{+11.8}_{-27.0}) \times 10^2$
Albedo, A_B	$[0, 1]$	–	0.0	$0.106^{+0.008}_{-0.106}$
Fitted				
Period, P , (days)	$3.19153285 \pm 0.000000058$	Wong et al. (2014)	–	–
Eccentricity, e	$0.2769^{+0.0017}_{-0.0016}$	Wong et al. (2014)	–	–
Semi-major axis, a , (AU)	$0.04589^{+0.0063}_{-0.0049}$	Wong et al. (2014)	–	–
Planet Radius, R_p , (R_{Jup})	1.295 ± 0.066	this work	–	–
Planet Mass, M_p , (M_{Jup})	11.79 ± 0.98	this work	–	–
Inclination, i , (deg)	84.11 ± 0.16	Wong et al. (2014)	–	–
Longitude of periapee, ω	$347.2^{+1.7}_{-1.6}$	Wong et al. (2014)	–	–
Pseudo-Synchronous Rotation Period, P_{ps} (days)	2.170	Hut (1981) prescription	–	–
Stellar Effective Temperature, T_{eff} , (K)	6759 ± 79	Soubiran et al. 2020	–	–
Stellar Radius, R_* , (R_{\odot})	1.407 ± 0.038	this work	–	–
Stellar Mass, M_* , (M_{\odot})	1.21 ± 0.15	this work	–	–
Derived				
Average Radiative Timescale, $\tau_{\text{rad,ave}}$, (hrs)	–	–	~ 6	~ 30
Advective Timescale, τ_{adv} , (hrs)	–	–	~ 0.1	~ 1

The `Bell_EBM` is agnostic about the underlying rotation of XO-3b, since its atmosphere is not expected to remain stationary with respect to the deeper regions. Nonetheless, in order to convert the inertial-frame atmospheric angular frequency, ω_{atm} , to a zonal wind velocity, we must assume a rotational frequency for the interior of the planet. The interiors of short-period eccentric planets are expected to be pseudo-synchronously rotating. Roughly speaking, this means that the planet is momentarily tidally locked near periastron passage, when the tidal forces are strongest. We adopt the prescription of Hut (1981) for the pseudo-synchronous rotation frequency, $\omega_{ps} \simeq 0.8\omega_{\text{max}}$, where the maximum orbital angular velocity at periastron is (Cowan & Agol 2011a):

$$\omega_{\text{max}} = \frac{2\pi (1 + e)^{1/2}}{P (1 - e)^{3/2}}. \quad (\text{S8})$$

The equatorial wind velocity is therefore

$$v_{\text{wind}} \simeq (\omega_{\text{atm}} - \omega_{ps}) R_p. \quad (\text{S9})$$

We transform the *Spitzer* phase curve into an orbital apparent brightness temperature profile and fit it with our energy balance model. Physically motivated uniform priors are imposed to the fit parameters (see Table 5.2). Our initial attempts to fit the 3.6 μm *Spitzer* phase-dependent temperatures with the `Bell_EBM` could not reproduce the high brightness temperatures at all orbital phases. Due to the eccentricity of XO-3b’s orbit, the planet is expected to experience tidal heating. We therefore add an internal energy source flux term, E_{int} , to equation (1) of Bell & Cowan (2018) and fit for this extra parameter. We experiment with and without this term and find that models allowing for an internal energy source are preferred. The best-fit EBM models to each channel are presented in Table 5.2 and Figure 5.8. For comparison, we also show the temperature curve of a limiting case with a very short advective timescale $\tau_{\text{adv}} \ll \tau_{\text{rad}} \ll P$, such that the incident energy is uniformly redistributed instantaneously (the advection-dominated phase curve). We also show the special case where $\tau_{\text{rad}} = 0$, i.e., the radiation-dominated phase curve. Neither of these limiting cases account for the presence of an internal energy source.

4.5 EBM Fit

The energy balance model is able to reproduce the timing and amplitude of the 4.5 μm phase curve peak and the minimum is only 1σ from the *Spitzer* observations. The best-fit model has v_{wind} of $3.13_{-0.83}^{+0.26}$ km/s: approximately the speed of sound. The model suggests that the mixed layer extends down to $P_0 = 2.40_{-0.16}^{+0.09}$ bar and a Bond albedo $A_b = 0.106_{-0.106}^{+0.008}$. From these, we estimate an advective timescale of ~ 1 hour

and an average radiative timescale of ~ 30 hours. Unlike the $3.6 \mu\text{m}$ phase curve, we do not need internal heating to explain the $4.5 \mu\text{m}$ phase curve.

5.5.3 Spitzer/IRAC 3.6: A Cautionary Tale

Strong Detector Systematics

Spitzer/IRAC’s $3.6 \mu\text{m}$ channel is known to be less stable than the $4.5 \mu\text{m}$ channel: stronger detector systematics generally plague the $3.6 \mu\text{m}$ observations (e.g. Zhang et al. 2018). As discussed in Section 2.3, the $3.6 \mu\text{m}$ observations exhibit a sharp PSF fluctuation coinciding with one of the secondary eclipses. We experiment with and without excluding the anomalous observations and find an eclipse depth 2130 ± 110 ppm when the aberrant observations are included and 1770 ± 100 ppm when discarded. The deeper eclipse depth estimate is likely a result of the large decrease in flux caused by the sharp PSF width fluctuation, hence we elect to omit the anomalous portion of the observations for the analysis. Consequently, without a reliable second eclipse, it is significantly more difficult to distinguish astrophysical trends from detector systematics. Furthermore, Figure 5.6 indicates that the residuals from our best-fit model to XO-3b’s $3.6 \mu\text{m}$ phase curve are significantly correlated; on the eclipse duration timescale the $3.6 \mu\text{m}$ residual RMS is 1.72 times larger than expected if the residuals were uncorrelated. Hence, we elect to inflate our SPCA fit uncertainties by 1.72 for the $3.6 \mu\text{m}$ fit and the $3.6 \mu\text{m}$ observations should be interpreted with caution.

3.6 Secondary Eclipse Inconsistencies

While the many repeat observations of the $4.5 \mu\text{m}$ eclipse of XO-3b enable a precise and robust measurements (Wong et al. 2014), the planet has only been observed in $3.6 \mu\text{m}$ with *Spitzer* two other times: one secondary eclipse in 2009 (Machalek et al. 2010, PID 525) and an unpublished partial phase curve obtained in 2010 (PI: P. Machalek, PID 60058). Our 1770 ± 180 ppm eclipse depth is 5σ discrepant with the $3.6 \mu\text{m}$ eclipse depth of 1010 ± 40 ppm reported by Machalek et al. (2010) taken during the cryogenic era *Spitzer* data. Such significant discrepancies between cryogenic and warm *Spitzer* eclipse depths are not unheard of (Hansen et al. 2014), and we note that there is visible correlated noise in Machalek et al. (2010)’s $3.6 \mu\text{m}$ residuals, hence their eclipse uncertainty is likely underestimated.

We investigate the $3.6 \mu\text{m}$ eclipse depths inconsistencies by analyzing the partial phase curve. Unfortunately, the 2010 observations are difficult to detrend because they only cover half an orbit and have large AOR breaks. Nonetheless, we were able

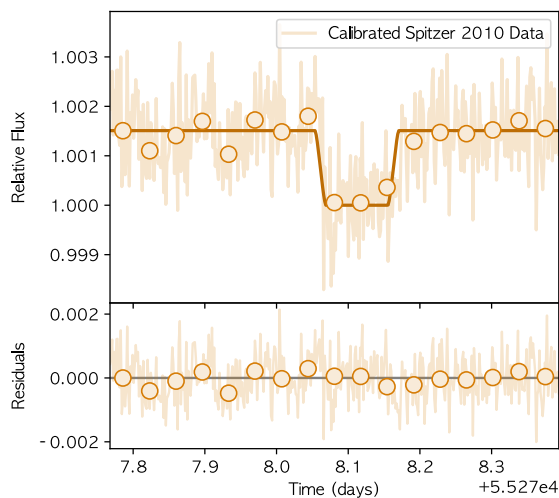


Figure 5.9: SPCA analysis of the secondary eclipse obtained as part of the 2010 partial phase curve of XO-3b at $3.6 \mu\text{m}$ with *Spitzer*. The detrended data are connected with a pale orange line. The dark line represents the best-fit astrophysical model and the orange circles represent the binned calibrated photometry in 20 bins. The bottom panel shows the residuals of the SPCA fit.

to fit the secondary eclipse portion of the 2010 time series, shown in Figure 5.9. We find an eclipse depth of 1520 ± 130 ppm, within 2σ our fit to the 2013 full-orbit phase curve.

[Machalek et al. \(2010\)](#)’s data were taken with a two-channel mode, i.e., two 2 s exposures at $3.6 \mu\text{m}$ for every 12 s exposure at $5.8 \mu\text{m}$ in order to avoid saturating in the shorter wavelength. As a result, the early eclipse has approximately 30% the efficiency of the continuous observation mode used for the later phase curves. Hence, we elect to discard [Machalek et al. \(2010\)](#)’s and the spoiled second eclipse in our full phase curve. When fitting the 2013 phase curve we experiment with using a Gaussian prior centered on the depth we obtained using the 2010 data. We find that the eclipse depth posteriors are consistent with or without the prior.

Tentative 3.6 EBM Fit

While the average $4.5 \mu\text{m}$ *Spitzer* temperature curve is consistent with the expected T_{eq} of XO-3b, the $3.6 \mu\text{m}$ temperature curve is higher and does not intersect with the $4.5 \mu\text{m}$ temperature curve at any point in the orbit. In fact, the $3.6 \mu\text{m}$ brightness temperature curve is comparable to the planet’s irradiation temperature, which means one of two scenarios: 1) a large excess flux or 2) leftover detector systematics. We

favour the second scenario—detector systematics—but explore the implications of the model fit below for completeness.

The best-fit model gives an unexpectedly high v_{wind} of $12.1_{-4.4}^{+3.0}$ km/s, an order of magnitude faster than the equatorial wind speed obtained for the $4.5 \mu\text{m}$ fit. Such a large equatorial wind speeds are in general not physically possible. As highlighted in Koll & Komacek (2018) although wind speeds approaching or even slightly exceeding the speed of sound (~ 2 km/s) are possible in hot Jupiters, the development of shocks and shear instabilities in the atmosphere will naturally limit the maximal wind speeds at the atmospheric pressures being probed by our observations of XO-3b. The fit suggests a mixed layer down to $P_0 = 0.15_{-0.11}^{+0.21}$ bar, a short advective timescale of 0.2 hours and an average radiative timescale of ~ 6 hours. An internal energy source flux of $7.21_{-0.17}^{+0.11} \times 10^5$ W/m² is required to fit the $3.6 \mu\text{m}$ brightness temperature. This internal flux is **1.3 times** the average incident stellar flux. If this is interpreted as tidal heating, it would require a tidal quality factor of $Q \sim 6 \times 10^3$. Given the above issue with the $3.6 \mu\text{m}$ data, these results should be taken lightly.

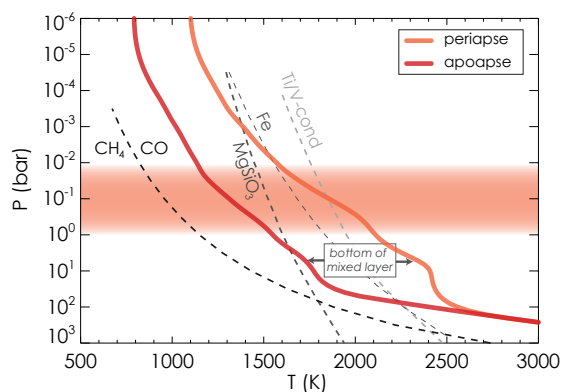


Figure 5.10: 1D atmospheric model at apoapse and periapse. The model predicts that incoming shortwave radiation from the star is deposited entirely at pressures $P < 10$ bars above the isothermal region. An approximate infrared photosphere is indicated by the red swath from 0.01 to 1 bar.

5.5.4 Theoretical Models of XO-3b’s Atmosphere

Vertical Thermal Structure

We present in Figure 5.10 a planet-averaged 1D model at apoapse and periapse to look at the deposition of stellar energy as a function of pressure (Marley et al. 2002;

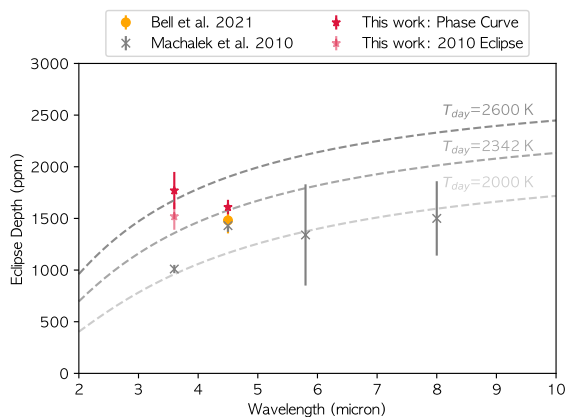


Figure 5.11: Published *Spitzer*/IRAC secondary eclipse depths are shown along with our new eclipse depths. Gray dashed lines show notional eclipse spectra if the star and planet radiate as blackbodies with $T_{\text{eff},*} = 6885$ K and planetary dayside temperature of $T_{\text{day}} = [2000, 2342, 2600]$ K. The deeper $3.6 \mu\text{m}$ eclipse depth in comparison to the $4.5 \mu\text{m}$ eclipse depth rules out the thermal inversion reported by Machalek et al. (2010): water vapour opacity dictates that the $3.6 \mu\text{m}$ photons originate from deeper in the atmosphere than those at $4.5 \mu\text{m}$.

Fortney et al. 2008). The model uses the code, physics, and chemistry described in Fortney et al. (2008). The specific entropy of the deep adiabat is relatively uncertain, here a value of the intrinsic flux (parameterized as T_{int}) was set to 300 K at periapse, which sets the adiabat for the self-consistent model in radiative-convective equilibrium. The temperatures in the deep part of the atmosphere are expected to be horizontally uniform. Therefore, the T_{int} value for apoapse was iterated until the converged apoapse model fell upon the same deep adiabat, yielding $T_{\text{int}}=520$ K. The planet’s temperature should be homogenized at depth, but, T_{int} can’t be thought of as constant in a simplified 1D modeling framework because the T-P profiles won’t lie on the same adiabat due to limitations of a 1D model. We note that a more sophisticated solution with time-stepping atmospheric structure code has been developed to investigate the continuous atmospheric response to the variable incident flux that eccentric planets experience (Mayorga et al. 2021) that uses a different approach by fixing T_{int} .

The 1D atmospheric model shown in Figure 5.10 predicts that incoming short-wave light from the star has all been absorbed by $P < 10$ bars. This is slightly deeper than the bottom of the mixed layer of $P_0 = 2.40^{+0.92}_{-0.16}$ bar inferred from our EBM fit to the $4.5 \mu\text{m}$ data. We note that mixed layer here is a relevant model quantity in terms of explaining heat transport at observable levels, but it might not be accurate to extrapolate its meaning to the full depth of the circulation. In reality, because

of the barotropic nature of the flow, winds will be strong throughout the observable atmosphere. A hotter interior would result in an adiabat at lower pressures and the isothermal region would take less room in pressure space. The infrared photosphere, on the other hand, is expected to be at the 0.01–1 bar altitude due to the atmosphere’s greater IR opacity. In reality, for strong narrow absorption lines, photons could be absorbed even down to 10^{-4} bars. We only expect winds to become significant at higher altitude than the deposition layer, where horizontal temperature gradients are greater; we therefore expect the mixed layer to lie above the shortwave deposition depth.

By comparing the simulated temperature-pressure profiles with condensation and molecular transition curves in Figure 5.10, we expect that CO is the main carbon carrier on the planet throughout its orbit. Clouds of TiO/VO, FeSiO₃ and MgSiO₃ might be expected to form at or above the IR photosphere when the planet is near periapse, but would be too deep to affect the emergent spectrum at apoapse. Hence the emergent spectrum of the planet near periapse—possibly including the secondary eclipse—could be affected by the presence of clouds above the notional clear-sky photosphere. There is no evidence of such clouds in the planet’s eclipse spectrum. The *Spitzer* eclipse depth measurements are shown in Figure 5.11: a deeper 3.6 μm eclipse depth disfavors the dayside thermal inversion reported by Machalek et al. (2010). Unfortunately, our analysis is inconclusive as to temperature inversions for the rest of the orbit due to systematics spoiling our 3.6 μm phase curve. Further investigations with JWST at different orbital phases could provide a better understanding of XO-3b’s atmospheric thermal structure and its response to the changing incident stellar flux.

3D General Circulation Model

We present three-dimensional atmospheric circulation models of XO-3b using the SPARC/MITgcm (Showman et al. 2009). The SPARC/MITgcm couples the MITgcm, a three-dimensional (3D) general circulation model (GCM) (GCM; Adcroft et al. 2004) with a two-stream adaptation of a multi-stream radiative transfer code Marley & McKay (1999). The MITgcm solves the primitive equations using the finite-volume method over a cubed sphere grid. The radiative transfer code solves the two-stream radiative transfer equations, and employs the correlated- k method to solve for upward/downward fluxes and heating/cooling rates through the atmosphere (e.g., Goody et al. 1989; Marley & McKay 1999). The correlated- k method retains most of the accuracy of full line-by-line calculations, while drastically increasing computational efficiency. The SPARC/MITgcm has been applied to a range of exoplanets

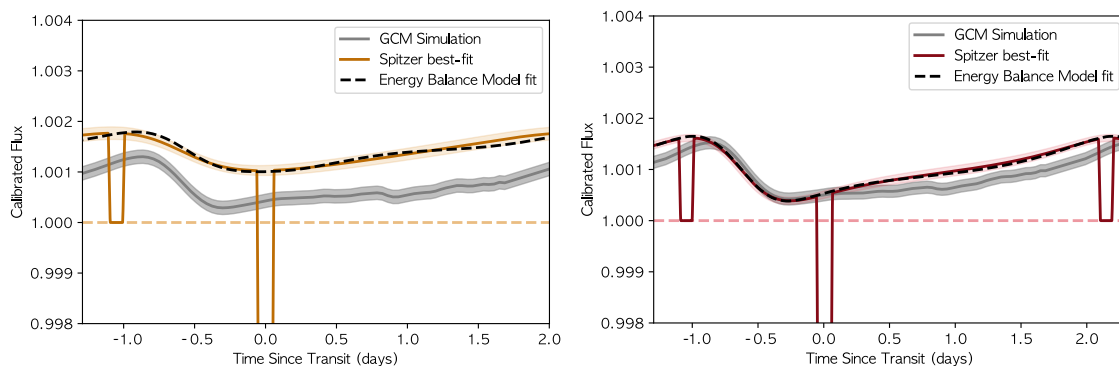


Figure 5.12: General circulation model (GCM) thermal phase curve predictions for the $3.6 \mu\text{m}$ (*left*) and $4.5 \mu\text{m}$ (*right*) Spitzer band passes. The coloured swath represent the 1σ uncertainties of the best-fit *Spitzer* phase curves. The grey swath represents the magnitude of the orbit-to-orbit variability seen in the GCM. The large discrepancy between the $3.6 \mu\text{m}$ *Spitzer* phase curve and GCM predictions is likely due to issues with the observations. At $4.5 \mu\text{m}$, our model correctly predicts the cooling rate of the planet between eclipse and transit, but underestimates its heating rate between transit and eclipse. The dashed black lines represents the EBM fit to each Spitzer phase curve.

and brown dwarfs (e.g., [Showman et al. 2009](#); [Kataria et al. 2014](#); [Lewis et al. 2014](#); [Parmentier et al. 2018](#); [Steinrueck et al. 2019](#)).

In this model we adopt a horizontal resolution of 32×64 in latitude and longitude, and a vertical resolution of 40 layers evenly spaced in log pressure from 200 bars at the bottom boundary to 200 microbars at the top. Given that XO-3b is on an eccentric orbit, we assume the planet is “pseudo-synchronously” rotating, i.e., that the planet’s tidal interactions with the star force a single side of the planet to approximately face the star every periape passage. We estimate the planet’s rotation rate following the [Hut \(1981\)](#) formulation for binary stars, $T_{\text{rot}} = 1.852 \times 10^5$ seconds (or approximately 2 days). We assume a Solar atmospheric composition without TiO/VO (whose opacities are used to produce a thermal inversion). Given the high gravity and eccentricity of the planet, the GCM was run for 63 Earth days. Despite this short run time, this amounts to approximately 21 orbits of XO-3b, sufficient time for the model to have converged.

Unlike hot Jupiters on circular orbits, eccentric hot Jupiters allow us to investigate the atmospheric response to time-varying incident flux. We use our 3D simulations to inspect wind patterns and temperature gradients at apoapse and periapse at pressures of 10 and 100 mbar (Figure 5.13). At periapse, the GCM predicts a large

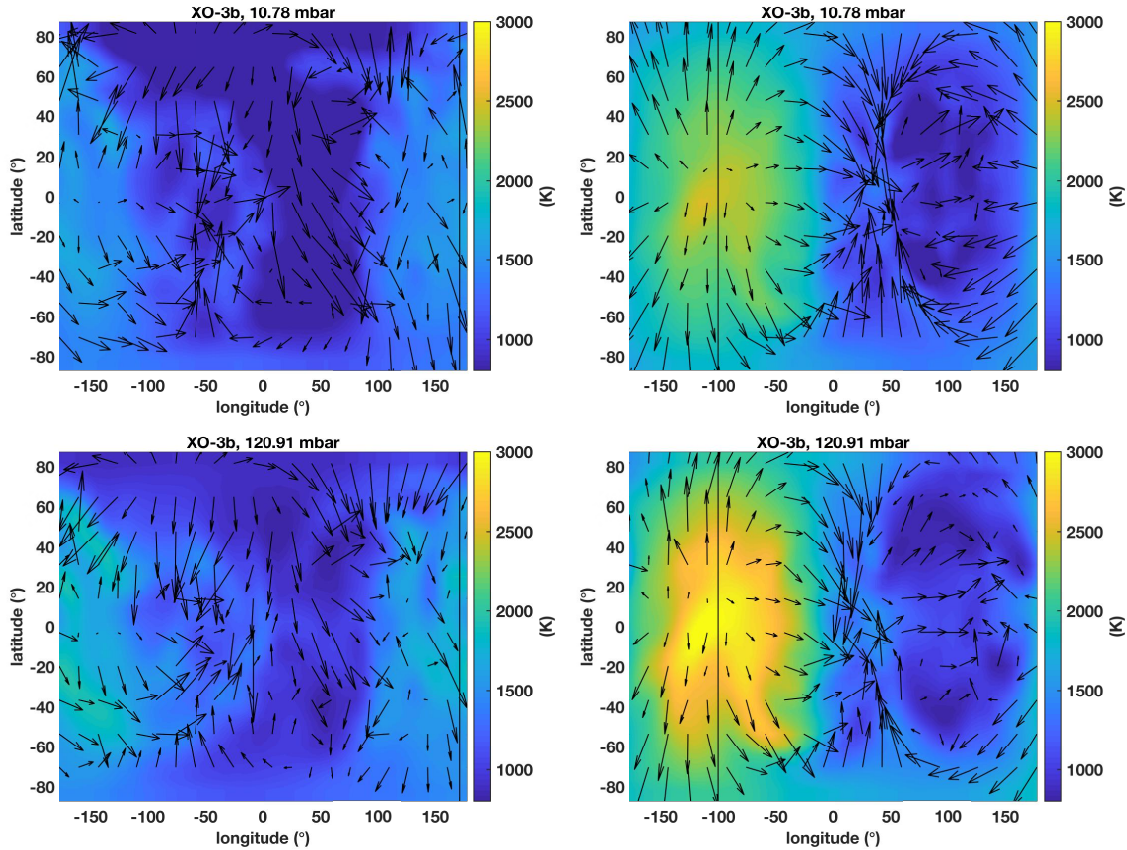


Figure 5.13: Temperature (colorscale) and winds (arrows) at the ≈ 10 mbar and ≈ 120 mbar level of our $1\times$ solar model at snapshots corresponding to apoapse (left) and periapse (right). The substellar longitude is indicated by the solid vertical line. At periapse, the model exhibits a large temperature contrast between the dayside and nightside of the planet. At apoapse, the temperature gradient is attenuate and the predominant wind zonal and meridional flows are suppressed.

temperature contrast between the dayside and nightside of the planet with large zonal (east-west) and meridional (north-south) flows from the substellar point to the limbs and antistellar point. Conversely, at apoapse, the atmosphere is comparatively quiescent, with low temperature contrasts from dayside to nightside, and unorganized flow. This behavior is in broad agreement with previous GCMs of highly eccentric exoplanets, including HD 80606b (Lewis et al. 2017b) and HAT-P-2b (Lewis et al. 2014).

Comparing GCM predictions to our *Spitzer* phase curves in Figure 5.12, we find that the planetary 3.6 μm flux is greatly underestimated throughout the orbit. As noted in section 5.3, this discrepancy is likely due to issues with the 3.6 μm observations. However, it is surprising that the 3.6 μm eclipse depth is also underestimated. Assuming the absence of the formation of a strong thermal inversion in the dayside atmosphere of XO-3b, the relative flux from the planet at 3.6 μm vs. 4.5 μm is a strong function of the pressures and hence atmospheric temperatures being probed by each channel. As the GCM assumes instantaneous equilibrium chemistry in the atmosphere it cannot capture possible disequilibrium processes that may affect abundances of key species such as CH_4 and CO that are strong absorbers in the 3.6 and 4.5 μm *Spitzer* bandpasses respectively. Visscher (2012) highlights that for eccentric hot Jupiters like XO-3b orbit induced thermal quenching can produce a significant reduction in the abundance of CH_4 in the planet’s atmosphere throughout its orbit. Such a scenario would naturally allow the 3.6 μm channel to probe deeper into XO-3b’s atmosphere resulting in a deeper than expected secondary eclipse depth in that channel.

The numerical model is able to correctly predict the amplitude of the 4.5 μm phase curve, although the peak and trough occurs slightly later than the *Spitzer*’s data. The model seems to adequately predict the cooling timescale of the planet at 4.5 μm , but underestimates the heating timescale where the discrepancy is more apparent after transit. Although predictions from the GCM match well with the flux measured from XO-b from eclipse through periastron and into transit, especially at 4.5 μm , the GCM predicts a significantly shallower increase in the planetary flux between the transit and eclipse events. As highlighted in other studies of eccentric hot Jupiters such as HAT-P-2b (e.g, Lewis et al. 2013, 2014) and HD80606b (e.g., ?), the assumption of a “pseudo-synchronous” rotation rate for hot Jupiters on eccentric orbits can result in inconsistencies between model predictions and observations. Near periastron passage, the thermal structure of the planet is dominated by the intense transient heating that results in the theoretical flux from the planet to be fairly insensitive to the assumed rotation rate. However away from periastron passage the assumed rotation rate plays a stronger role in shaping the phase dependent flux

from the planet (see discussion in [Lewis et al. 2014](#) in the context of HAT-P-2b and ? in the context of HD80606b). A rotation rate that is slower than the assumed pseudo-synchronous rotation rate would result in the cooler hemisphere of XO-3b being projected toward an earth observer for more the time between the transit and secondary eclipse event that would mimic a slower than expected heating rate for the planet.

The energy balance model allows P_0 , A_b , E_{int} and V_{wind} to be free-parameters, constant across the planet and throughout the orbit. In contrast, these quantities are spatially and temporally variable in the GCM and the local pressure levels of absorption and re-emission, Bond Albedo and winds are computed self-consistently assuming equilibrium chemistry. Additionally, the EBM is compared with each *Spitzer* phase curve separately while the simulated GCM phase curves are derived from the same simulation. The internal heat, E_{int} , is a free parameter that is explored in the EBM but not in the GCM. Given the atmospheric temperature expected for XO-3b and assumption of chemical equilibrium, the 3.6 micron photosphere will generally be located at deeper pressures (400 mbar) compared to the 4.5 μm photosphere (100 mbar). Therefore, increasing internal heat in the GCM could serve to increase the temperature at depth and provide a better prediction to the 4.5 μm phase curve. The discrepancy between the 3.6 μm phase curve and the GCM prediction could also be due instrumental issues with the 3.6 μm channel. However, the GCM also under-predicts the robust 3.6 μm eclipse depth and instrumental effects are unlikely to be the cause for this difference.

5.5.5 Possible Inflated Radius of XO-3b

Given the significant difference between the radius and mass of XO-3 reported by [Stassun et al. \(2017\)](#) and previously reported parameters, we re-determined these parameters by updating the stellar $T_{\text{eff}} = 6759 \pm 79$ K from the latest PASTEL spectroscopic catalog ([Soubiran et al. 2020](#)) and the parallax to the *Gaia* EDR3 value ([Gaia Collaboration et al. 2021](#)), then applied all of the other empirical parameters and calculations described in [Stassun et al. \(2017\)](#) with a correction described in [Stassun & Torres \(2018\)](#). We find a stellar mass and radius of $M_* = 1.21 \pm 0.15 M_\odot$ and $R_* = 1.407 \pm 0.038 R_\odot$ and a planetary mass and radius of $M_p = 11.79 \pm 0.98 M_J$ and $R_p = 1.295 \pm 0.066 R_J$.

To contextualize these new constraints, we compare them with planetary interior structure models based on [Thorngren & Fortney \(2018\)](#). These are 1-D evolution models that solve the equations of hydrostatic equilibrium, mass conservation, and the relevant equations of state. The most important free parameters are the bulk

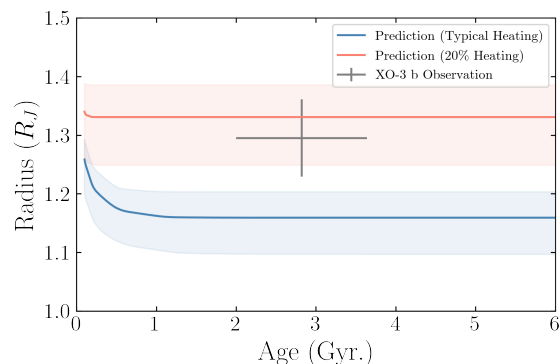


Figure 5.14: Theoretical planet radius vs age for XO-3b with typical heating (blue) and with additional heating (red) compared to XO-3b’s observed radius. The shaded swatches represent model uncertainties, dominated by the compositional uncertainties.

metallicity Z_p and the anomalous heating, which we parametrize as a fraction of the incident flux. Using heating values fitted from the observed hot Jupiter population (Thorngren & Fortney 2018) and a distribution of bulk metallicities inferred from the warm Jupiter population (Thorngren et al. 2016), we predict a range of expected radii for the observed mass and flux.

Figure 5.14 shows this radius plotted against age, and suggests that the observed radius of XO-3b is about 2σ larger than expected. Interestingly the expected radius of XO-3b is consistent with the observed radius of the planet if we use a high 20% insolation interior heating. Such a relationship between the internal heating and planetary radius has been previously proposed for KELT-1b, a $27-M_J$ brown dwarf companion (von Essen et al. 2021). Given the observational uncertainties, this means that we are either measuring the radius at 2 sigma above the true value or the planet is inflated beyond the level expected for its time-averaged flux (Thorngren et al. 2019).

If we interpret the radius of the planet as being linked to internal heating, then there are many possible candidate sources of heat. First, the planet is expected to experience tidal heating and it is possible we are catching the planet in a few Myr window during which it is rapidly circularizing (Mardling & Lin 2002; Ibgui & Burrows 2009; Millholland 2019). Since the observed mass of the planet is less than 1σ below the deuterium limit, it is possible that the true mass of the planet is slightly above the deuterium limit and it could take gigayears to finish burning (Spiegel et al. 2011; Phillips et al. 2020). Even if somewhat below this limit, it is likely that at least some of the deuterium in the planet has or will be burned (Spiegel et al. 2011; Bodenheimer et al. 2013); the main issue therefore is whether the heating is sufficient to explain

the radius at this age, but that is a difficult question outside the scope of this work. Another possibility is that the planet could be experiencing a Cassini State 2 with high obliquity that would increase the tidal dissipation of the planet (Fabrycky et al. 2007; Adams et al. 2019). Thermal tides, advection of potential temperatures, and Ohmic dissipation are proposed mechanisms for the general radius inflation problem that may also play an important role on XO-3b (e.g. Socrates 2013; Tremblin et al. 2017; Thorngren & Fortney 2018). Ultimately, unusually hot interior would likely be explained by a combination of the usual hot Jupiter inflation effect operating in conjunction with one or more of these other, less common heat sources.

5.6 Summary and Conclusion

We presented the analysis of new *Spitzer*/IRAC observations of the curious XO-3 system harbouring a massive $M_p = 11.79 \pm 0.98 M_{\text{jup}}$ inflated hot Jupiter with $R_p = 1.295 \pm 0.066 R_{\text{jup}}$ on a 3.2 day orbit with an orbital eccentricity of $e = 0.2769$. The full-orbit $3.6 \mu\text{m}$ and $4.5 \mu\text{m}$ *Spitzer*/IRAC phase curves of XO-3b yield a secondary eclipse depths of 1770 ± 180 ppm and 1610 ± 70 ppm at $3.6 \mu\text{m}$ and $4.5 \mu\text{m}$, respectively. From the secondary eclipse portion of the $3.6 \mu\text{m}$ partial phase curve of XO-3b obtained in 2010 (PI: P. Machalek, PID 60058), we retrieve an eclipse depth of 1520 ± 130 ppm which agrees with our more recent phase curve observations, but is 5σ discrepant with Machalek et al. (2010)’s results. Our observations therefore suggest no evidence for the thermal inversion on the dayside at secondary eclipse proposed by Machalek et al. (2010). The discrepancy is likely due to the less efficient observing mode used by Machalek et al. (2010) and resulting systematics.

Unfortunately, detector systematics are difficult to decorrelate from our $3.6 \mu\text{m}$ phase curve. Nonetheless, we compare our reliable $4.5 \mu\text{m}$ phase curve observations to multiple atmospheric models to constraint the radiative and advective properties of XO-3b. We use an energy balance model, assuming the Hut (1981) prescription for pseudosynchronous rotation rate, to fit the more reliable $4.5 \mu\text{m}$ observations and find a Bond albedo of $A_b = 0.106_{-0.106}^{+0.008}$ best-fits our data. We also estimates an average equatorial wind speed v_{wind} of $3.13_{-0.83}^{+0.26}$ km/s, in agreement with the ~ 2.5 km/s equatorial wind speeds predicted near periastron by a general circulation model. Our energy balance model fit suggest that the mixed layer of the atmosphere on a planet-averaged extends down to $P_0 = 2.40_{-0.16}^{+0.92}$ bars which is consistent with our 1D radiative transfer model that predicts shortwave light absorbed at deeper pressures. We also compare our phase curves with predictions from a GCM and find good agreement at $4.5 \mu\text{m}$ and large discrepancies at $3.6 \mu\text{m}$. While the disagreement

could be due to detector systematics spoiling the 3.6 μm phase curve, it's unlikely to be culprit for the difference in *Spitzer*-measured and GCM-predicted 3.6 μm eclipse depths. Planetary evolution models suggest that XO-3b is unusually large for its mass. Interestingly, additional heating equivalent to 20% insolation could explain its observed radius. If our results are interpreted as internal heat, the cryptic source of heating could be deuterium burning or tidal dissipation due to the orbital eccentricity or the high planetary obliquity.

Better characterization of stellar properties resulting in stringent constraints on the planet's mass would allow us to determine if the radius of XO-3b is really unusual. Further investigations with the James Webb Space Telescope would enable a search for clouds and could better constrain the presence of a temperature inversion at orbital phases other than at superior conjunction. Phase curve observations at other wavelengths can also better constraint the planetary flux and hence cryptic heating. Along with, HD 80606b, a giant planet with an orbital eccentricity of 0.93, gas giants with moderate orbital eccentricity, such as XO-3b and HAT-P-2b, offer a unique opportunity to characterize the gas giants at different stages of planet migration and help constrain planetary evolution theories.

Acknowledgments

L.D. acknowledges support in part through the Technologies for Exo-Planetary Science (TEPS) PhD Fellowship, and the Natural Sciences and Engineering Research Council of Canada (NSERC)'s Postgraduate Scholarships-Doctoral Fellowship. This work is based on archival data obtained with the Spitzer Space Telescope, which is operated by the Jet Propulsion Laboratory, California Institute of Technology under a contract with NASA. T.J.B. acknowledges support from the McGill Space Institute Graduate Fellowship, the Natural Sciences and Engineering Research Council of Canada's Postgraduate Scholarships-Doctoral Fellowship, and from the Fonds de recherche du Québec – Nature et technologies through the Centre de recherche en astrophysique du Québec.

Software:

`astropy` ([Astropy Collaboration et al. 2013](#)), `emcee` ([Foreman-Mackey et al. 2013](#)), `batman` ([Kreidberg 2015](#)), `SPCA` ([Dang et al. 2018](#); [Bell et al. 2021](#)), `Bell_EBM` ([Bell & Cowan 2018](#))

Appendix: Tidal Heating

Time-dependent tidal distortion of a body leads to internal heating (Peale & Cassen 1978; Peale et al. 1979; Wisdom 2004). Hence, eccentricity and obliquity tides have been proposed as the missing energy source to explain the anomalously large radius of some hot Jupiters. We estimate the rate of energy dissipation using the formalism described in Levrard et al. (2007) which takes into account the effect of synchronous rotation:

$$\frac{dE_{\text{tides}}}{dt} = 2K \left[N_a(e) - \frac{N^2(e)}{\Omega(e)} \frac{2x^2}{1+x^2} \right] \quad (\text{S10})$$

where $\Omega(e)$, $N(e)$, and $N_a(e)$ are functions of the orbital eccentricity and are defined as:

$$\Omega(e) = \frac{1 + 3e^2 + \frac{3}{8}e^4}{(1 - e^2)^{9/2}}, \quad (\text{S11})$$

$$N(e) = \frac{1 + \frac{15}{2}e^2 + \frac{45}{8}e^4 + \frac{5}{16}e^6}{(1 - e^2)^6}, \quad (\text{S12})$$

$$N_a(e) = \frac{\left(1 + \frac{31}{2}e^2 + \frac{255}{8}e^4 + \frac{185}{16}e^6 + \frac{25}{64}e^8\right)}{(1 - e^2)^{15/2}}. \quad (\text{S13})$$

and where $x = \cos \epsilon$, ϵ is the planet's obliquity (the angle between the equatorial and orbital planes) and

$$K = \frac{3}{2} \frac{k_2}{Q_n} \left(\frac{GM_p^2}{R_p} \right) \left(\frac{M_*}{M_p} \right)^2 \left(\frac{R_p}{a} \right)^6 n \quad (\text{S14})$$

where k_2 is the planet's potential Love number of degree 2, Q_n is the planet's annual tidal quality factor, G is the gravitational constant, and n is the planet's mean motion which is approximately $\sqrt{GM_*/a^3}$. Assuming that XO-3b has a zero obliquity and Jupiter's tidal Love number $k_2 = 0.565 \pm 0.006$ (Durante et al. 2020), we find that a tidal quality factor of $Q \sim 6 \times 10^3$ is required to explain the excess flux of $1.3 \times$ insolation inferred for the $3.6 \mu\text{m}$ phase curve.

Epilogue

I show, again, that phase curve observations of a close-in gas giant cannot be solely described by its orbital configuration – the age of the system matters in the interpretation of our data. Shortly after the publication of this work, evidence for tidal evolution of XO-3b has been reported using TESS observation (Yang & Wei 2022). Additionally, a 3-sigma detection of the NUV transit of XO-3b with the Neil Gehrels Swift Observatory suggests that the apparent NUV radius of XO-3b $2.5 \pm 0.2 R_{Jup}$, a factor of two larger than the optical radius (Corrales et al. 2021). Given these recent development on elucidating the puzzling XO-3b, I was invited to join an observing proposal led by Lia Corrales at the University of Michigan to acquire ultra-violet transit observations of XO-3b with the Wide-Field Camera 3 (WFC3) aboard the *Hubble* space telescope.

I later presented this work at the Ariel Summer Consortium Meeting in 2021 and was promoted to co-lead of *Ariel*'s Eccentric Planet team. Atmospheric Remote-sensing Infrared Exoplanet Large-survey (*Ariel*) is a European Space Agency mission, launching in 2029, designed to study what exoplanets are made of, how they formed and how they evolve by characterizing the climate of a large sample of 1000 exoplanets. Eccentric planets allow one to probe tidal migration processes and their respective atmospheric states. In addition, I am a member of a collaboration who successfully competed for *JWST* time to observe a partial phase curve of the highly eccentric ($e = 0.93$) gas giant HD 80606b (Sikora et al. 2021). Combined, these *JWST* observations will constrain radiative, advective and chemical atmospheric timescales of eccentric gas giants and will serve as guideline for our *Ariel* survey and help to identify traces of key features linked to their evolutionary history.

Chapter 6

A Hell of a Phase Curve

This thesis chapter presents my unpublished contribution to the study of lava worlds.

Prologue

One rare class of objects are lava planets, which have orbital periods shorter than one day and bulk densities suggestive of terrestrial composition. The drastic planetary and orbital properties suggest that these planets could be the result of extreme cases of migration and evolution. [Lee & Chiang \(2017\)](#) showed that the population of USPs could be accounted for by tidal orbital decay of planets formed with material collected near the inner edge. Although, some USPs have been suggested to be the remnants of larger stripped of hot Jupiters (e.g. [Valsecchi et al. 2015](#); [Jackson et al. 2016](#)), evidence hints that the majority of them likely have a different origin than hot Jupiters. In particular, USPs are often found in multi-planet systems and do not exhibit the host star metallicity dependence seen in hot Jupiters ([Sanchis-Ojeda et al. 2014](#); [Winn et al. 2018](#)).

Their daysides are blasted with stellar irradiation, reaching temperatures hot enough to melt rock and harbour a magma ocean (e.g. [Kite et al. 2016](#); [Dai et al. 2019](#)). For this reason, lava worlds are particularly compelling to study for the insight they provide into the behavior of materials at extreme temperature, and volatile cycling which depends on the entire history of the planet. However, the few existing observations of lava planets do not yet paint a clear picture. In this chapter, I present my contribution to the study of lava planets, a category of rocky exoplanets with an

orbital period of a day or less. First, I will summarize the re-analysis of the multi-epoch *Spitzer* phase curve of the hot super-Earth, 55 Cnc e, led by undergraduate students Samson Mercier and Alex Gass, to whom I was the primary research advisor. Then, I will discuss my successful *JWST* cycle 1 program to characterize the climate of the lava planet, K2-141b.

6.1 Overview of Lava Planets

Due to their incredibly intense irradiation, ultra-short period planets (USPs) may be the stripped cores of gas-rich planets that lost their atmospheres to escape processes, e.g., photo-evaporation (Owen & Wu 2017; Lopez 2017). Indeed, most USPs with known masses have densities consistent with Earth-like bulk compositions (Heng 2018; Dai et al. 2019); these are the lava planets, with scorching dayside temperatures (>1000 K) hot enough to maintain a dayside magma ocean tens of km deep (Lutgens et al. 2014). Figure 6.1 shows a schematic view of a synchronously-rotating lava planet. The dayside magma pool is likely made of the most refractory constituents, Al_2O_3 and CaO , while the relatively volatile MgO and SiO_2 can vaporize into the overlying atmosphere (Kite et al. 2016). Indeed, Schaefer & Fegley (2009) predicted that a bulk earth composition lava planet would have an atmosphere of O, O_2 , SiO , Na, K and SiO_2 . At temperatures greater than about 1000 K, SiO_2 evaporates into $\text{SiO}+\text{O}$, hence the possibility of an extended, global oxygen atmosphere if it is not lost to space faster than its production rate.

6.2 Re-Analysis of 55 Cnc e’s Phase Curve

Hot Jupiters have so far benefited the most from thermal phase observations with *Spitzer*, due to their short-orbit, high temperatures and large radius. The study of their smaller counterpart remains largely unexplored due to the challenges of observing small exoplanets. Fortunately, the discovery of USP’s have enabled a new benchmark in atmospheric characterization. In 2016, Demory et al. (2016b) reported the first detection of thermal phase variation of a hot super-Earth in multi-epoch observations of 55 Cnc e. Their phase curve exhibits an *eastward* hotspot shift of 41 degrees which is suggestive of strong heat transport and surprising as these objects are predicted to only have a thin atmospheric layer dominated by rock vapour (Ito et al. 2015). Even if 55 Cnc e had a thick atmospheric envelope, due to the short radiative timescales at such high temperatures, we expect poor heat recirculation even if the planet has a thick atmosphere (Hammond & Pierrehumbert 2017).

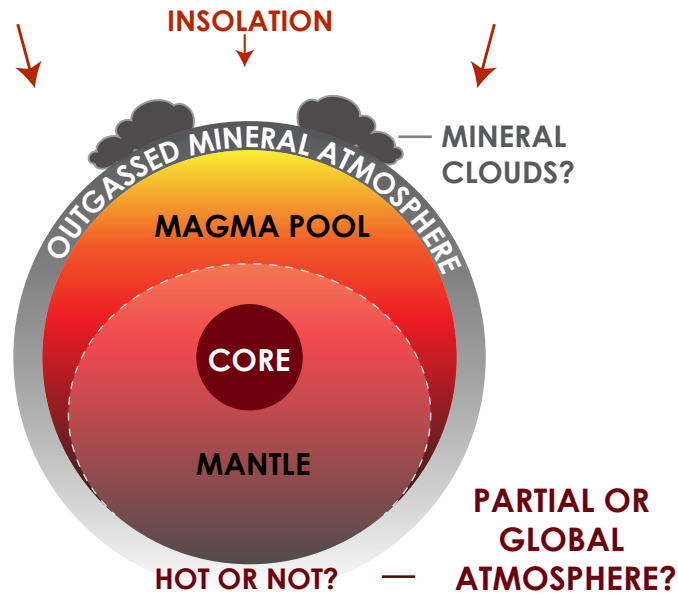


Figure 6.1: Adapted schematic of a K2-141b from [Kite et al. \(2016\)](#), not to scale, showing the dayside magma pool outgassing minerals into the atmosphere.

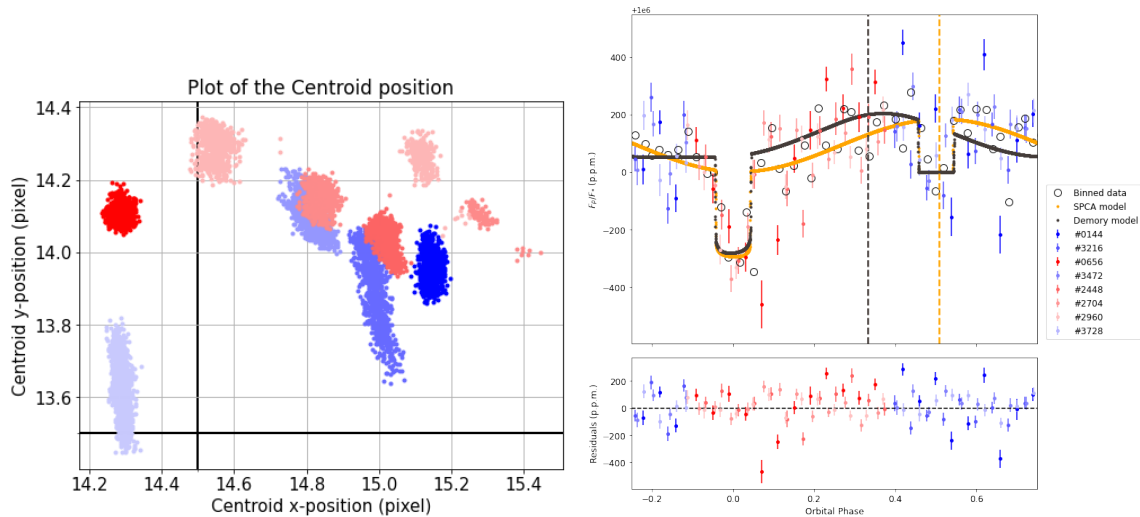


Figure 6.2: Plotted on the left is the centroid position on the IRAC detector and on the right is the phase folded reduced phase curve after decorrelating for detector systematics. In both plots the 8 AORs are separated into two groups: the red group represents the phase range -0.1 to 0.4 and the blue group represents the phase range 0.4 to 0.9. On the right, our best-fit is denoted by the yellow curve and the previous published phase curve by [Demory et al. \(2016b\)](#) is denoted by the black line.

As shown in Figure 6.2, the *Spitzer* phase curve observations are not continuous

as 55 Cnc e is a naked-eye star. The image exposure time is reduced to 0.02 s to avoid detector saturation, consequently, the data volume is filled before 55 Cnc e completes a full-orbit. The authors have instead opted for multi-epoch observations spanning half an orbit at a time, however, the position of the target on the detector for each visit does not overlap as shown in Figure 6.2, making the removal of detector systematics more challenging. We also note that the peak of the phase curve presented in Demory et al. (2016b) coincides with the orbital phase of a recurrent break in the *Spitzer* observations which begs for a re-analysis.

We present our attempt to re-produce their results using the Spitzer Phase Curve Analysis Pipeline (SPCA) to detrend the observations for known instrumental effects. Using BLISS mapping, we retrieve a phase curve with a phase semi-amplitude of $96.3_{-4.3}^{+2.3}$ and a phase offset of 4.14 ± 5.05 degrees west – which are consistent with the expected poor heat recirculation efficiency. Additionally, a dayside and night-side temperature of $T_{\text{day}} = 3845_{-412}^{+457}\text{K}$ and $T_{\text{night}} = 871_{-206}^{+242}\text{K}$ were inferred from our resulting lightcurves. While we attempted to replicate Demory et al. (2016b)’s analysis, there are certain discrepancies in our analysis that could plausibly explain the different results between our analysis:

- **centroiding:** Detrending with BLISS mapping depends heavily on the target’s centroid on the images. In our analysis, we used flux-weighted-mean centroids while Demory et al. (2016b) uses a 2D Gaussian fit to determine the target’s centroid in each image. It is possible that our different centroiding strategies led to different astrophysical parameters.
- **photometry:** We used a 2.2 pixel radius circular aperture for our photometric scheme for all different visits. In comparison, Demory et al. (2016b) used a fixed aperture with variable radius ranging from 2.6 to 3.4 pixels for each visit. It seems likely to us that these additional parameters could explain why we cannot reproduce the original results.

As shown in Figure 6.2, using a slightly different analysis scheme, we obtain a large phase amplitude and a smaller phase offset that does not coincide with an observation break. However, the larger observed scatter from our analysis could be astrophysical in nature, as both Demory et al. (2016a) and Tamburo et al. (2018) have reported eclipse depth variability with *Spitzer*. Indeed, the astrophysical variability could have been removed by Demory et al. (2016b) because they used a different photometric aperture for each visit.

If the *Spitzer* phase modulation is interpreted as a planetary signal, then 55 Cnc e either has a global atmosphere covering both hemispheres of the planet or a local

dayside atmosphere with a short radiative timescale ensuring poor heat distribution. While tidal heating is likely insufficient, the surprisingly high dayside brightness temperature can be explained with the presence of SiO in the atmosphere. Lava planets with silicate atmospheres are prone to temperature inversions due to UV absorption by SiO vapour (Ito et al. 2015; Zilinskas et al. 2022). Moreover, Nguyen et al. (2022) showed that the balance between UV heating and cooling of SiO leads to very hot stratospheric temperatures everywhere in the dayside, further enhancing the eclipse depth. In the balance, the larger dayside temperature and smaller offset obtained from our re-analysis is more consistent with theoretical predictions for these exotic planets. These results have been submitted to the *Astrophysical Journal* as Mercier et al.

6.2.1 Authors Contribution

The analysis pipeline was co-written by Taylor Bell and I. Alex Gass used SPCA to retrieve photometric measurements from the *Spitzer* images, while Samson led the analysis and instrumental effects decorrelation. I acted as primary advisor to Samson and Alex, guided their analysis and helped with the redaction of the manuscript and interpretation of the results.

6.3 Mapping the Atmosphere and Surface of K2-141b

More recently, I joined the international Team Lava collaboration that successfully competed for *Spitzer*, *Hubble*, and most notably *JWST* phase curves of lava planets. Among known lava planets, K2-141b is one of the very best targets: due to its relatively small and nearby host star, and the smallest noise. Barragán et al. (2018) report the following planetary properties: $M_p = 5.31(46)M_\oplus$, $R_p = 1.5(1)R_\oplus$, for a density of 8.5 g/cm^3 , suggestive of 50:50 silicate (MgSiO) and iron (Fe) composition (Dai et al. 2019). Fortuitously, the independent analysis of Malavolta et al. (2018) reports consistent values. At 2.2 stellar radius from the center of its host star, over 2/3 of the planet’s surface is illuminated (Nguyen et al. 2020) and K2-141b may intermittently pass through its star’s corona.

Led by Sebastian Zieba, our joint analysis of *K2* and *Spitzer* phase curve observations of K2-141b revealed hints of a tenuous rock vapor atmosphere. To further our understanding of lava worlds, I led the successful *JWST*/MIRI proposal to observe

3 full-orbit phase curves of the lava planet K2-141b (Dang et al. 2021). Our *JWST* observations could lead to the first detection of the rock vapour on a lava planet as theory predicts these planets to have tenuous rock vapour atmosphere outgassed from their molten dayside (Zilinskas et al. 2020). Whether lava planets have a partial day-side atmosphere or a global atmosphere remains a major outstanding question which we will resolve with our observations (Demory et al. 2016b), 2017ApJ...849..152H. Our spectroscopic phase curve will also reveal the first 3D map of the thermal and chemical structure of a terrestrial planet which will allow us to determine the extent of its atmosphere while providing insights into modelling processes that operate on lava worlds.

Detecting Rock Vapour on a Lava World

Although lava planets are expected to have lost their primordial H/He envelope, models predict that silicate melt at the high temperatures of the sub-stellar region has an appreciable vapor pressure (0.01-0.1 bar) making a rock vapor atmosphere on the stellar side of the planet likely (Castan & Menou 2011). Given the irradiation temperature of K2-141b, Miguel et al. (2011) predict an atmosphere dominated by Na, O, O₂, SiO, Mg, and Fe based on the models of Schaefer & Fegley (2009). Of these, only SiO has significant spectral features in the thermal infrared. Ito et al. (2015) have simulated the eclipse spectra of lava planets and find they are dominated by two silicate features: the usual 9 μm feature, and a 4 μm feature. Our simulated dayside emission spectrum of K2-141b, shown in Figure 6.3, is calculated assuming an atmosphere made by outgassing from the surface (Miguel et al. 2011) and combined with radiative transfer and chemical equilibrium calculations, based on Zilinskas et al. (2021, 2020) and also predicts the strong emission feature of SiO. Notably, our model predicts a dayside temperature inversion due to the high opacity of SiO – hence the SiO feature appear in emission (Ito et al. 2015; Zilinskas et al. 2020). Indeed, in addition to detecting a mineral atmosphere, our proposed spectroscopic phase curve observations of K2-141b, *will revealed the first 2D picture of the atmosphere of a lava planet, as previously done for hot Jupiters (Stevenson et al. 2014; Kreidberg et al. 2018; Arcangeli et al. 2019), with SiO as a means to probe the vertical temperature profile.*

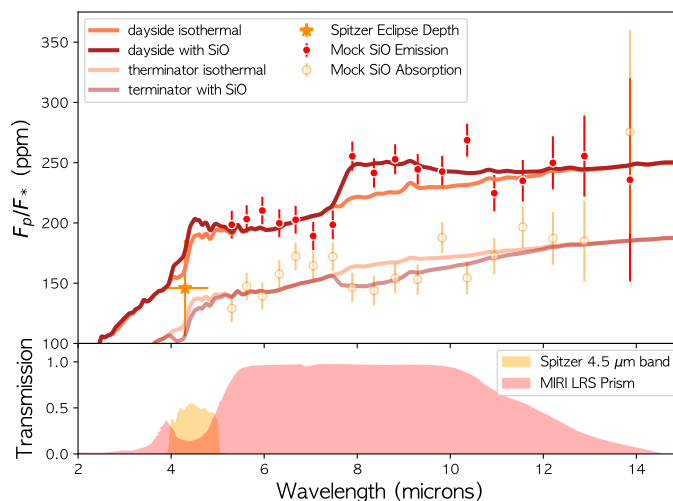


Figure 6.3: Expected dayside emission spectrum K2-141b based on [Zilinskas et al. \(2020a,b\)](#) and possible SiO feature in absorption towards the planet’s terminator. The isothermal scenarios for the dayside and the terminator are shown in orange. Simulation of a dayside SiO detection in emission and terminator SiO detection in absorption are shown in red and orange respectively. The uncertainties are estimated using `pandexo` ([Batalha et al. 2017.](#))

Determine the presence of a global atmosphere

If the planet is tidally locked, the magma pool is subject to enormous temperature gradients, but a surface temperature gradient is a poor way to induce mixing. As such, the magma pool is expected to do a poor job of recirculating heat to the permanent nightside ([Léger et al. 2011](#); [Kite et al. 2016](#)). Even the vaporized rock is not expected to substantially increase the frigid nightside temperatures since such an atmosphere barely reaches the terminator ([Castan & Menou 2011](#); [Kite et al. 2016](#); [Nguyen et al. 2020](#)). Phase observations of a significantly lower density planet, 55 Cnc e, shows a hotspot offset from the substellar point which has been interpreted as the presence of a thick atmosphere ([Demory et al. 2016b](#); [Hammond & Pierrehumbert 2017](#)). Recent 4.5 μm *Spitzer* phase observations of K2-141b on the other hand, show no hotspot offset as expected for a synchronously rotating lava planet ([Zieba et al. 2022](#)). However, this does not rule out the presence of a global atmosphere: none of our GCM simulations of K2-141b with a global atmosphere, based on [Hammond & Pierrehumbert \(2017\)](#) and [Mendonça et al. \(2016\)](#), show an appreciable hotspot offset because the planet’s high rotation rate, which gives a very narrow jet that is limited in its effect, despite its high speed. Our GCM simulations of K2-141b show that a weak greenhouse gas like N_2 or O_2 does not appreciably increase the

surface temperature on the nightside, but significantly increases the temperature of the atmosphere. Alternatively, a strong greenhouse background gas like CO_2 increases the surface temperature on the nightside of the planet while decreasing the strength of thermal inversion, hence decreasing the temperature of the atmosphere.

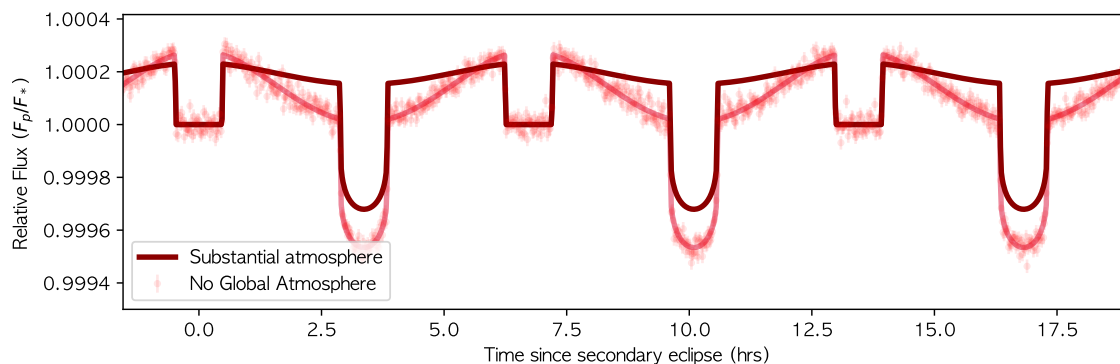


Figure 6.4: A partial atmosphere phase curve can be distinguished by its large phase variation amplitude and low nightside temperature (Nguyen et al. 2020) while a global atmosphere would have a smaller phase curve amplitude as predicted with GCM simulations (Hammond & Pierrehumbert 2017). Our simulated proposed observation of K2-141b with MIRI LRS binned over the entire band without a global atmosphere with uncertainty estimated using `pandexo` (Batalha et al. 2017) with a photometric uncertainty of ~ 13 ppm.

A dayside temperature of 2049 ± 361 K and a nightside temperature of $T_n < 1712$ K at 2σ are inferred from the *Spitzer* phase curve (Zieba et al. 2022). However, the *Spitzer* $4.5\ \mu\text{m}$ observations are right in an SiO feature, hence it is impossible to tell whether they are probing the atmospheric temperature rather than the surface, if there is an atmosphere on the planet’s nightside. With MIRI LRS, we will be able to observe phase curves of K2-141b both in and out of the SiO feature, hence, mapping the temperature distribution of its surface and its atmosphere. JWST/MIRI is much more sensitive to lower temperatures, so our phase curves and will be able to better constrain the nightside temperature. If the planet has no background gas then the nightside is a barren frigid rock, easy to identify due to its large phase curve amplitude and cold nightside as shown in Figure 6.4. Our simulations show that if there is a background gas like O_2 , then the SiO spectral feature will persist to the nightside, but as an emission feature due to the stronger thermal inversion. If the background gas is a strong greenhouse gas like CO_2 , then the nightside surface temperature will be hotter than the overlying atmosphere resulting in an SiO absorption feature as shown in Figure 6.3. *Whether lava planets have a partial dayside atmosphere or a global atmosphere remains a major outstanding question we will resolve with our observations.*

Beyond the Lava Planet K2-141b

There are precious few self-consistent model predictions for partial atmospheres on hot terrestrial planets: even the heroic holistic effort of [Kite et al. \(2016\)](#) presented a pallet of possible scenarios due to the great number of unknowns. Lava planets fall in a blind spot of atmospheric models: GCMs break when the dominant atmospheric gas condenses, while 1D *Ingersoll*-style simulations neglect much of the relevant radiative transfer, coriolis forces and convection. The same issues plague the outer edge of the habitable zone ([Wordsworth et al. 2011](#)) and intermittent lava worlds in the Solar System such as Io, showing tantalizing evidence of harbouring a cyclically overturning lava lake ([Ingersoll 1989](#); [de Kleer et al. 2017](#)). *The most extreme cases are often the most revealing* and observations of K2-141b could provide empirically-motivated insights into collapsing atmospheres.

Epilogue

In this chapter, I present first attempts to characterize the climate of lava worlds and potential insights the MIRI/*JWST* observations of K2-141b can provide into our understanding of lava planets ([Dang et al. 2021](#)). I have also been awarded a grant from the Canadian Space Agency to support this programs. In addition to K2-141b, other phase curves of lava planets will be acquired in the near future. In particular, *JWST* will observe also observe a full-orbit phase curve of K2-141b in the near infrared with NIRSpec ([Espinoza et al. 2021](#)), partial phase curves of 55 Cnc e with NIRCams and MIRI ([Hu et al. 2021](#); [Brandeker et al. 2021](#)), and a MIRI LRS phase curve of the super-Mercury GJ 367b ([Zhang et al. 2021](#)) during its Cycle 1 General Observers Program. These upcoming program will offer unprecedented details about the atmosphere of lava planets and could provide unmatched insights into the complex interplay between an exoplanet’s atmosphere and interior.

CHAPTER 6. LAVA WORLDS

Chapter 7

Conclusion

In this thesis, I used *Spitzer*/IRAC time-series observations for a variety of exoplanetary science investigations. With relatively large pixels size compared to the typical width of the target’s point-spread-function (PSF), time-correlated instrumental noise often plague *Spitzer* lightcurves as a result of variation in the telescope pointing and the non-uniform intra-pixel sensitivity of InSb detectors. To test the robustness of the surprising *westward* offset, I developed the Spitzer Phase Curve Analysis (SPCA) pipeline where I implemented most decorrelation techniques widely used at the time to make future phase curves analysis easier and reproducible. In Chapter 3 and 5, I use a suite of decorrelation to ensure reliability of our retrieved astrophysical parameters and determine the best detrending technique for the respective data set. One of the conclusions from my work, along with subsequent comprehensive *Spitzer* analysis using a similar detector model comparison (Bell et al. 2021) approach suggest that there is no optimal one-size fits all treatment to all data sets. Even when using the same detrending technique, such as our re-analysis of 55 Cnc e’s phase curve in Chapter 6, the exact details of its usage can lead to different retrieve astrophysical constraints. There are now over 30 hot Jupiters with infrared phase curves measurements enabling comparative exoplanetology studies to unveil atmospheric processes at play. Study cases in this thesis are forming a cautionary tale about using published analysis at face value if only one decorrelation method. Instead, a uniform analysis as presented in Bell et al. (2021) and May et al. (2022) are preferred to minimize instrumental model-dependent features.

I presented the first detection of a *westward* hot spot offset, in Chapter 3, on the young hot gas giant CoRoT-2b with an anomalously featureless dayside emergent spectrum. At the time of this publication, all hot Jupiters with similar *Spitzer* measurements exhibit either an *eastward* hot spot offset which has long been interpreted

CHAPTER 7. CONCLUSION

as a result of *eastward* super-rotating jets, a feature seen in purely hydrodynamical simulations. To explain the direction of the bright spot shift, I proposed 3 plausible explanation: 1) an asynchronous rotation causing steady-state *westward* winds as seen in [Rauscher & Kempton \(2015\)](#), 2) westward winds due to the coupling a partially ionized atmosphere and an deep magnetic field as suggested to explain the variable *Kepler* hotspot offset of HAT-P-7b ([Armstrong et al. 2016](#); [Rogers 2017](#)), and 3) partial coverage by optically thick clouds sculpting the thermal phase curve. All three scenarios are attractive as they might also explain other unusual features of CoRoT-2b. In particular, asynchronous rotation linked to the young age of CoRoT-2n (100-300 Myrs) can lead to tidal heating which is one of the mechanisms by which a Hot Jupiter can be inflated. The inflated radius of CoRoT-2b can also be related to the presence of a magnetic field as Ohmic dissipation can lead to an energetic interior. Clouds on the other hand are appealing as it could explain the spectrally featureless dayside emission. Each case supports the claim that hot Jupiters cannot be organized into a one-parameter family governed by the amount of stellar irradiation.

The *Spitzer* microlensing campaign offered a drastic study case for tackling instrumental systematics. Most *Spitzer* phase curves observations are acquired with continuous observations covering the entire orbital period, as such, many detrending techniques have been optimized for single epoch observations and vice-versa. As continuous observations were not the optimal observing strategy for a microlensing survey, a typical *Spitzer* microlensing light curve consists of multi-epoch observations, each composed of 6 to 12 dithered images. Due to the rigidity of the observing scheme, I identified Pixel Level Decorrelation as the best suited detrending method for crowded observations. As the instrumental systematics at dither position should be unrelated, each dither position will have a different detector model which significantly increases the number of detector parameters. To mitigate this, I introduced an iterative fitting method in [Dang et al. \(2020\)](#) allowing for common astrophysical model parameters to vary while the PLD coefficients are evaluated analytically at each step to limit the number of jump parameters. In return, this approach has since been used for multi-epoch observations of transiting planets which also requires a common astrophysical model but a different detector model for each visit ([Crossfield, priv. communication](#)). Despite the dissimilarity between planetary insights one may gain from the study of transiting exoplanets and microlensing planets, the observing techniques have significant overlap – by construction every microlensing survey is also a transit survey with sufficient photometric precision. As such, microlensing data sets can challenge the state-of-the-art detrending methods while enabling new approaches due to its unconventional constraints.

In Chapter 5, I analyze *Spitzer* observations of the eccentric hot Jupiter XO-3b

CHAPTER 7. CONCLUSION

with a mass of $\sim 12 M_{\text{Jup}}$ placing it close to the deuterium-burning limit, an important distinction between an exoplanet and brown dwarfs. Found in an intermediate regime of planetary mass where processes normally neglected for less massive hot Jupiters may come into play, XO-3b is an interesting case study for atmospheric dynamics and interior evolution. Compared with a series of atmospheric models, our *Spitzer* observations suggest XO-3b may be emitting more thermal flux than it's receiving from its host star. Interestingly, this could be related to the anomalously large radius of XO-3b for its age. Since XO-3b resides on an eccentric orbit, this guarantees that it is experiencing some amount of tidal heating. As it is more difficult to inflate a very massive gas giant, leftover heating from deuterium burning could be contributing to this inflation.

Finally, a re-analysis of the phase curve of 55 Cnc e is presented in Chapter 6. Initial analysis revealed an astounding 41 degree eastward shift of the hot spot. Our re-analysis supports a smaller hot spot offset and larger phase amplitude suggesting poor heat recirculation on 55 Cnc e all consistent with current understanding of lava worlds. In addition, the ultra-hot dayside temperature is in accordance with the predicted atmospheric thermal inversion for lava planets. These hot rocky planets are particularly compelling to study for the insight they provide into the behavior of materials at extreme temperature, and volatile cycling which depends on the entire history of the planet. Upcoming observations of lava planets such as K2-141b could allow for the detection of mineral composites such as SiO and for the determination of the extent of its atmosphere. Such measurements will provide empirical insights into atmospheric modelling.

More broadly, a general assumption behind many theoretical and observational studies of short-period planets is that most traces of their history have now been erased and their atmospheric state is strongly influenced by their current orbital configuration and corresponding stellar forcing. In short, the collection of work presented in this thesis shows evidence that the history of an exoplanet matters and impacts the atmospheric state of an exoplanet. In conclusion, this further suggests that exoplanets are not spherical cows, rather they are complex systems and understanding the interplay between various factors is key to interpreting our observations.

CHAPTER 7. CONCLUSION

References

- Adams, A. D., & Laughlin, G. 2018, *AJ*, 156, 28
- Adams, A. D., Millholland, S., & Laughlin, G. P. 2019, *AJ*, 158, 108
- Adcroft, A., Campin, J.-M., Hill, C., & Marshall, J. 2004, *Monthly Weather Review*, 132, 2845
- Akeson, R. L., Chen, X., Ciardi, D., et al. 2013, *PASP*, 125, 989
- Albrow, M. D., Yee, J. C., Udalski, A., et al. 2018, *ApJ*, 858, 107
- Alonso, R., Deeg, H. J., Kabath, P., & Rabus, M. 2010, *AJ*, 139, 1481
- Alonso, R., Guillot, T., Mazeh, T., et al. 2009, *A&A*, 501, L23
- Alonso, R., Auvergne, M., Baglin, A., et al. 2008, *A&A*, 482, L21
- Anderson, J., & King, I. R. 2000, *PASP*, 112, 1360
- Arcangeli, J., Désert, J. M., Parmentier, V., Tsai, S. M., & Stevenson, K. B. 2021, *A&A*, 646, A94
- Arcangeli, J., Désert, J.-M., Parmentier, V., et al. 2019, *A&A*, 625, A136
- Armstrong, D. J., de Mooij, E., Barstow, J., et al. 2016, *Nature Astronomy*, 1, 0004
- Arras, P., & Socrates, A. 2010, *Astrophysical Journal*, 714, 1
- Astropy Collaboration, Robitaille, T. P., Tollerud, E. J., et al. 2013, *A&A*, 558, A33
- Barragán, O., Gandolfi, D., Dai, F., et al. 2018, *A&A*, 612, 95
- Bean, J., Parmentier, V., Mansfield, M., et al. 2018, *Revealing Fact or Fiction in Spitzer Exoplanet Phase Curve Trends*, *Spitzer Proposal*

REFERENCES

- Beatty, T., Keating, D., Cowan, N., et al. 2018, A Test of the Fundamental Physics Underlying Exoplanet Climate Models, Spitzer Proposal
- Beatty, T. G., Marley, M. S., Gaudi, B. S., et al. 2019, *AJ*, 158, 166
- Bell, T. J., & Cowan, N. B. 2018, *ApJ*, 857, L20
- Bell, T. J., Zhang, M., Cubillos, P. E., et al. 2019, *MNRAS*, 489, 1995
- Bell, T. J., Dang, L., Cowan, N. B., et al. 2021, *MNRAS*, 504, 3316
- Benneke, B., Werner, M., Petigura, E., et al. 2017, *Astrophysical Journal*, 834, 187
- Bennett, D. P., Anderson, J., & Gaudi, B. S. 2007, *ApJ*, 660, 781
- Bodenheimer, P., D'Angelo, G., Lissauer, J. J., Fortney, J. J., & Saumon, D. 2013, *ApJ*, 770, 120
- Bodenheimer, P., Hubickyj, O., & Lissauer, J. J. 2000, *Icarus*, 143, 2
- Bordwell, B., Brown, B. P., & Oishi, J. S. 2018, *ApJ*, 854, 8
- Borsa, F., & Poretti, E. 2011, *Memorie della Societa Astronomica Italiana Supplementi*, 16, 80
- Borucki, W. J., Koch, D., Basri, G., et al. 2010, *Science*, 327, 977
- Bozza, V. 2010, *MNRAS*, 408, 2188
- Bozza, V., Bachelet, E., Bartolić, F., et al. 2018, *MNRAS*, 479, 5157
- Bozza, V., Shvartzvald, Y., Udalski, A., et al. 2016, *ApJ*, 820, 79
- Brandeker, A., Alibert, Y., Bourrier, V., et al. 2021, Is it raining lava in the evening on 55 Cancri e?, JWST Proposal. Cycle 1, ID. #2084
- Bruno, G., Deleuil, M., Almenara, J.-M., et al. 2016, *Astronomy and Astrophysics*, 595, A89
- Cabrera, J., Fridlund, M., Ollivier, M., et al. 2009, *Astronomy and Astrophysics*, 506, 501
- Calchi Novati, S., Gould, A., Udalski, A., et al. 2015a, *ApJ*, 804, 20
- Calchi Novati, S., Gould, A., Yee, J. C., et al. 2015b, *ApJ*, 814, 92
- Calchi Novati, S., Skowron, J., Jung, Y. K., et al. 2018, *AJ*, 155, 261

REFERENCES

- Calchi Novati, S., Suzuki, D., Udalski, A., et al. 2019, *AJ*, 157, 121
- Castan, T., & Menou, K. 2011, *ApJ*, 743, 36
- Challener, R. C., Harrington, J., Jenkins, J., et al. 2021, *The Planetary Science Journal*, 2, 9
- Charbonneau, D., Allen, L. E., Megeath, S. T., et al. 2005, *ApJ*, 626, 523
- Chung, S. J., Zhu, W., Udalski, A., et al. 2017, *ApJ*, 838, 154
- Chung, S.-J., Gould, A., Skowron, J., et al. 2019, *ApJ*, 871, 179
- Corrales, L., Ravi, S., King, G. W., et al. 2021, *AJ*, 162, 287
- Cowan, N. B., & Agol, E. 2008, *ApJ*, 678, L129
- . 2011a, *ApJ*, 726, 82
- . 2011b, *Astrophysical Journal*, 729, 54
- Cowan, N. B., Fuentes, P. A., & Haggard, H. M. 2013, *Monthly Notices of the Royal Astronomical Society*, 434, 2465
- Cowan, N. B., Machalek, P., Croll, B., et al. 2012a, *ApJ*, 747, 82
- Cowan, N. B., Voigt, A., & Abbot, D. S. 2012b, *Astrophysical Journal*, 757, 80
- Cubillos, P., Harrington, J., Lored, T. J., et al. 2017, *AJ*, 153, 3
- Cutri, R. M., Skrutskie, M. F., van Dyk, S., et al. 2003, *VizieR Online Data Catalog*, 2246
- Dai, F., Masuda, K., Winn, J. N., & Zeng, L. 2019, *ApJ*, 883, 79
- Dang, L., Calchi Novati, S., Carey, S., & Cowan, N. B. 2020, *MNRAS*, 497, 5309
- Dang, L., Cowan, N. B., Schwartz, J. C., et al. 2018, *Nature Astronomy*, 2, 220
- Dang, L., Cowan, N. B., Hammond, M., et al. 2021, A Hell of a Phase Curve: Mapping the Surface and Atmosphere of a Lava Planet K2-141b, JWST Proposal. Cycle 1
- Dawson, R. I., & Johnson, J. A. 2018, *ARA&A*, 56, 175
- Daylan, T., Günther, M. N., Mikal-Evans, T., et al. 2021, *AJ*, 161, 131
- de Kleer, K., Skrutskie, M., Leisenring, J., et al. 2017, *Nature*, 545, 199

REFERENCES

- de Wit, J., Lewis, N. K., Langton, J., et al. 2016, *ApJ*, 820, L33
- Delorme, P., Schmidt, T., Bonnefoy, M., et al. 2017, *A&A*, 608, A79
- Deming, D., & Knutson, H. A. 2020, *Nature Astronomy*, 4, 453
- Deming, D., Knutson, H., Agol, E., et al. 2011, *ApJ*, 726, 95
- Deming, D., Knutson, H., Kammer, J., et al. 2015, *ApJ*, 805, 132
- Demory, B.-O., Gillon, M., Madhusudhan, N., & Queloz, D. 2016a, *Monthly Notices of the Royal Astronomical Society*, 455, 2018
- Demory, B.-O., de Wit, J., Lewis, N., et al. 2013, *Astrophysical Journal Letters*, 776, L25
- Demory, B.-O., Gillon, M., de Wit, J., et al. 2016b, *Nature*, 532, 207
- Dobbs-Dixon, I., & Cowan, N. B. 2017, *ApJ*, 851, L26
- Dong, S., Udalski, A., Gould, A., et al. 2007, *ApJ*, 664, 862
- Durante, D., Parisi, M., Serra, D., et al. 2020, *Geophys. Res. Lett.*, 47, e86572
- Einstein, A. 1916, *Annalen der Physik*, 354, 769
- . 1936, *Science*, 84, 506
- Espinoza, N., & Jordán, A. 2015, *Monthly Notices of the Royal Astronomical Society*, 450, 1879
- Espinoza, N., Bello-Arufe, A., Buchhave, L. A., et al. 2021, The first near-infrared spectroscopic phase-curve of a super-Earth, JWST Proposal. Cycle 1, ID. #2159
- Fabrycky, D. C., Johnson, E. T., & Goodman, J. 2007, *ApJ*, 665, 754
- Fazio, G. G., Hora, J. L., Allen, L. E., et al. 2004, *ApJS*, 154, 10
- Feng, Y. K., Line, M. R., Fortney, J. J., et al. 2016, *Astrophysical Journal*, 829, 52
- Foreman-Mackey, D. 2016, *The Journal of Open Source Software*, 1, 24
- Foreman-Mackey, D., Hogg, D. W., Lang, D., & Goodman, J. 2013, *PASP*, 125, 306
- Fortney, J. J., Lodders, K., Marley, M. S., & Freedman, R. S. 2008, *ApJ*, 678, 1419
- Fulton, B. J., Petigura, E. A., Howard, A. W., et al. 2017, *AJ*, 154, 109

REFERENCES

- Gaia Collaboration, Prusti, T., de Bruijne, J. H. J., et al. 2016, *A&A*, 595, A1
- Gaia Collaboration, Brown, A. G. A., Vallenari, A., et al. 2018, *A&A*, 616, A1
- . 2021, *A&A*, 649, A1
- Gaudi, B. S. 2012, *ARA&A*, 50, 411
- Gaudi, B. S. 2022, in *Astrophysics and Space Science Library*, Vol. 466, *Demographics of Exoplanetary Systems*, Lecture Notes of the 3rd Advanced School on Exoplanetary Science, ed. K. Biazzo, V. Bozza, L. Mancini, & A. Sozzetti, 237–291
- Gillon, M., Lanotte, A. A., Barman, T., et al. 2010, *A&A*, 511, A3
- Gomes, R., Levison, H. F., Tsiganis, K., & Morbidelli, A. 2005, *Nature*, 435, 466
- Goody, R., West, R., Chen, L., & Crisp, D. 1989, *J. Quant. Spec. Radiat. Transf.*, 42, 539
- Gould, A. 1994, *ApJ*, 421, L75
- Gould, A., & Horne, K. 2013, *ApJ*, 779, L28
- Gould, A., Ryu, Y.-H., Calchi Novati, S., et al. 2020, *Journal of Korean Astronomical Society*, 53, 9
- Guillot, T., & Havel, M. 2011, *A&A*, 527, A20
- Hammond, M., & Pierrehumbert, R. T. 2017, *ApJ*, 849, 152
- Han, C., Udalski, A., Gould, A., et al. 2016, *ApJ*, 828, 53
- . 2017, *ApJ*, 834, 82
- Han, C., Calchi Novati, S., Udalski, A., et al. 2018, *ApJ*, 859, 82
- Hansen, C. J., Schwartz, J. C., & Cowan, N. B. 2014, *MNRAS*, 444, 3632
- Hébrard, G., Bouchy, F., Pont, F., et al. 2008, *A&A*, 488, 763
- Henderson, C. B., Poleski, R., Penny, M., et al. 2016, *PASP*, 128, 124401
- Heng, K. 2018, *Research Notes of the American Astronomical Society*, 2, 128
- Heng, K., & Showman, A. P. 2015, *Annual Review of Earth and Planetary Sciences*, 43, 509
- Hirao, Y., Bennett, D. P., Ryu, Y.-H., et al. 2020, *AJ*, 160, 74

REFERENCES

- Hu, R., Brandeker, A., Damiano, M., et al. 2021, Determining the Atmospheric Composition of the Super-Earth 55 Cancri e, JWST Proposal. Cycle 1, ID. #1952
- Huang, C. X., Penev, K., Hartman, J. D., et al. 2015, MNRAS, 454, 4159
- Hunter, J. D. 2007, Computing in Science and Engineering, 9, 90
- Hut, P. 1981, A&A, 99, 126
- Ibgui, L., & Burrows, A. 2009, ApJ, 700, 1921
- Ingalls, J. G., Krick, J. E., Carey, S. J., et al. 2016, AJ, 152, 44
- Ingersoll, A. P. 1989, Icarus, 81, 298
- Iro, N., & Deming, L. D. 2010, ApJ, 712, 218
- Ito, Y., Ikoma, M., Kawahara, H., et al. 2015, ApJ, 801, 144
- Jackson, B., Jensen, E., Peacock, S., Arras, P., & Penev, K. 2016, Celestial Mechanics and Dynamical Astronomy, 126, 227
- Johns-Krull, C. M., McCullough, P. R., Burke, C. J., et al. 2008, ApJ, 677, 657
- Johnson, S. A., Penny, M., Gaudi, B. S., et al. 2020, AJ, 160, 123
- Jung, Y. K., Gould, A., Udalski, A., et al. 2019, AJ, 158, 28
- Kass, R. E., & Raftery, A. E. 1995, Journal of the american statistical association, 90, 773
- Kataria, T., Lewis, N., Mayorga, L. C., et al. 2021, A Blast From the Past: A Spectroscopic look at the Flash Heating of HD80606b, JWST Proposal. Cycle 1, ID. #2008
- Kataria, T., Showman, A. P., Fortney, J. J., Marley, M. S., & Freedman, R. S. 2014, ApJ, 785, 92
- Kataria, T., Showman, A. P., Lewis, N. K., et al. 2013, ApJ, 767, 76
- Keating, D., & Cowan, N. B. 2017, ApJ, 849, L5
- Keating, D., Cowan, N. B., & Dang, L. 2019, Nature Astronomy, 3, 1092
- Keating, D., Stevenson, K. B., Cowan, N. B., et al. 2020, AJ, 159, 225

REFERENCES

- Kempton, E. M.-R., Bean, J. L., & Parmentier, V. 2017, *Astrophysical Journal Letters*, 845, L20
- Kipping, D. M. 2013, *MNRAS*, 435, 2152
- Kite, E. S., Jr., B. F., Schaefer, L., & Gaidos, E. 2016, *ApJ*, 828, 80
- Knutson, H. A., Charbonneau, D., Allen, L. E., et al. 2007, *Nature*, 447, 183
- Knutson, H. A., Lewis, N., Fortney, J. J., et al. 2012, *ApJ*, 754, 22
- Koll, D. D. B., & Komacek, T. D. 2018, *ApJ*, 853, 133
- Koshimoto, N., & Bennett, D. P. 2020, *AJ*, 160, 177
- Kreidberg, L. 2015, *Publications of the Astronomical Society of the Pacific*, 127, 1161
- Kreidberg, L., Line, M. R., Parmentier, V., et al. 2018, *AJ*, 156, 17
- Krick, J. E., Fraine, J., Ingalls, J., & Deger, S. 2020, *AJ*, 160, 99
- Langton, J., & Laughlin, G. 2008, *ApJ*, 674, 1106
- Lanotte, A. A., Gillon, M., Demory, B. O., et al. 2014, *A&A*, 572, A73
- Lanza, A. F., Pagano, I., Leto, G., et al. 2009, *Astronomy and Astrophysics*, 493, 193
- Laughlin, G., Deming, D., Langton, J., et al. 2009, *Nature*, 457, 562
- Lee, E. J., & Chiang, E. 2017, *ApJ*, 842, 40
- Lee, G., Dobbs-Dixon, I., Helling, C., Bognar, K., & Woitke, P. 2016, *Astronomy and Astrophysics*, 594, A48
- Levrard, B., Correia, A. C. M., Chabrier, G., et al. 2007, *A&A*, 462, L5
- Lewis, N. K., Parmentier, V., Kataria, T., et al. 2017a, *ArXiv e-prints*, arXiv:1706.00466
- . 2017b, *arXiv e-prints*, arXiv:1706.00466
- Lewis, N. K., Showman, A. P., Fortney, J. J., Knutson, H. A., & Marley, M. S. 2014, *ApJ*, 795, 150
- Lewis, N. K., Showman, A. P., Fortney, J. J., et al. 2010, *ApJ*, 720, 344

REFERENCES

- Lewis, N. K., Knutson, H. A., Showman, A. P., et al. 2013, *ApJ*, 766, 95
- Li, S. S., Zang, W., Udalski, A., et al. 2019, *MNRAS*, 488, 3308
- Lin, D. N. C., Bodenheimer, P., & Richardson, D. C. 1996, *Nature*, 380, 606
- Liu, X., Burrows, A., & Ibgui, L. 2008, *ApJ*, 687, 1191
- Lopez, E. D. 2017, *MNRAS*, 472, 245
- Luger, R., Agol, E., Kruse, E., et al. 2016, *AJ*, 152, 100
- Luger, R., Kruse, E., Foreman-Mackey, D., Agol, E., & Saunders, N. 2018, *AJ*, 156, 99
- Lutgens, F. K., Tarbuck, E. J., & Tasa, D. G. 2014, *Essentials of geology* (Pearson Higher Ed)
- Léger, A., Grasset, O., Fegley, B., et al. 2011, *Icarus*, 213, 1
- Machalek, P., Greene, T., McCullough, P. R., et al. 2010, *ApJ*, 711, 111
- Malavolta, L., Mayo, A. W., Louden, T., et al. 2018, *AJ*, 155, 107
- Malhotra, R. 1993, *Nature*, 365, 819
- Mandel, K., & Agol, E. 2002, *ApJ*, 580, L171
- Mansfield, M., Bean, J. L., Stevenson, K. B., et al. 2020, *ApJ*, 888, L15
- Mardling, R. A., & Lin, D. N. C. 2002, *ApJ*, 573, 829
- Marley, M. S., & McKay, C. P. 1999, *Icarus*, 138, 268
- Marley, M. S., Seager, S., Saumon, D., et al. 2002, *ApJ*, 568, 335
- Maxted, P. F. L., Anderson, D. R., Doyle, A. P., et al. 2013, *MNRAS*, 428, 2645
- May, E., Stevenson, K., Bean, J., et al. 2022, arXiv e-prints, arXiv:2203.15059
- May, E. M., Komacek, T. D., Stevenson, K. B., et al. 2021, arXiv e-prints, arXiv:2107.03349
- Mayor, M., & Queloz, D. 1995, *Nature*, 378, 355
- Mayorga, L. C., Robinson, T. D., Marley, M. S., May, E. M., & Stevenson, K. B. 2021, *ApJ*, 915, 41

REFERENCES

- Mendonça, J. M., Grimm, S. L., Grosheintz, L., & Heng, K. 2016, *ApJ*, 829, 115
- Menou, K. 2012, *Astrophysical Journal*, 745, 138
- Mighell, K. J. 2005, *Monthly Notices of the Royal Astronomical Society*, 361, 861
- Miguel, Y., Kaltenegger, L., Fegley, B., & Schaefer, L. 2011, *ApJ*, 742, 19
- Millholland, S. 2019, *ApJ*, 886, 72
- Morello, G. 2015, *ApJ*, 808, 56
- Morello, G., Waldmann, I. P., Tinetti, G., et al. 2014, *ApJ*, 786, 22
- Moses, J. I., Madhusudhan, N., Visscher, C., & Freedman, R. S. 2013, *Astrophysical Journal*, 763, 25
- Naoz, S., Farr, W. M., Lithwick, Y., Rasio, F. A., & Teyssandier, J. 2013, *MNRAS*, 431, 2155
- Nguyen, T. G., Cowan, N. B., Banerjee, A., & Moores, J. E. 2020, *MNRAS*, 499, 4605
- Nguyen, T. G., Cowan, N. B., Pierrehumbert, R. T., Lupu, R. E., & Moores, J. E. 2022, *MNRAS*, 513, 6125
- Owen, J. E., & Wu, Y. 2017, *ApJ*, 847, 29
- Paczynski, B. 1986, *ApJ*, 304, 1
- Parmentier, V., Fortney, J. J., Showman, A. P., Morley, C., & Marley, M. S. 2016, *Astrophysical Journal*, 828, 22
- Parmentier, V., Line, M. R., Bean, J. L., et al. 2018, *A&A*, 617, A110
- Peale, S. J., & Cassen, P. 1978, *Icarus*, 36, 245
- Peale, S. J., Cassen, P., & Reynolds, R. T. 1979, *Science*, 203, 892
- Penny, M. T., Gaudi, B. S., Kerins, E., et al. 2019, *ApJS*, 241, 3
- Perez, F., & Granger, B. E. 2007, *Computing in Science and Engineering*, 9, 21
- Perez-Becker, D., & Showman, A. P. 2013, *Astrophysical Journal*, 776, 134
- Perna, R., Menou, K., & Rauscher, E. 2010, *Astrophysical Journal*, 719, 1421
- Phillips, M. W., Tremblin, P., Baraffe, I., et al. 2020, *A&A*, 637, A38

REFERENCES

- Poleski, R., Penny, M., Gaudi, B. S., et al. 2019, *A&A*, 627, A54
- Poleski, R., & Yee, J. C. 2019, *Astronomy and Computing*, 26, 35
- Poleski, R., Zhu, W., Christie, G. W., et al. 2016, *ApJ*, 823, 63
- Rasio, F. A., & Ford, E. B. 1996, *Science*, 274, 954
- Rauscher, E., & Kempton, E. M. R. 2014, *Astrophysical Journal*, 790, 79
- . 2015, *Astrophysical Journal*, 799, 241
- Refsdal, S. 1966, *MNRAS*, 134, 315
- Ricker, G. R., Winn, J. N., Vanderspek, R., et al. 2015, *Journal of Astronomical Telescopes, Instruments, and Systems*, 1, 014003
- Rogers, T. M. 2017, *Nature Astronomy*, 1, 0131
- Rogers, T. M., & Komacek, T. D. 2014, *Astrophysical Journal*, 794, 132
- Roman, M., & Rauscher, E. 2017, *ApJ*, 850, 17
- Ryu, Y. H., Yee, J. C., Udalski, A., et al. 2018, *AJ*, 155, 40
- Sanchis-Ojeda, R., Rappaport, S., Winn, J. N., et al. 2014, *ApJ*, 787, 47
- Schaefer, L., & Fegley, B. 2009, *ApJ*, 703, 113
- Schröter, S., Czesla, S., Wolter, U., et al. 2011, *A&A*, 532, A3
- Schwartz, J. C., & Cowan, N. B. 2015, *Monthly Notices of the Royal Astronomical Society*, 449, 4192
- . 2017, *Publications of the Astronomical Society of the Pacific*, 129, 014001
- Schwartz, J. C., Kashner, Z., Jovmir, D., & Cowan, N. B. 2017, *ApJ*, 850, 154
- Schwarz, G. 1978, *Annals of Statistics*, 6, 461
- Schwarz, G., et al. 1978, *The annals of statistics*, 6, 461
- Seager, S., & Deming, D. 2010, *ARA&A*, 48, 631
- Shan, Y., Yee, J. C., Udalski, A., et al. 2019, *ApJ*, 873, 30
- Shin, I. G., Udalski, A., Yee, J. C., et al. 2017, *AJ*, 154, 176

REFERENCES

- . 2018, *ApJ*, 863, 23
- Showman, A. P., Fortney, J. J., Lian, Y., et al. 2009, *ApJ*, 699, 564
- Showman, A. P., & Guillot, T. 2002, *A&A*, 385, 166
- Shvartzvald, Y., Udalski, A., Gould, A., et al. 2015, *ApJ*, 814, 111
- Shvartzvald, Y., Li, Z., Udalski, A., et al. 2016, *ApJ*, 831, 183
- Shvartzvald, Y., Yee, J. C., Calchi Novati, S., et al. 2017, *ApJ*, 840, L3
- Shvartzvald, Y., Yee, J. C., Skowron, J., et al. 2019, *AJ*, 157, 106
- Sikora, J., Barclay, T., Colon, K., et al. 2021, Real Time Exoplanet Meteorology: Direct Measurement of Cloud Dynamics on the High-Eccentricity Hot Jupiter HD80606 b, JWST Proposal. Cycle 1
- Silva-Valio, A., Lanza, A. F., Alonso, R., & Barge, P. 2010, *Astronomy and Astrophysics*, 510, A25
- Snellen, I. A. G., de Mooij, E. J. W., & Burrows, A. 2010, *Astronomy and Astrophysics*, 513, A76
- Socrates, A. 2013, arXiv e-prints, arXiv:1304.4121
- Soubiran, C., Le Campion, J. F., Brouillet, N., & Chemin, L. 2020, *VizieR Online Data Catalog*, B/pastel
- Spergel, D., Gehrels, N., Baltay, C., et al. 2015, arXiv e-prints, arXiv:1503.03757
- Spiegel, D. S., Burrows, A., & Milsom, J. A. 2011, *ApJ*, 727, 57
- Stassun, K. G., Collins, K. A., & Gaudi, B. S. 2017, *AJ*, 153, 136
- Stassun, K. G., & Torres, G. 2018, *ApJ*, 862, 61
- Steinrueck, M. E., Parmentier, V., Showman, A. P., Lothringer, J. D., & Lupu, R. E. 2019, *ApJ*, 880, 14
- Stevenson, K. B., Harrington, J., Fortney, J. J., et al. 2012, *ApJ*, 754, 136
- Stevenson, K. B., Désert, J.-M., Line, M. R., et al. 2014, *Science*, 346, 838
- Stevenson, K. B., Line, M. R., Bean, J. L., et al. 2017, *AJ*, 153, 68
- Street, R. A., Udalski, A., Calchi Novati, S., et al. 2016, *ApJ*, 819, 93

REFERENCES

- STScI Development Team. 2013, pysynphot: Synthetic photometry software package, ascl:1303.023
- Tamburo, P., Mandell, A., Deming, D., & Garhart, E. 2018, *AJ*, 155, 221
- Thommes, E. W., Duncan, M. J., & Levison, H. F. 1999, *Nature*, 402, 635
- Thorngren, D., Gao, P., & Fortney, J. J. 2019, *ApJ*, 884, L6
- Thorngren, D. P., & Fortney, J. J. 2018, *AJ*, 155, 214
- Thorngren, D. P., Fortney, J. J., Murray-Clay, R. A., & Lopez, E. D. 2016, *ApJ*, 831, 64
- Tremblin, P., Chabrier, G., Mayne, N. J., et al. 2017, *ApJ*, 841, 30
- Tsapras, Y. 2018, *Geosciences*, 8, 365
- Turner, J. D., Leiter, R. M., Biddle, L. I., et al. 2017, *MNRAS*, 472, 3871
- Udalski, A., Szymański, M. K., & Szymański, G. 2015a, , 65, 1
- Udalski, A., Yee, J. C., Gould, A., et al. 2015b, *ApJ*, 799, 237
- Udalski, A., Han, C., Bozza, V., et al. 2018, *ApJ*, 853, 70
- Valsecchi, F., Rappaport, S., Rasio, F. A., Marchant, P., & Rogers, L. A. 2015, *ApJ*, 813, 101
- van der Walt, S., Colbert, S. C., & Varoquaux, G. 2011, *Computing in Science and Engineering*, 13, 22
- Visscher, C. 2012, *ApJ*, 757, 5
- von Essen, C., Mallonn, M., Piette, A., et al. 2021, *A&A*, 648, A71
- Walsh, K. J., Morbidelli, A., Raymond, S. N., O'Brien, D. P., & Mandell, A. M. 2012, , 47, 1941
- Wang, D., Hogg, D. W., Foreman-Mackey, D., & Schölkopf, B. 2016, *PASP*, 128, 094503
- Wang, T., Calchi Novati, S., Udalski, A., et al. 2018, *ApJ*, 860, 25
- Weidenschilling, S. J., & Marzari, F. 1996, *Nature*, 384, 619
- Werner, M. W., Roellig, T. L., Low, F. J., et al. 2004, *ApJS*, 154, 1

REFERENCES

- Wilkins, A. N., Deming, D., Madhusudhan, N., et al. 2014, *Astrophysical Journal*, 783, 113
- Winn, J. N., Sanchis-Ojeda, R., & Rappaport, S. 2018, , 83, 37
- Winn, J. N., Holman, M. J., Torres, G., et al. 2008, *ApJ*, 683, 1076
- Winn, J. N., Johnson, J. A., Fabrycky, D., et al. 2009, *ApJ*, 700, 302
- Wisdom, J. 2004, *AJ*, 128, 484
- Wit, E., Heuvel, E. v. d., & Romeijn, J.-W. 2012, *Statistica Neerlandica*, 66, 217
- Wong, I., Knutson, H. A., Cowan, N. B., et al. 2014, *ApJ*, 794, 134
- Wong, I., Knutson, H. A., Lewis, N. K., et al. 2015, *ApJ*, 811, 122
- Wong, I., Knutson, H. A., Kataria, T., et al. 2016, *ApJ*, 823, 122
- Wong, I., Benneke, B., Shporer, A., et al. 2020, *AJ*, 159, 104
- Wordsworth, R. D., Forget, F., Selsis, F., et al. 2011, *ApJ*, 733, L48
- Wu, Y., & Lithwick, Y. 2011, *ApJ*, 735, 109
- Yadav, R. K., & Thorngren, D. P. 2017, *ApJ*, 849, L12
- Yang, F., & Wei, X. 2022, *PASP*, 134, 024401
- Yee, J. C., Shvartzvald, Y., Gal-Yam, A., et al. 2012, *ApJ*, 755, 102
- Yee, J. C., Gould, A., Beichman, C., et al. 2015a, *ApJ*, 810, 155
- Yee, J. C., Udalski, A., Calchi Novati, S., et al. 2015b, *ApJ*, 802, 76
- Yoo, J., DePoy, D. L., Gal-Yam, A., et al. 2004, *ApJ*, 616, 1204
- Youdin, A. N., & Mitchell, J. L. 2010, *ApJ*, 721, 1113
- Zang, W., Dong, S., Gould, A., et al. 2020a, *ApJ*, 897, 180
- Zang, W., Shvartzvald, Y., Wang, T., et al. 2020b, *ApJ*, 891, 3
- Zellem, R. T., Lewis, N. K., Knutson, H. A., et al. 2014, *ApJ*, 790, 53
- Zhang, M., Dai, F., Hu, R., Knutson, H. A., & Lam, K. 2021, The First and Only Multi-wavelength Map of an Ultra-short-period sub-Earth, JWST Proposal. Cycle 1, ID. #2508

REFERENCES

- Zhang, M., Knutson, H. A., Kataria, T., et al. 2018, *AJ*, 155, 83
- Zhu, W., & Dong, S. 2021, *ARA&A*, 59, arXiv:2103.02127
- Zhu, W., Gould, A., Beichman, C., et al. 2015a, *ApJ*, 814, 129
- Zhu, W., Udalski, A., Gould, A., et al. 2015b, *ApJ*, 805, 8
- Zhu, W., Calchi Novati, S., Gould, A., et al. 2016, *ApJ*, 825, 60
- Zhu, W., Udalski, A., Huang, C. X., et al. 2017a, *ApJ*, 849, L31
- Zhu, W., Huang, C. X., Udalski, A., et al. 2017b, *PASP*, 129, 104501
- Zhu, W., Udalski, A., Novati, S. C., et al. 2017c, *AJ*, 154, 210
- Zieba, S., Zilinskas, M., Kreidberg, L., et al. 2022, arXiv e-prints, arXiv:2203.00370
- Zilinskas, M., Miguel, Y., Lyu, Y., & Bax, M. 2021, *MNRAS*, 500, 2197
- Zilinskas, M., Miguel, Y., Mollière, P., & Tsai, S.-M. 2020, *MNRAS*, 494, 1490
- Zilinskas, M., van Buchem, C. P. A., Miguel, Y., et al. 2022, *A&A*, 661, A126